Alma Mater Studiorum · Università di Bologna

Scuola di Scienze
Dipartimento di Fisica e Astronomia
Corso di Laurea Magistrale in Fisica

Surface and interface states investigated in Si based thin films for photovoltaic applications

Relatore:
Prof.ssa Daniela Cavalcoli

Correlatore:
Dott.ssa M. A. Fazio

Presentata da:
Bruna Dudda

Anno Accademico 2016/2017

Abstract (versione in italiano)

Negli ultimi anni, le celle fotovoltaiche a eterogiunzione in Silicio (SHJ) hanno dimostrato i risultati più promettenti nella famiglia del fotovoltaico a film sottile, raggiungendo efficienze record per le celle basate su silicio, intorno al 25% [1]. Questi dispositivi devono le loro alte prestazioni all'utilizzo di un blocco emettitore, il quale consiste in un doppio layer di silicio amorfo, intrinseco e drogato, che viene depositato su entrambe le facce della base di silicio cristallino. Tale struttura garantisce al contempo la passivazione dei difetti d'interfaccia e il trasporto della carica fotogenerata verso i contatti metallici [2, 3].

L'ossinitruro di silicio nanocristallino idrogenato (nc-SiO_xN_y:H) è stato recentemente individuato come potenziale sostituto del silicio amorfo nelle celle SHJ. Quest'ultimo presenta infatti un elevato assorbimento parassita della luce, che causa una diminuzione della corrente di corto-circuito, e dunque un abbassamento dell'efficienza di conversione fotovoltaica dei dispositivi [4, 5]. Questo problema viene notevolmente ridotto con l'utilizzo del SiO_xN_y in quanto esso presenta un bandgap più ampio e facilmente tunabile [4]. Il SiO_xN_y nanocristallino è un materiale composito che presenta una struttura complessa caratterizzata da una miscela di fasi cristalline e di fase amorfe [6]. Da misure di spettroscopia in trasmissione è emerso che il bandgap ottico di questo materiale può arrivare a energie di 2.5 eV [7]. Inoltre, esso presenta ottime proprietà elettriche, con conducibilità fino a 44 S/cm [6].

Questa tesi si propone di presentare lo studio di film sottili di nc-SiO_xN_y:H effettuato mediante spettroscopia di fototensione superficiale (SPV) e caratterizzazione elettrica, allo scopo di valutare come la variazione del contenuto di ossigeno e il trattamento termico influiscono sulle proprietà optoelettroniche e sulla conducibilità del materiale.

Per prima cosa è stata effettuata la taratura dell'apparato per le misure di SPV, al fine di stabilire le condizioni ottimali per l'acquisizione dello spettro del flusso delle sorgenti luminose. Le misure del flusso dei fotoni emessi da due diverse lampade in due diversi intervalli spettrali, effettuate con un sensore piroelettrico, sono state successivamente utilizzate per la normalizzazione dei segnali SPV ottenuti dai campioni.

Gli spettri di fototensione superficiale dei diversi campioni hanno permesso di ottenere informazioni importanti sullo stato dell'interfaccia SiON/substrato, sul valore del

gap energetico dei layer di SiON, sul ruolo del contenuto di ossigeno e dell'annealing su questi parametri.
Le misure di SPV hanno rivelato che il campione con basso contenuto di ossigeno, non trattato termicamente, presenta ottime proprietà passivanti. Al contrario, il processo di annealing, così come un maggiore contenuto di ossigeno nella matrice amorfa, sembrano portare ad un peggioramento della qualità dell'interfaccia.
Ciò potrebbe essere dovuto alla formazione di precipitati di ossigeno tra il substrato e il layer superiore, indotta dal trattamento termico, come mostrato da precedenti misure [6], che causerebbe dunque un aumento del disordine e la formazione di difetti all'interfaccia. La formazione di composti SiO_x potrebbe essere inoltre la causa dello spostamento del bandgap all'interfaccia col substrato verso enerie maggiori, osservato nel campione con maggiore contenuto di ossigeno.
Dagli spettri SPV è stato possibile ricavare il valore del bandgap dei campioni studiati. Inoltre, lo studio del campione più cristallino (a basso contenuto di ossigeno, non trattato termicamente) ha rivelato caratteristiche ad energie maggiori del bandgap che non sono presenti negli altri due campioni. Esse potrebbero indicare transizioni otticamente indotte tra livelli quantizzati all'interno dei nanocristalli di silicio.
Tale assunzione, sulla presenza di quantum dot (QD) di Si, risulterebbe in accordo con quanto emerso da analisi precenti sulle proprietà strutturali e sulla morfologia superficiale alla nanoscala [6, 8]. Queste avevano evidenziato che il trattamento termico induce una separazione di fase, portando alla formazione di aggregati di silicio cristallini con orientazione casuale immersi in una matrice amorfa, ricca di ossigeno [6, 8].

Le caratteristiche corrente-tensione hanno mostrato che le proprietà elettriche del materiale dipendono dalle condizioni di deposizione e dal trattamento termico. È stato trovato che l'annealing produce un aumento della conducibilità del materiale, attribuibile all'aggregazione di cristalli di Si altamente conduttivi all'interno della matrice amorfa, indotta appunto dal trattamento termico [6, 9]. Al contrario, l'assorbimento di maggiori quantità di ossigeno all'interno del reticolo amorfo limita fortemente la conduzione dei film a causa di un più elevato disordine strutturale [9]. I valori di conducibilità calcolati dalle caratteristiche corrente tensione dei campioni con basso contenuto di ossigeno e con alto contenuto di ossigeno, entrambi sottoposti ad annealing, risultano infatti differenti di tre ordini di grandezza.
L'andamento osservato per le proprietà elettriche macroscopiche dei campioni risulta in accordo sia con precedenti misure di conducibilità al buio, sia con precedenti studi riguardanti la conduttanza alla nano-scala.

Dai risultati di questa indagine emerge che per l'ottimizzazione del SiON nanocristallino al fine di una sua applicazione nelle celle solari SHJ sono necessari ulteriori studi. Di fatto, il trattamento di annealing produce due effetti contrastanti: da una parte, si mostra fondamentale per il raggiungimento di conducibilità elevate; dall'altra, esso porta a un

forte deterioramento delle proprietà passivanti del layer. Un'alternativa che potrebbe portare a simili valori di conducibilità è rappresentata dall'incremento della diluizione di idrogeno (H_2) durante il processo di deposizione, che ha come effetto l'aumento della cristallinità del materiale [10].

Abstract (English version)

In the last few years, silicon heterojunction (SHJ) solar cells have demonstrated the most promising results among the field of thin film photovoltaics, reaching record efficiencies for silicon-based devices of about 25% [1]. The key of these high performance devices relies on the concept of passivating layers in the heteroemitter stack: an intrinsic layer and a doped layer of hydrogenated amorphous silicon are both subsequently deposited on both the front and the rear side of the crystalline silicon thin film absorber.
Such heteroemitter stack serves the role of a semi-permeable membrane for carrier extraction [2, 3].

Recently, hydrogenated nanocrystalline silicon oxynitride (nc-SiO$_x$N$_y$:H) has been proposed as a suitable substitute for a-Si:H in SHJ cells. In fact, the latter presents strong parasitic absorption of light, which causes losses in short circuit current, and consequently prevents to achieve higher power conversion efficiencies [4, 5]. From transmission spectroscopy measurements emerged that nc-SiO$_x$N$_y$ can achieve optical bandgap values as high as 2.5 eV [7]. Furthermore, it has shown very high values for the dark conductivity, up to 44 S/cm [6]. The peculiar properties of this material arise from its complex structure, which comprises a mixture of crystalline and amorphous phases [6].

This thesis aims to report the investigation of nc-SiO$_x$N$_y$ thin films, deposited by Plasma-Enhanced Chemical Vapour Deposition (PECVD) on c-Si and glass substrates, conducted by means of surface photovoltage (SPV) measurements and electrical characterization. The study concerned in particular the evaluation of the influence of the oxygen content and the thermal treatment, on the optoelectronic and electrical properties of the SiO$_x$N$_y$ layers.

First of all, the calibration of the experimental set-up for SPV measurements has been conducted, in order to establish the optimal conditions for the acquisition of the light source intensity spectra. The spectra of the lamps, acquired with a pyroelectric sensor, have been used later for the normalization of the SPV signals of the samples.

Surface photovoltage spectroscopy (SPS) has been proven an important tool for the investigation of the passivating properties of the SiO$_x$N$_y$ layer at the interface with the c-Si substrate, for the extraction of the bandgap of the material, as well as to clarify the role of O content and annealing on this parameters.
SPV measurements have evidenced the excellent passivation quality of the sample with

low oxygen content, as-deposited. On the other hand, the annealing treatment and the enhancement of the oxygen incorporation into the amorphous network appear to have a negative impact on the interface, leading to a deterioration of the quality of the nc-SiON/c-Si interface. This could be due to the annealing-induced formation of the oxygen precipitates between the substrate and the buffer layer, as highlighted by previous results [6], which could lead to an enhancement of the disorder and the defects at the interface. The formation of SiO_x compounds could be also the cause of the observed blue shift of the bandgap in the sample with higher oxygen content, since the bandgap shifts towards SiO2 bandgap values ($\sim$9 eV [49]).
Furthermore, from SPV spectra it has been possible to extract the bandgap energy of the studied samples. In addition, the analysis of the measurements of the sample with high crystalline fraction (low oxygen content, 3 h annealed), have also revealed the presence of additional peaks at energies higher than the bandgap. These features might indicate possible optical transitions at higher energies due to quantum confinement effects at the silicon nanocrystals NCs.
This assumption would be in agreement with what had already been observed for the evolution of the structural properties and the surface morphology at the nano-scale [6, 8]. Those studies revealed that a phase separation is enhanced during the annealing process, which leads to the formation of a multi-phase material where Si-rich clusters are embedded within an O-rich amorphous matrix [6, 8].

Current voltage measurements have shown that the electical properties of the material are deeply influenced by the deposition conditions, i.e. the oxygen content, and the thermal treatment. The dark conductivity values obtained for the annealed samples deposited on glass differ by three orders of magnitude, being higher for the sample with low oxygen content. This is in accordance with the fact that higher oxygen incorporation within the layer leads to an increased structural disorder [6].
Therefore, the annealing has been found to produce an enhancement of the conductivity of the material, which could be attributed to the formation of highly conductive silicon crystals within the amorphous and less conductive matrix [6, 9]. Whereas, higher oxygen incorporation is seen to strongly hinder the conduction of the material [6, 9].
The observed trend for the electric behaviour of the samples is in good agreement with both macroscopic dark conductivity and nano-scale conductance results from precedent studies on the same samples [6, 9].

The results of the present investigation suggest that further studies are still required in order to achieve the optimization of nanocrystalline SiON films for their application in SHJ solar cells. It has been shown that the annealing treatment and low oxygen content lead to high dark conductivities; nonetheless, the thermal process also negatively affects the quality of the SiON/substrate interface. Similar high conductivity can be achieved by increasing the H_2 dilution during the deposition stage that boosts the layer crystallinity [10].

Contents

Abstract (versione in italiano) **3**

Abstract (English version) **7**

Introduction **11**

1 Introduction to Photovoltaics **15**

1.1 Climate change 15

1.1.1 Photovoltaics: a clean and renewable energy resource 17

1.2 The physics of solar cells 19

1.2.1 The solar radiation 19

1.2.2 The photovoltaic conversion 20

1.2.3 Performance parameters of a solar cell 21

1.2.4 Detailed balance 25

1.2.5 Maximum Efficiency 25

1.3 Three Generations of PV 26

1.4 Silicon Heterojunction Solar Cells 27

2 Surface Photovoltage Spectroscopy **33**

2.1 SPV: theoretical principle 34

2.1.1 Electronic structure of surfaces 34

2.1.2 The surface photovoltaic effect 37

2.2 Experimental methods 38

2.2.1 The Kelvin Probe 38

2.2.2 The Metal-Insulator-Semiconductor structure 39

2.2.3 Scanning SPV measurements 40

2.3 Applications of SPS 41

2.3.1 Determination of semiconductor bandgap and type 41

2.3.2 Detection of defect states and Urbach tails 43

2.3.3 Characterization of multilayered structures 43

3 Materials and Methods **47**
3.1 Materials . . . 47
3.2 Experimental Methods . . . 56
3.2.1 Surface Photovoltage Spectroscopy Apparatus . . . 56
3.2.2 Electrical Characterization . . . 63

4 Results **67**
4.1 Optimization of the SPS set-up . . . 67
4.2 SPV Measurements . . . 74
4.2.1 SiO_xN_y/Si interface properties . . . 74
4.2.2 SiO_xN_y surface properties . . . 77
4.3 Electrical Measurements . . . 83

Conclusions **87**

Ringraziamenti **91**

Bibliography **92**

Introduction

Since the 20th century, fossil fuels (coal, petrol, and oil) have been of great importance for almost every activity of the human race, from the production of electricity, to transportation, as well as in the petrochemical industry. However, according to the International Panel for Climate Change (IPCC), human alteration of green house gases GHGs emissions, deriving from fossil fuels combustion (mainly water vapour and carbon dioxide), can be regarded as the dominant cause of the observed global warming [11].
Indeed, in 2000 Nobel laureate Paul Crutzen first proposed the term Anthropocene (from the roots anthropo- = human, and -cene = epoch) for the period of time starting around 1800 with the onset of the Industrial Revolution, as to denote the period in which humankind's activities became a growing geological and morphological force [12].
As a matter of fact, the environmental impact of global warming includes profound alterations of the water cycles, annual snow and rain fall, thawing of the ice sheets, as well as rise of the sea level and temperature [11]. Indeed, continued emissions of GHGs at the current rate are believed to lead to severe and catastrophic repercussions on humans and biosystems on all continents [11].
The rate of consumption of fossil fuels is expected to further increase in the next years, to compound the problem, with expanding world population and increasing per capita energy demand.

It is indisputable that, to slow down global warming and inhibit its consequences, a transition from fossil fuels to renewable and sustainable energy resources must occur soon. Among the renewable technologies, solar energy is believed to be the most promising, as well as being certainly the most developed at the moment [13]. In particular, the direct exploitation of sunlight with photovoltaics (PV) alone could produce all the energy currently demanded, including electricity, heat, and trasportation, using a fraction of land much smaller that the one we use for agriculture [13, 14]. PV demostrates high reliability under all kinds of climate; besides, thanks to its modularity properties, it can enable the access to electricity even in the most remote regions of the planet, where grid connections are not present. It is worth to mention that, for the first time in 2015, a zero-fuel airplane was able to fly 40,000 km around the world completely powered by solar energy, marking an important milestone in aviation history [15].

Silicon has been the most used material in the PV industry since its breakthrough in the 1970s, mainly due to the fact that it was already widely exploited in the field of microelectronics, and because it is a stable, non-toxic, and easily available resource. In 2015, Si-based solar cells still dominated the market with almost 90% of share. Notwithstanding the steady reduction of PV technology over the years, silicon wafer still accounts for about 50% of the total cost of a finished module [16].
Therefore, in order for photovoltaics to achieve cost-competitive large-scale production, increase of the efficiency of solar irradiation conversion, as well as decrease of the amount of materials that are used, and reduction of the manufacturing and installation costs, are the prime issues to be addresses [17].

Within the technology of thin film solar cells, silicon heterojunctions (SHJ) have demostrated promising results, with a record-breaking efficiency of 25.6% for the SHJ with intrinsic thin layer (HIT) solar cell, by Panasonic [1]. The design of this cell features an intrinsic amorphous-Si layer, a doped amorphous-Si layer, together with a layer of a trasparent conductive oxyde (TCO), deposited on both sides of a thin (∼100 μm) crystalline-Si substrate [3].
The heteroemitter stack of SHJ solar cells serves the double purpose of the passivation of the wafer surface and the contacting role. In fact, as the substrate is thinned down, the recombination of the photogenerated carriers at its surface is enhanced, resulting in a reduction of the open circuit voltage of the cell. Moreover, the reduced amount of absorbed light in the thin active layer causes a decrease of the attainable short circuit current. Clearly, in order to achieve high output power, the maximization of light absorption and the efficient passivation of the surface, as well as of the metallic contacts with the active region, become extremely important [4, 2].

Although intrinsic a-Si:H is reported to provide excellent surface passivation quality, it also shows strong parasitic absorption of light, which leads to losses in short circuit current [4]. Recently, hydrogenated amorphous silicon oxynitride (a-SiO_xN_y:H) has attracted a lot of attention, due to its possible application in different fields (e.g. optoelectronic devices and microelectronics) and its low-cost fabrication technologies [18, 19, 20]. In PV this material has already been used as window layer and anti-reflective coating in thin films solar cells [21]; in addition, it seems to be a very good candidate to substitute a-Si:H as emitter layer in SHJ solar cells, due to the fact that it has a wider bandgap (that prevents a high parasitic absorption) and shows higher conductivity than amorphous silicon [4, 7].
As a matter of fact, the combination of intrinsic and doped a-SiO_xN_y layers with the c-Si absorber in SHJ solar cells resulted in a very high implied open circuit voltage, up to 733 mV [4]. Moreover, further efficiency increase is expected from replacing the amorphous films with nanocrystalline ones, since the latter exhibit enhanced conductivity and optical band gap values, as well as lower contact resistance to the TCO layer [7].

Previous studies on the structure and composition of nc-SiO_xN_y:H thin layers have

highlighted the complexity of this multi-phase material [6]. Nonetheless, the investigation of the optical and electrical properties have confirmed the great potential of silicon oxynitride as heteroemitter layer in SHJ solar cells, regarding in particular the enhancement of both the bandgap and the conductivity in the nanocrystalline layers [6, 7]. At last, it has been found that both the morphology of the surface and the electrical properties at the nano-scale are deeply affected by the oxygen content within the films and by the thermal treatment [8, 9].

This thesis presents the investigation of the properties of nc-Si$O_x N_y$:H thin layers deposited on c-Si and glass substrates, conducted by means of Surface Photovoltage Spectroscopy and electrical measurements, with the purpose to gain an understanding on the effect of the annealing treatment and the oxygen incorporation during the deposition, on the nc-Si$O_x N_y$/c-Si interface and nc-Si$O_x N_y$ electrical properties.

Chapter 1

Introduction to Photovoltaics

1.1 Climate change

The greenhouse effect is known since the 1820s, when a French scientist, Joseph Fourier, first realized that the Earth's atmosphere retains heat radiation [22]. Certain gases present in the atmosphere, including water vapor and carbon dioxide (CO_2), are opaque to heat rays: they let the sunlight pass through the atmosphere, simultaneously acting as heat-trapping particles. Fourier and its successors, understood that such gases high in the air help keeping our planet warm, and that, without the atmosphere, the planet would be much more cooler. In particular, they discovered that CO_2 sets the level of water vapour in the atmosphere: since water vapour is itself a greenhouse gas, its increase would push the temperature rise. This means that releasing CO_2 into the atmosphere leads to the enhancement of the greenhouse effect [23, 22].

During the past few thousand years, the production of greenhouse gases (GHGs) appeared to be counterbalanced by the absorption within the atmosphere through natural sinks, which helped to maintain their level fairly constant. This has enabled the development of a long-term equilibrium of the Earth's weather, as well as of all the other natural systems [22, 11]. However, over the last 300 years, coinciding with the beginning of the industrialization, green-house gas (GHG) emissions in the atmosphere have seen to rise at an unprecedent rate, reaching today the highest level in history [11]. We are currently facing the consequences of this dramatic trend, which is causing a deep alteration of the Earth's climate and of all the natural systems related to its cycles. Although climate change is also referred to as global warming in general, it includes warming the atmosphere and the oceans, changes in the global water cycle, reductions in snow and ice and global mean sea level rise (Figure 1.1). These modifications are seen to affect natural and human systems on all continents [11, 13].

According to the Interdipartimental Panel for Climate Change (IPCC) "human influence is extremely likely to have been the dominant cause of the observed global warming since the mid-20th century" [11]. As can be seen in the diagram in Figure 1.2, the main

contribution to the total anthropogenic GHGs emissions is CO_2 from fossil fuels combustion and industrial processes, accounting for more than 70% of the total. Continuos GHGs emissions at the present rate will exacerbate the risks of severe and irreversible impacts in all components of the climate system, as well as human activities and ecosystems [11].

As a consequence, given the exponential economic and population growth of the last century (almost 7.5 billions humans in 2015, forecasted to increase to more than 11 billions by the end of the century [24]) many efforts have started to be addressed in order to strengthen the global response to climate change. At the end of 2015, an historic global climate agreement was agreed within the United Nations Framework Convention on Climate Change (UNFCCC) at the 21st Conference of the Parties (COP21) in Paris. The Paris Agreement is a call to action for the global community to adopt responsible strategies for the substantial and sustained reductions in GHGs emissions, promoting actions to adapt and build resilience to climate impacts, and setting mitigation targets [25]. The UN have also agreed to the global goal to hold average temperature increase to well below 2 °C and pursue efforts to limit the increase to 1.5 °C above pre-industrial levels [25].

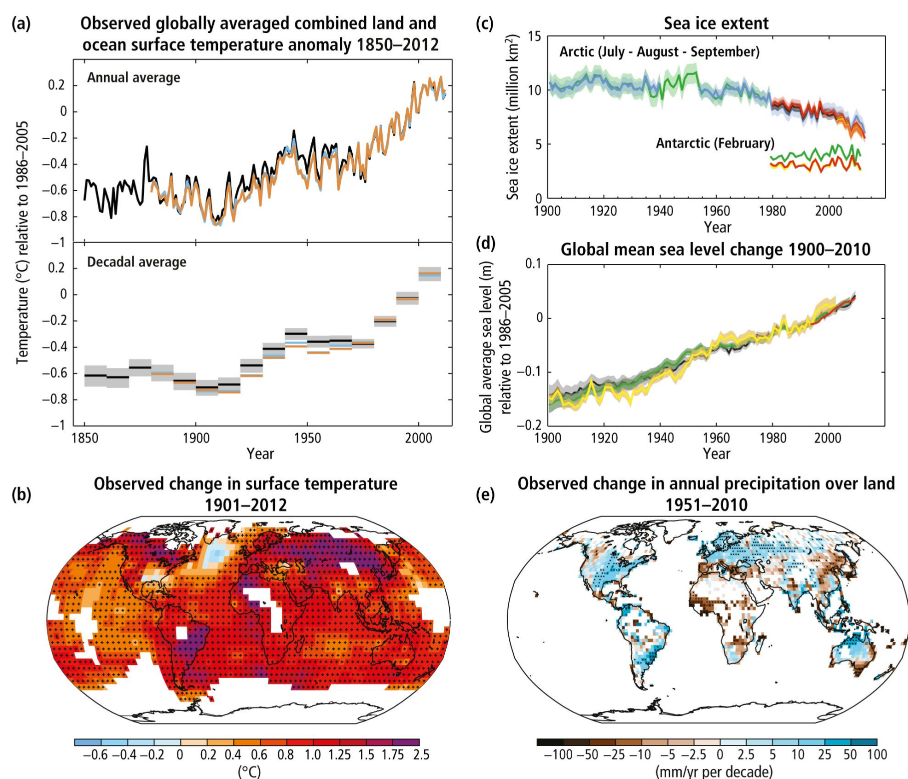

Figure 1.1: Multiple observed indicators of a changing global climate system [11].

Within this framework, it appears clear that the previous century methods of gener-

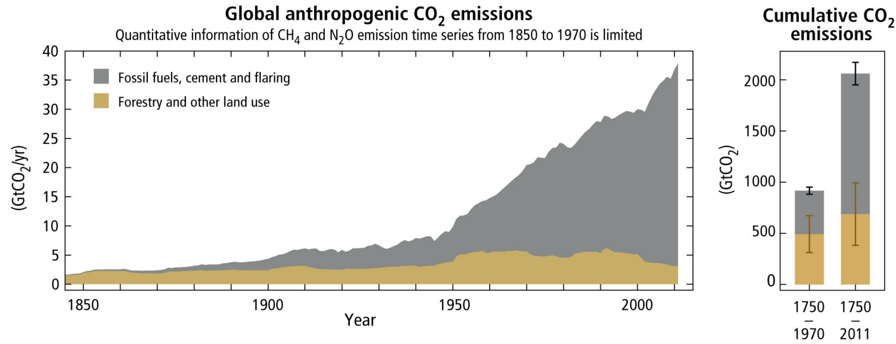

Figure 1.2: Global anthropogenic emissions of CO_2 per year, updated to 2011 [11].

ating the most useful form of energy, i.e. electricity, are no more sustainable. Now more than ever, it is essential to secure clean energy sources alternative to burning fossil fuels in order to switch to carbon-free economies as soon as possible [13]. Consequently, intensive scientific research for the development and constant improvement of new technologies has become crucial [1, 13].

1.1.1 Photovoltaics: a clean and renewable energy resource

Essentially, the most promising large-scale carbon-free energy sources, with the potential to fulfill the ever increasing global demand for electricity, are solar power-related technologies and nuclear power. Geothermal energy and tidal energy are significant only at a local scale, representing only a tiny fraction of the total energy income [13]. Nonetheless, although nuclear plants emit no CO_2, several problems related to the disposal of radioactive waste are yet to be solved.

The solar resource is widely accessible and essentially infinite: as a matter of fact, the amount of solar radiation arriving on Earth is 10,000 times the current energy consumption on the planet [13]. Among the various forms of solar energies (wind, biomass, tidal energy), the direct exploitation of the solar radiation appears the real big energy resource. In this regard, the photovoltaic technology (PV) has demonstrated to be the resource with the highest potential under many aspects [13].
Using photovoltaics with an efficiency of 10%, solar energy could be converted directly into enough electricity to provide 1000 times the current global consumption [13]. As an example, Fig. 1.3 reports the photovoltaic solar electricity potential in European countries for the total period between 1981 and 2011.
Moreover, PV has demonstrated to be able to generate electricity for a wide range of applications; thanks to its modularity and integration properties, it can operate at small or large scale, as well as in a variety of different climates and geographic locations [13].
At last, PV is regarded as a truly "green" energy resource, not only because of the cleaner operation of PV generators with respect to fossil-fuel or nuclear-fired generators, but also thanks to the low impact on the environment of the manufacturing processes and the

possibility to recycle the discarded modules [13].
For all these reasons, PV has demonstrated to be a fast growing market: in fact, between 2000 to 2015, the Compound Annual Growth Rate (CAGR) of PV installations was 42%. In 2015, Europe alone contributed for the 40% to the total cumulative PV installations (Figure 1.4a) [16].

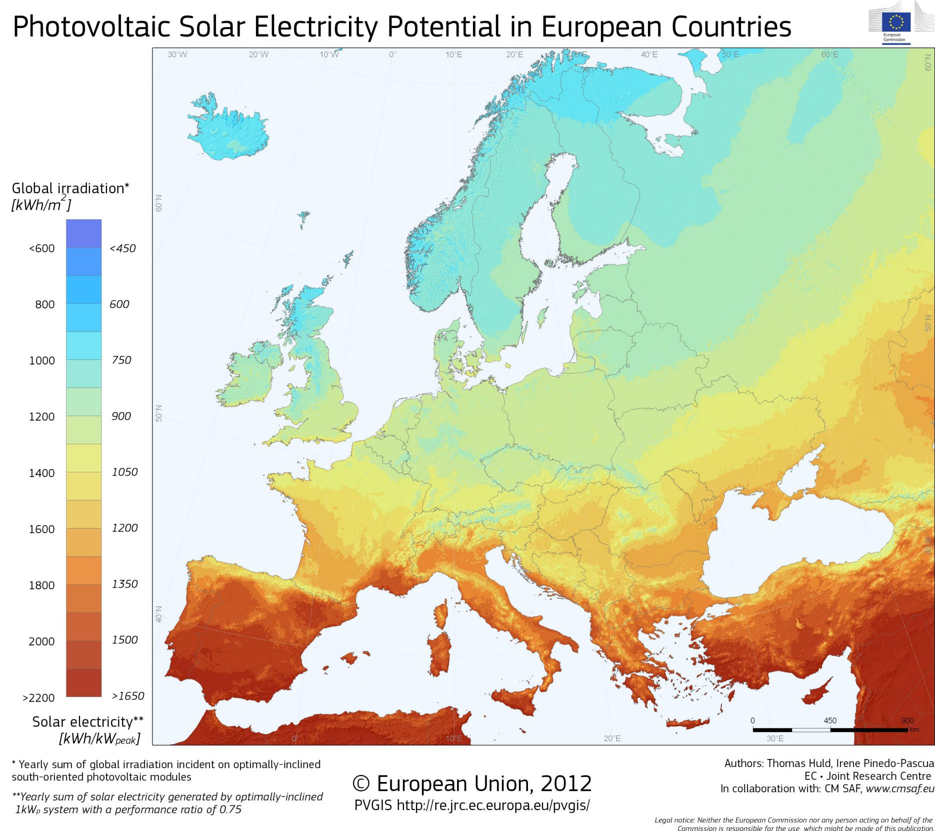

Figure 1.3: Photovoltaic Solar Electricity Potential in European countries: over most of the region, the data represent the average of the period 1998-2011. However, north of 58° N, the data represent the 10-years average of the period 1981-1990. The same colour legend represents also potential solar electricity [kWh/kWp] generated by a 1 kWp system per year with photovoltaic modules mounted at an optimum inclination and assuming system performance ratio 0.75 [26].

The Energy Payback Time (EPT) is used to measure how many years a system should operate to produce the energy required for its manufacture: after the payback time, all of the energy produced is truly new energy [13]. The EPT of PV systems depends on the geographical location: according to the 2016 Photovoltaic Report of the Fraunhofer Institute for Solar Energy Systems [16], PV systems in Northern Europe need around 2.5 years to balance the input energy, while PV systems in the South equal their energy input after 1.5 years or less, depending on the technology installed.
As can be seen from the "Module Price vs Comulative Production" curve (updated to

2015) in Figure 1.4b, for the last 35 years, each time the cumulative production doubled and the price of PV modules went down by 23% [16].
The achievement of higher power conversion efficiencies, as well as long term reliability, together with the reduction of the manufacturing costs, remain the main challenge for large-scale production of PV modules. Economies of scale and constantly-improving technologies are the key requirements to assure PV to become increasingly competitive in the global market of energy resources and to reach grid parity without subsidies [13].

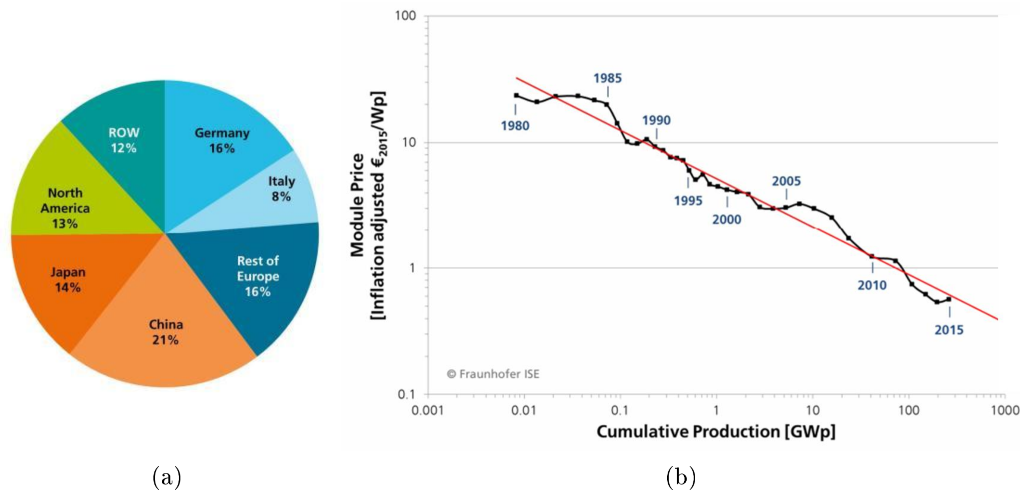

(a) (b)

Figure 1.4: (a) Global cumulative photovoltaic installation by region in 2015; all percentages are related to total global installations, including off-grid systems [16]. (b) Price Learning Curve including all commercially available PV technologies, updated to 2015 [16].

1.2 The physics of solar cells

1.2.1 The solar radiation

Sunlight is a spectrum of photons distributed over a wide range of energy. As can be seen from in Fig. 1.5, the extra-terrestrial spectrum of the sun rensembles the spectrum of a black body at 5760 K, spanning from the ultraviolet to the deep infrared, with a peak in the visible range of wavelengths (300 - 800 nm) [5]. However, the solar irradiance (i.e. the amount of radiant energy received from the Sun per unit area per unit time) deviates from the ideal case due to the fact that, on passing through the atmosphere, light is absorbed and scattered by the atmospheric constituents.
The reduction in the power of light as it passes through the atmosphere is quantified by the "Air Mass" (AM) factor [5]:

$$n_{AirMass} = \frac{\text{optical path length to Sun}}{\text{optical path length if Sun directly overhead}} \quad (1.1)$$

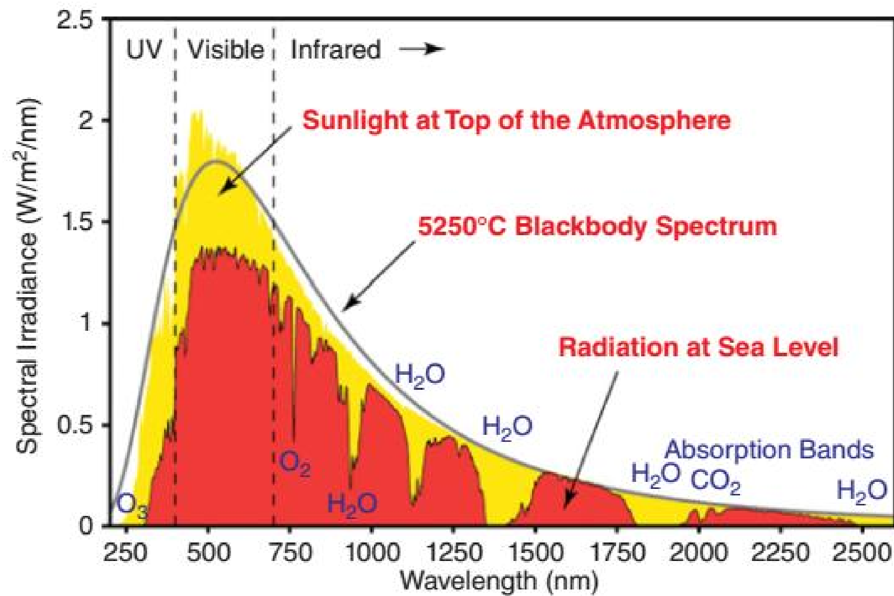

Figure 1.5: Solar spectrum at the top of the atmosphere and at the see level, compared with the 5760 K black body spectrum [27].

The standard spectrum outside the Earth's atmosphere is called AM0, while the standard spectrum at the Earth's surface is called *Air Mass 1.5*, or AM1.5, and corresponds to the Sun being at an angle of elevation of 42°. Typically, the AM1.5 is normalised so that the integrated irradiance is 1000 W m^{-2}, in order to take into account the effects of seasonal and daily variations of the position of the Sun [5].

1.2.2 The photovoltaic conversion

In a photovoltaic device the absorption of incident photons of radiant energy causes the generation of electron-hole pairs via band-to-band transitions (between the valence and the conduction bands of the semiconducting material that constituites the device). If a built-in electric field is present, it allows the separation of the photo-generated carriers before any recombination could take place, i.e. before the excited electrons could relax back to their ground state. At this point, the charges are collected at the contacts and can be driven through a load in an external circuit, thanks to the potential difference of the excited electrons.

This effect is known as photovoltaic conversion, and enables the operation of solar cells, devices based on the utilization of the solar radiation to produce electricity. In a solar cell the intrinsic electric field which allows the separation of the charge carriers is achieved with the realization of a p-n juction (Figure 1.6). The effectiveness of a photovoltaic device depends upon the choice of the light absorbing materials and the way through which they are connected to the external circuit [5].

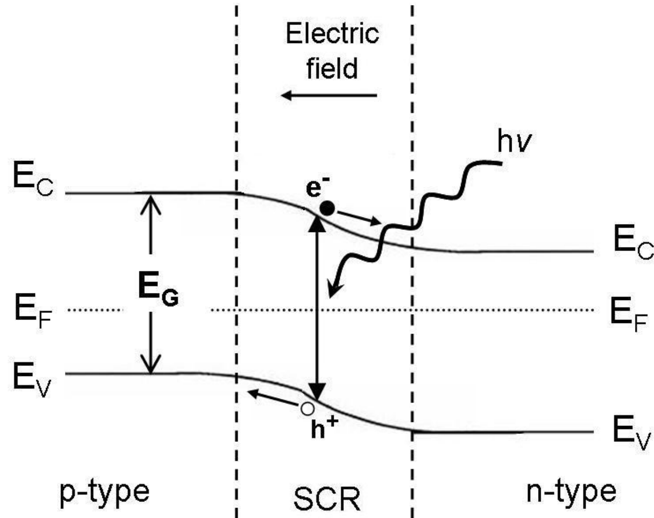

Figure 1.6: Photovoltaic conversion at a p-n junction. The bandgap of the material is indicated by E_G, while E_C, E_V, and E_F, denote the position of the conduction and valence bands, and of the Fermi level, respectively. $h\nu$ is the energy of the incident photons, which has to be $\geq E_G$ in order to be able to generate electron-hole pairs via band-to-band transitions. The electric field at the space charge region (SCR) provides the separation of the photo-generated carriers.

1.2.3 Performance parameters of a solar cell

The solar cell is the building block of solar photovoltaics. It consists of a wafer of semiconducting material, with a typical area of $\sim$100 cm^2 and thickness of hundreds of microns. This is the active region of the device, called absorber, where the electron-hole pairs are generated due to sunlight absorption. An emitter layer on top of the absorber constitutes the other half of the junction shown in Fig. 1.6, providing the separation of the carriers, and allowing the charge to be collected at the metallic contacts. When a load is connected to the terminals of the cell the carriers are able to flow through the external circuit.
Since a single cell can produce reasonable currents ($\propto$ 10 mA/cm^2) yet modest voltages ($<$ 1 V), typically, 28 to 36 cells are connected in series to form a module, to produce a DC output voltage of 12 V. To obtain further increase of the output, several modules can be connected in series or parallel.
Bypass and blocking diodes are also present within the circuit, in order to prevent the loss of power which would result from the failure of one the cells in series. Such arrays are called PV generators. A battery and a power conditioning system are usually integrated in the generator, to provide energy storage and power regulation, depending on the irradiation conditions. At last, an inverter is essential for the conversion to AC power of appropriate frequency [5].

In the following we will give the definition of the key parameters used to describe

the performances of a solar cell. These characteristics are usually defined for particular illumination conditions. The Standard Test Condition (STC) for solar cells is the AM1.5 spectrum, an incident power density of 1000 W m^{-2}, and a temperature of 25 °C [5].

Open circuit voltage and short circuit current. The e.m.f. which is developed at the isolated terminals (infinite load resistance) of an illuminated solar cell is known as open circuit voltage V_{oc}. In the opposite condition, zero load resistance, the terminals are connected together and the resulting current is called short circuit current I_{sc}. When an intermediate load resistance is present in the circuit, the resulting voltage is such that $V = IR_L$ and the current-voltage characteristic $I(V)$ of the cell depends not only on the load, but also on the spectrum of the incident radiation [5].

Photocurrent and quantum efficiency. The dependence of the photocurrent (at short circuit) on the spectrum of the incident light is expressed by the following relation (since the current is proportional to the illuminated area, we will rather refer to the short circuit current density, J_{sc}):

$$J_{sc} = q \int_0^\infty b_s(E) QE(E) dE \tag{1.2}$$

where q is the elementary charge, b_s is the incident spectral photon flux density, and $QE(E)$ is the quantum efficiency of the cell, which is the probability of generating an electron per incident photon as a function of photon energy. The quantum efficiency depends on the absorption coefficient of the material constituting the cell, and on the effectiveness of charge separation and collection [5].

Dark current. The reverse or dark current J_{dark}(V) of a PV cell is defined as the current generated by a potential difference which is developed when the cell terminals are connected to a load. It flows in the opposite direction to the photocurrent. As a matter of fact a solar cell is a p-n junction, and thus shows a rectifying behaviour; hence, it can be considered as a diode in the dark, for which the dark current density under an applied bias V is given by [5]:

$$J_{dark}(V) = J_0 \left(e^{qV/mk_BT} - 1 \right) \tag{1.3}$$

where J_0 is a constant, k_B is Boltzmann's constant and T is the temperature (K). In the ideal diode behaviour the ideality factor, m, which gives the actual depence of the dark current on V, is equal to 1.

Under the *superposition approximation*, which has been proven a reasonable approximation for many photovoltaic materials, the current-voltage characteristic of the cell results from the sum of the short circuit photocurrent and the dark current:

$$J(V) = J_{sc}(V) - J_{dark}(V) \tag{1.4}$$

where the photocurrent is positive, according to the sign convention for current and volt-

ages in photovoltaics [5]. It follows that the open circuit voltage, defined at the beginning as the maximum reachable potential difference between the separated terminals, corresponds to the potential difference when the two currents exactly cancel out: $J_{sc}(V) = J_{dark}(V)$. Therefore, for the ideal diode we have:

$$V_{oc} = \frac{k_B T}{q} ln \left(\frac{J_{sc}}{J_0} + 1 \right) \tag{1.5}$$

which increases with increasing light intensity. V_{oc} is defined so that the photovoltage occurs in forward bias, $V > 0$, and power generation is achieved when the voltage is between 0 and V_{oc}. At V > 0 the illuminated device acts as a photodetector, while at $V > V_{oc}$ the device consumes power to emit radiation [5].

Fill Factor and Efficiency. The power density of the cell is defined as the product:

$$P = J(V)V \tag{1.6}$$

At the cell's operating point the current-voltage product reaches its maximum, corresponding to a certain voltage value V_m and a certain current density J_m; this is also called the maximum power point. For optimal performances the cell should be operated with a load resistance which corresponds to this point ($R_L = V_m/J_m$) [5].
The squareness of the current density-voltage curve (Fig. 1.7) is described by the Fill Factor FF, which is defined as the ratio [5]:

$$FF = \frac{J_m V_m}{J_{sc} V_{oc}} \tag{1.7}$$

The efficiency η of a solar cell corresponds to the fraction of the power density delivered at the cell operating point with respect to the incident light power density P_s [5]:

$$\eta = \frac{J_m V_m}{P_s} = \frac{J_{sc} V_{oc} FF}{P_s} \tag{1.8}$$

where P_s is given by the integral of the emitted energy flux density (incident irradiance, $L(E)$) over the photon energy [5]:

$$P_s = \int_0^\infty L(E) dE \tag{1.9}$$

Real solar cells. At last, it is important to note that in real cells, the ideal behaviour is degraded by the presence of series and parallel resistances (Figure 1.8), which cause the dissipation of the produced power through the resistance of the contacts and through leakage currents around the sides of the device, respectively.

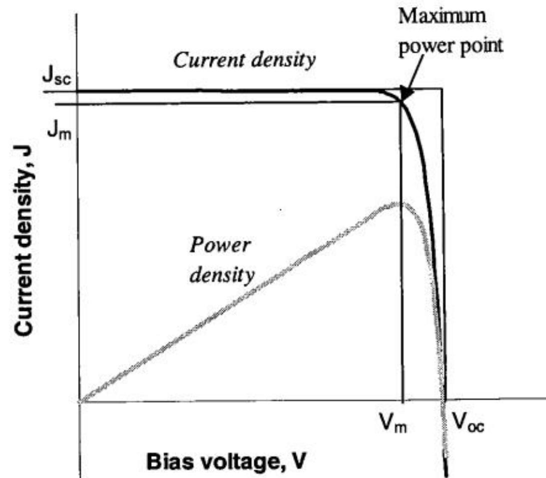

Figure 1.7: Current-voltage (black) and power-voltage (grey) characteristics of an ideal solar cell. The product of V_m and I_m is the maximum power density which is given by the area of the inner rectagle. The outer rectagle corresponds to the ideal case in which the fill factor is equal to 1 [5].

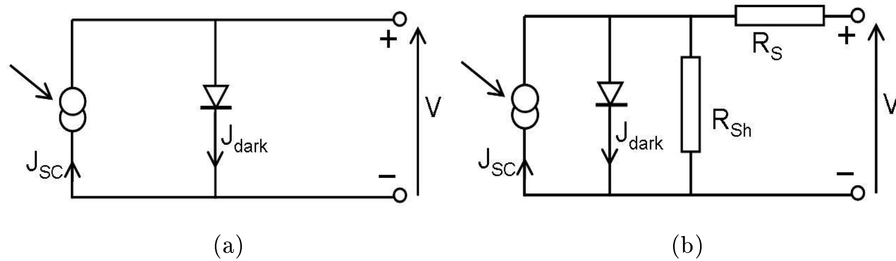

(a) (b)

Figure 1.8: Electrically, the solar cell is equivalent to a current generator in parallel with an asymmetric, non-linear, resistive element, i.e. a diode. The figure shows the equivalent circuit of (a) an ideal solar cell, and (b) a real solar cell with series (R_s) and shunt resistances (R_{sh}). J_{dark} is the dark or reverse current and J_{sc} is the short circuit photocurrent [5].

1.2.4 Detailed balance

As any body which absorbs light, photovoltaic converters exchange thermal radiation with the surrounding ambient, on account of their finite temperature. As a consequence, the efficiency of these devices cannot be infinite, and it can be evaluated considering the principle of detailed balance. The latter states that the rate of photon emission and photon absorption of the cell must be mutually counterbalanced, in order to have a constant steady-state electrons concentration in the material.
In the equilibrium condition, i.e. in the dark, a cell absorbs radiation only from the surrounding ambient, and, in turn, emits thermal photons by spontaneous emission, or radiative recombination, through which excited electrons relax to their ground state, in order to maintain the steady state [5]. The result of the detailed balance is therefore given by [5]:

$$\epsilon(E) = a(E) \tag{1.10}$$

where $a(E)$ and $\epsilon(E)$ are the probability of absorption and of emission of a photon of energy E, also known as absorbance and emissivity, respectively [5].
Under illumination, the electrochemical potential energy of the electrons is higher due to light absorption, and causes an enhancement of the light emitted by the cell. Because the net current density of the device results from the contributions of both the absorption and the emission of radiation, it is this unavoidable radiative recombination that ultimately limits the performances of the photovoltaic converter [5].

1.2.5 Maximum Efficiency

In order to evaluate the maximum efficiency of a photovoltaic converter, let us recall Eq. (1.2) for the short circuit photocurrent (density). Supposing the constituent material is a perfect absorber, providing no reflection of the incident light, we can thus assume that each photon with energy equal or higher than the bandgap of the semiconductor promotes one electron to the upper band (we do not consider multiple carrier generation). If we further suppose that perfect charge separation is achieved, i.e. zero radiative recombination of carriers occurs before they could reach the terminals of the device, the resulting photocurrent is the maximum for that band gap [5]. This can be expressed analitically as:

$$QE(E) = \begin{cases} a(E) = 1 & E \geq E_g \\ a(E) = 0 & otherwise \end{cases} \tag{1.11}$$

and

$$J_{sc} = q \int_{E_g}^{\infty} b_s(E) QE(E) dE \tag{1.12}$$

Photocurrent is then a function only of the bandgap and the incident spectrum [5].

According to Eq. (1.8), the power conversion efficiency of a solar cell can be written as:

$$\eta = \frac{V\ J(V)}{P_s} \tag{1.13}$$

where $J(V)$ is given by Eq.(1.4). Consequently, maximum efficiency is achieved when:

$$\frac{d}{dV}(J(V)\ V) = 0. \tag{1.14}$$

As for the photocurrent, the maximum efficiency of a photovoltaic cell depends thus on the spectrum of the incident radiation and on the band gap of the semiconductor. It is important to underline that, although J_{sc} increases with decreasing bandgap energy, the open circuit voltage must always be less than E_g/q (Eq. (1.5)); therefore, the maximum efficiency arises from a trade-off between the maximum reachable values of photocurrent and voltage.
For a standard spectrum η_{max} is around 33% at a band gap of 1.4 eV [5]. The Shockley-Queisser limit, corresponding to the optimum operating bias $V = E_g/q$ and collection of all carriers with $\Delta\mu = qV$, has a maximum around 44% at a band gap of 2.2 eV for a 6000 K black body Sun [5].

In conclusion, the design of an efficient solar cell entails the achievement of several key requirements: 1) selection of a semiconductor material with a bandgap well matched to the solar spectrum, as well as excellent light absorption, charge separation and charge transport properties; 2) optimization of the load resistance and minimization of shunt and series resistances; 3) minimization of optical losses due to reflection and/or shadowing of the surface of the cell [5, 13].

1.3 Three Generations of PV

Since the major breakthrough of the photovoltaic technology in the 1970s, silicon has been the most exploited material in the field: in 2015 (crystalline/multi-crystalline) Si-wafer based technology, the so-called "first generation", still accounted for about 90% of the total PV production [17]. The success of silicon arises from the fact that it is a non-toxic and abundant material, known for its good stability; also, its physical, chemical and electronic properties, have been widely explored in the microelectronic field for decades.

A "second generation" of thin film solar cells (TFSC) is based on polycrystalline or amorphous materials, e.g. CdTe, CuInGaSe (CIGS), and a-Si, which can be deposited directly onto large areas of cheaper materials, such as glass sheets, plastics, or metallic foils, thereby offering the possibility to cut down the production costs of the expensive silicon wafer. However, they do not show high performances (maximum efficiency of $\sim$ 21% for poly-Si) [28].

A "third generation" PV comprises a wide variety of innovative solar cell designs and

materials, still at a research and development stage. As an example, remarkable results have been obtained with muntijunction (MJ) solar cells ($\eta > 40\%$, Fig. 1.11) within the concentrator photovoltaics field, however this technology is far from reach large scale production due to the prohibitive costs of both materials and manufacturing [28].

According to the most recent efficiency chart of PV technologies by the National Renewable Energy Laboratory (Figure 1.11), single-juction solar cells provide the highest efficiencies among the commercial products: 25.6% for Si-wafer based devices (blue filled circles), and 29.1% for gallium arsenide (GaAs) based solar cells (purple dotted triangle) developed for space applications, both close to the Shockley-Queisser limit of 31% for this technology. Indeed, the achievement of higher efficiencies, together with cost-reduction, as well as long term reliability, remain the main challenge for large scale production of PV modules.

1.4 Silicon Heterojunction Solar Cells

Commercial single-junction solar cells based on crystalline silicon (c-Si) are usually fabricated with high quality p-type doped wafers. The p-n junction is realized by diffusion of PH_3 dopants onto the substrate to achieve n-type doping of the emitter. In addition, in order to avoid recombination of carriers at the rear surface, a back surface field (BSF) is usually obtained by creating a heavily boron-doped (p^+-type) region [17]. In this regards, this design is referred to as a homojunction, since it is all realized with the same material. The junction provides the separation of the charge carriers photo-generated in the absorber.
In order to reduce recombination losses, the passivation of surface defects is usually attained by means of a thermally grown layer of silicon oxide, at both the front and rear sides of the wafer. The top surface is coated with a SiN_x or TiO_x anti-reflective layer, and litography techniques are employed to realize particular surface patterns, e.g. inverted pyramids, with the double purpose to reduce surface reflection and enhance internal reflection on the rear side.
At last, the photo-generated carrier are collected by metallic electrodes on the top and bottom of the cell. On the front side, the contact with the absorber is made possible through small openings in the dielectric layer; here, recombination is reduced by creating a locally diffused region heavily doped underneath the contacts. An example of such structure is the passivated emitter with rear locally diffused (PERL) solar cell by the University of New South Wales (UNSW), which achieved an efficiency of 25% [17].

Nowadays almost half of the total cost of a PV module is dominated by the silicon wafer; indeed, the challenge for commercial cells for further cost-performance improvements is the enhancement of the conversion efficiency of the solar radiation, together with a decrease of the amount of material used per module, i.e. lower silicon usage per Watt of PV power [17, 2].

One of the major concerns of a technology based on thin films is related to the decrease of the output power of the cell that follows the reduction of the wafer thickness, which thus hinders the performance of the finished product. In fact, as the substrate is thinned down the amount of light that is absorbed is reduced, thereby resulting in lower values of J_{sc}. In addition, the reduction of the wafer thickness is followed by a drop of the V_{oc} of the cell, due to the enhanced recombination of the photo-generated carriers at the surface of the absorber [2]. Consequently, in order to achieve high-efficiency, the use of high-quality absorbers (optimal light absorption and high effective minority carrier lifetimes) and extremely efficient surface passivation are of prime importance.
Within this framework, the silicon heterojunction (SHJ) solar cell technology have demonstrated promising results, arising from the combination of the advantages of both the "first" (high performance of c-Si) and the "second generation" (thinner films and low cost manufacturing processes) PV technologies [2, 17].

The schematic representation of a particular SHJ solar cell, the so-called Heterojunction with Intrinsic Thin-layer by Sanyo (now part of Panasonic), is reported in Figure 1.9. Here, the passivation of both the top and bottom surfaces of the n-type c-Si wafer is attained with intrinsic hydrogenated amorphous silicon (a-Si:H) films (yellow layers in Fig. 1.9) deposited at room temperature by Plasma-Enhanced Chemical Vapour Deposition (PECVD).
The passivation mechanism, leading to the reduction of the a-Si:H/c-Si interface defect density, is attributed to the hydrogenation of the silicon dangling bonds on the wafer surface. The p-type emitter and the back surface field (red and green layers, respectively, in Fig. 1.9) are realized with subsequent deposition of boron-doped a-Si:H on the front side of the cell and an n-type a-Si:H film on the back side, respectively [3, 2]. The anti-reflective coating (light grey layers in Fig. 1.9), usually a transparent conductive oxide (TCO) film with low sheet resistance (3-100 Ω/sq), is deposited by Physical Vapour Deposition (PVD) on both sides of the cell, while the current collection is provided by means of screen-printed grid electrodes (dark grey contacts on top of the TCO layer in Fig. 1.9) [3]. This design has enabled to obtain a conversion efficiency of 22.8% and a V_{oc} of 743 mV for a 98-μm-thick practical size cell (100.3 m^2) [3].
Remarkably, the thickness of the c-Si substrate is about half of the current industrial standard for diffused-junction solar cells. In addition, the symmetrical structure of the HIT solar cell made it possible to create a bifacial module, which has been reported to have produced 10.9% more annual output power than the single-sided module [3].
The insertion of a wider bandgap passivating material between the highly recombination-active metallic contacts and the c-Si absorber surface appears to have been the key idea for the success of the SHJ technology. In fact, the heteroemitter stack of a SHJ solar cell acts as a semi-permeable membrane for the carrier extraction, simultaneously fulfilling two functions: the passivation of the c-Si surface and the collection the photo-generated carriers.

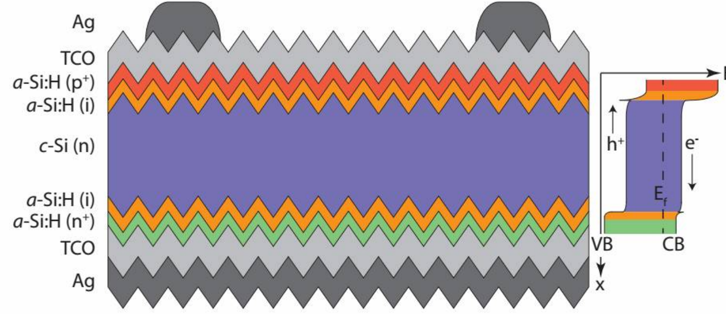

Figure 1.9: Schematic illustration of a SHJ solar cell (based on n-type c-Si wafer) as first developed by Sanyo, Japan (now part of Panasonic), including its band diagram. Structure is not drawn to scale [2].

In particular, it is the presence of the intrinsic a-Si:H films (HIT solar cell) that enables the record-high values of open circuit voltage and efficiency, as can be deduced from the trend of the effective carrier lifetime with the excess carrier density, reported in Figure 1.10 for three different heteroemitter stack designs (i/c-Si/i, ni/c-Si/ip, n/c-Si/p).
The poorer passivation quality (lower τ) of doped films may be attributed to doping-related defect generation at the interface with the substrate [2]. Nonetheless, doping of the films is essential to create the electric field that provides the separation of the photo-generated carriers, and which is thus absolutely necessary for the operation of the solar cell [5].

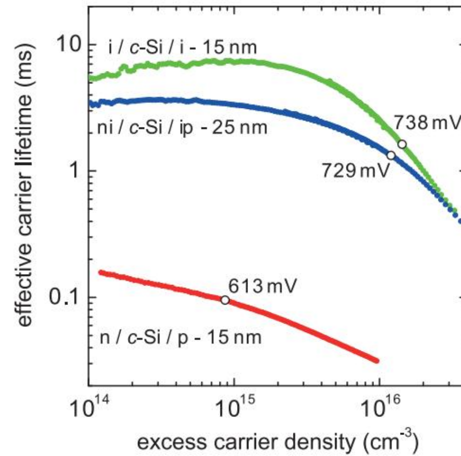

Figure 1.10: Effective carrier lifetime trends with excess carrier density for passivated wafers, including solar cell precursor, consisting of device-relevant a-Si:H stacks. The wafers are random-pyramid textured n-type FZ-Si, with a resistivity of about 3 Ω cm. The indicated voltages correspond to the implied-V_{oc} under 1 sun illumination [2].

Furthermore, it has been observed that low temperature annealing may result in an improvement of the passivation quality of the interface between the crystalline thin wafer and the amorphous layer [2]. The dependence of the effective carrier lifetime from the

annealing time can be expressed with sufficient accuracy by the following relation:

$$\tau_{eff}(t_{ann}) = \tau_{eff}^{SS}\left[1 - exp\left[-\left(\frac{t_{ann}}{\tau}\right)^{\beta}\right]\right] \tag{1.15}$$

where β is the dispersion parameter ($0 < \beta < 1$), τ_{eff} is the effective time constant, τ_{eff}^{SS} the steady-state value of τ_{eff}, and t_{ann} is the annealing time [2].

Notwithstanding amorphous silicon has been proven an excellent candidate for buffer layers, since it has a slightly wider bandgap with respect to c-Si, and can be easily doped both p- and n-type [2], the same material also shows strong parasitic absorption of light which causes a loss in short circuit current [4]. A solution which may lead to the improvement of the short circuit current, while simultaneously preserving high open circuit voltage, is represented by the incorporation of C, N, or O, into the amoprhous matrix, in order to widen the optical bandgap of the material. Si-rich hydrogenated amorphous silicon carbide a-SiC_x:H and silicon oxide a-SiO_x:H have both demonstrated good passivating properties; however, the efficiencies of SHJs based on SiC_x are not yet comparable with those obtained with pure amorphous silicon, while silicon oxide has been only investigated in its intrinsic form.

Recently, silicon oxynitride SiO_xN_y has demonstrated to be an appealing candidate for photovoltaic applications thanks to its high conductivity and the possibility of tunable bandgap and refractive index [4]. Therefore, the study of electrical and optical properties of this material is highly important in view of its use in SHJ solar cells, as it already showed improved passivating properties.
In particular, in this thesis we will report the investigation on the interface and surface properties of nc-SiO_xN_y:H thin layers deposited on silicon substrate conducted by means of surface photovoltage spectroscopy. Electrical characterization has been conducted as well, in order to evaluate the macroscopic conductivity of the films.

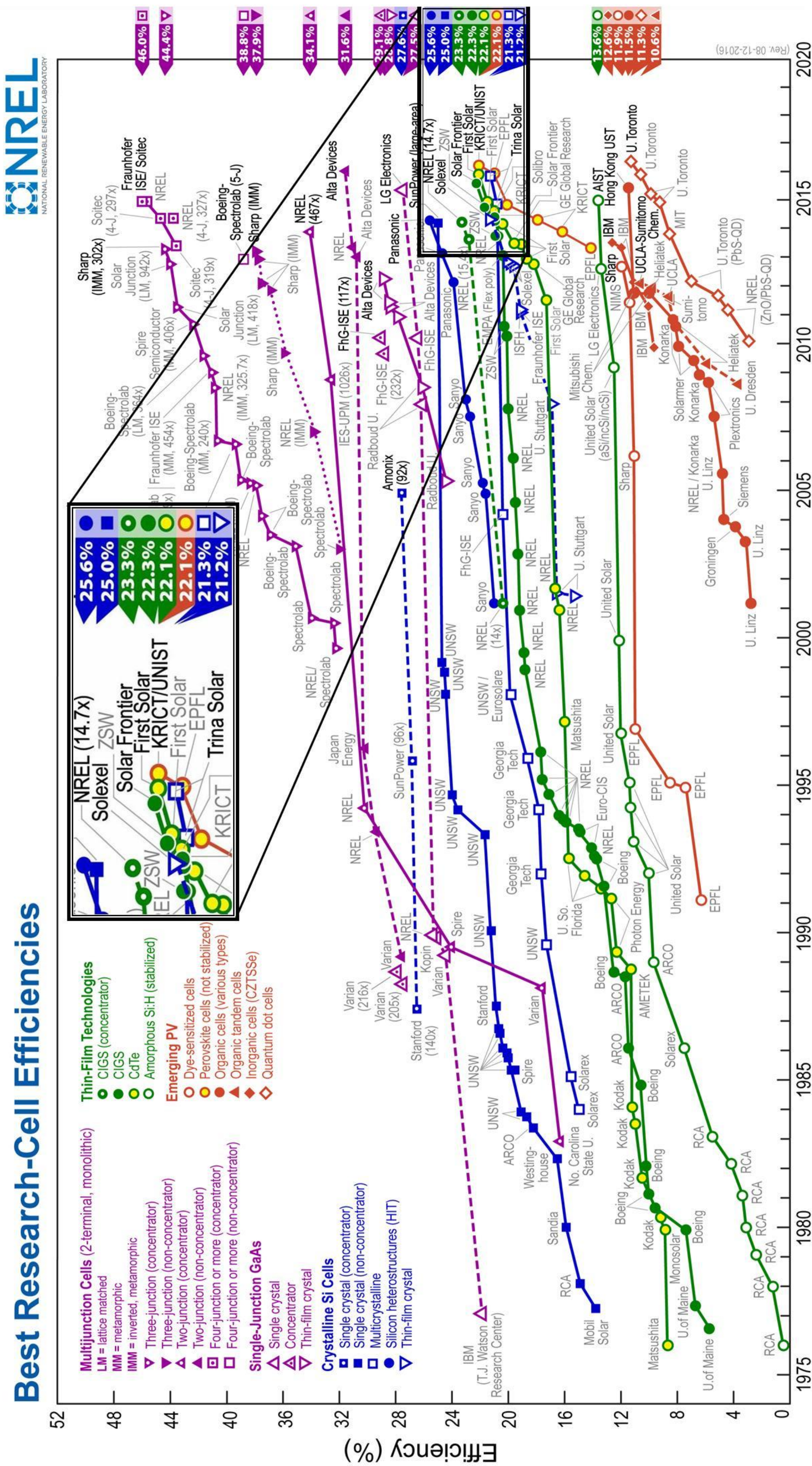

Figure 1.11: Chart of best research-cell efficiencies updated to 2016 [1].

Chapter 2

Surface Photovoltage Spectroscopy

The Surface Photovoltage (SPV) method is a contactless and non destructive technique for quantitative characterization of semiconductors, which involves light-induced variations of the band-bending to gain information on the electronic properties of the material [29]. In particular, Surface Photovoltage Spectroscopy (SPS) relies on the analysis of the surface voltage changes, both at the free semiconductor surface and buried interfaces, as a function of the incident photon energy [30]. Therefore, it allows the complete construction of the surface and interface band diagrams of the material, including defect states and quantum confinement structures, and also provides a detailed understanding of the semiconductor bulk properties (e.g. bandgap value and type, diffusion length and lifetime of charge carriers) [30, 31]. Since they both rely on optical absorption, SPS is often thought to be analogous to transmission spectroscopy; however, SPS does not require light collection and can thus be performed on arbitrarily thick samples, which need not to be removed from the substrate, nor to be grown on a transparent one [30]. In addition, it has been proven to be eminently useful for micro- and nano-crystallites, being inherently insensitive to reflection and scattering [30].
More generally, SPS measurements are practically ambient insensitive, and can be performed not only on clean surfaces, but also on real ones, at any reasonable temperature, and at any lateral resolution, down to the atomic scale [30].

The first studies on the illumination-induced changes of the semiconductor surface voltage date back to the early 1950s, with the pioneering work of Bardeen and Brattain [32, 29]. Thereafter, Johnson demonstrated that SPV measurements yield infomation on minority carrier lifetimes [33] and Goodman developed an algorithm for the extraction of the minority carrier diffusion length [34], in 1957 and 1961, respectively. Surface photovoltage spectroscopy was introduced a decade later by Gatos *et al.*, which conducted a systematic research on the effects of sub-bandgap illumination on the surface voltage [35, 29]. Furthermore, by successfully applying the method to study a great variety of semiconductors, Brillson [36], Mönch[37] and Lüth [38], among many others, contributed

to the popularization of SPS throughout much of the 1970s and 1980s. Starting from the 1990s, several groups worked to develop and improve other SPV-related methods and experimental tools, as well as algorithms for data analysis. In particular, Shapira's group, and more recently Pollack's group, have systematically applied SPS for quantitative studies of various semiconductor interfaces and heterostructures, including actual device structures [30]. Over time, SPS has become a well-established technique for the characterization of semiconducting materials, with numerous applications in the fields of surface electronic structure [29, 31].

The present chapter is intended to provide an insight on the SPV method and, specifically, on surface photovoltage spectroscopy. First of all, the physics of the surface photovoltaic effect is briefly explained in Section 2.1. Therafter, Sec. 2.2 is dedicated to the typical experimental set-ups available to perform SPV measurements, while several applications of SPS are discussed in the last section.

2.1 SPV: theoretical principle

2.1.1 Electronic structure of surfaces

The term "surface" is commonly used to define any boundary between two materials with different properties. Depending on the phase of the media involved, we refer to it as a "free surface", when a solid is surrounded by a gaseous phase or, in the ideal case, the vacuum; whereas, when two solids are in contact (e.g. two semiconductors in a heterostructure), it is said that they are separated by an "interface" [29].

The electronic structure of an ideal crystalline semiconductor arises from the periodic disposition of the atoms in the lattice, and it is characterized by allowed energy bands separated by forbidden energy levels. However, an abrupt termination of the periodic structure of the bulk crystal might cause the emergence of surface-localized electronic states within the forbidden bandgap and/or a double layer of charge, known as surface dipole [39, 30]. Precisely, the formation of the surface states can be ascribed to the alteration of the chemical bonding configuration at the semiconductor free surface when the periodicity breaks down [39, 30]. These changes typically result in uncompensated or "dangling bonds", since surface atoms have fewer neighbours than bulk atoms to bind to, steps and kinks at the surface, as well as absorption of impurity atoms. Moreover, surface reconstruction and relaxation phenomena may occur, in order to minimize the surface energy [39, 30].

Surface- or interface-localized states can have either acceptor or donor character, and whether they remain neutral or become positively or negatively charged, it depends on their energy position with respect to the Fermi level [39]. If they become charged, a flow of carriers is established between the bulk and the surface until the system reaches

thermal equilibrium [29]. According to the surface charge neutrality condition [39]:

$$Q_{SS} + Q_{SC} = 0 \tag{2.1}$$

a space-charge layer (SCR) has to be formed below the semiconductor surface so that its charge, Q_{SC}, exactly compensates the net surface charge, Q_{SS} [39]. As a consequence, the SCR has a non-zero electric field and the surface potential V_s differs from the electric potential far away in the bulk even under equilibrium conditions.
Three different regimes are to be distinguished for the SCR at the surface of either a p- or n-type semiconductor: *accumulation*, when the majority carrier concentration is larger at the surface than in the bulk; *depletion*, if the majority carrier concentration at the surface is smaller than its equilibrium value, but larger than the minority carrier concentration at the surface; *inversion*, when the majority carrier concentration at the surface is smaller than that of the minority carriers [29].

The potential drop across the SCR is manifested through the bending of the semiconductor bands in the vicinity of the surface [30]. Let us define the surface potential by means of the following expression [39]:

$$eV_s = E_V - E_{Vs} = E_B - E_{Cs} \tag{2.2}$$

where e is the elementary charge, E_V and E_C are the energy positions of the valence and conduction bands in the bulk, respectively, whereas E_{Vs} and E_{Cs} indicates the position of the same bands at the semiconductor surface. Thus, a positive value of V_s corresponds to downward-bent bands, and viceversa [29]. As an example, consider an n-type semiconductor in which acceptor-like surface states have developed within the bandgap, as shown in Figure 2.1a: since the acceptors are below the Fermi level of the doped semiconductor they charge negatively, resulting in a violation of the condition (2.1), as long as the bands remain flat up to the surface [39]. Surface charge neutrality can be re-established with an upward bending of the bands (Fig. 2.1b): in fact, as a consequence of the increasing distance between the Fermi level and the conduction-band edge towards the surface, the space-charge layer is depleted of mobile electrons and, thus, charged positively [39]. Conversely, a downward band-bending would lead to an accumulation of the majority carriers, thereby producing a SCR with charge of the same sign of the surface states, and, again, a violation of the charge neutrality condition [39]. The same arguments apply to a p-type semiconductor with donor-like surface-localized states (since acceptor states above the Fermi level would remain neutral), although the upward/downward bending of the bands must be inverted, as well as the signs of the charges Q_{SS} and Q_{SC} [39].
At last, when surface donors and acceptors are simultaneously present in the gap, surface band-bending will occur and a space-charge region of depletion type will be formed irrespective of the type of bulk doping.

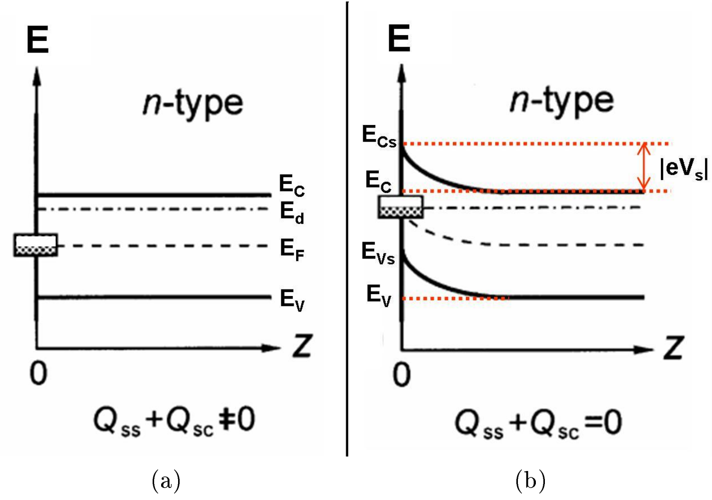

(a) (b)

Figure 2.1: (a) Non-equilibrium condition in the presence of charged acceptor-type surface states and (b) formation of a surface space-charge layer leading to charge neutrality, at an n-type doped semiconductor surface. E_F is the Fermi level of the n-type doped semiconductor, while E_i indicates the mid-gap position of the intrinsic Fermi level. Adapted from [39].

As mentioned above, another important phenomenon associated with a semiconductor surface involves the formation of surface dipoles. In this case, due to the extension of the "tail" of the surface-localized electron wave functions into the vacuum, a potential barrier for the electrons attempting to leave the semiconductor is formed at its free surface [29]. In addition, other microscopic dipole contributions may arise from reconstruction, stoichiometry changes or adsorption [30].

To better understand the difference between the effect of surface states and surface dipoles, let us introduce the concept of the local vacuum level E_l. It is defined as the energy of an electron at rest and free from the influence of any microscopic crystal potentials but not from macroscopic ones, e.g. the potentials due to the electric field at a SCR; hence, it must follow any changes in the electric potential along the sample [30]. Consequently, the electron affinity in the bulk, $\chi = E_l - E_c$, i.e. the amount of energy required to remove an electron from the conduction band at a point inside the crystal into the vacuum, may differ from the surface value χ^*, owing to the presence of a surface dipole $\Delta\phi_s$ [29].

This is illustrated in Figure 2.2 for a depleted p-type semiconductor, where it is also indicated the work function at the semiconductor surface in equilibrium, W_s, defined as the energy separation between the Fermi level E_F and the local vacuum level at the surface [29].

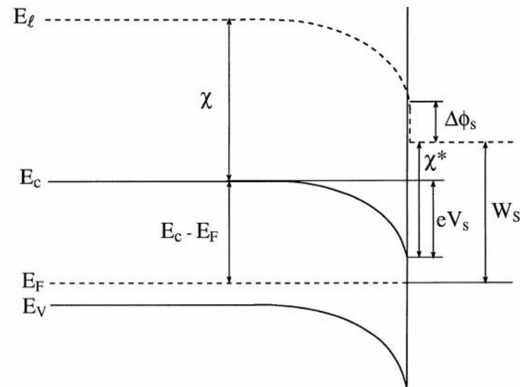

Figure 2.2: Schematic band diagram for a depleted p-type semiconductor free surface with surface dipole contributions $\Delta\phi_s$ [29]. The symbols are defined in the text.

2.1.2 The surface photovoltaic effect

In Chapter 1 we have seen that the operation of semiconductor devices which convert light into electricity is based on illumination-induced changes of the potential distribution of the material, i.e. the photovoltaic effect. Here, we describe one less familiar effect, i.e. the surface photovoltage, SPV.

Let us focus on the SPV induced at the free surface of a semiconductor sample with a grounded ohmic back contact. Even though the surface charge neutrality condition (Eq. (2.1)) remains valid, provided no external field is present, both the surface charge and the space charge may vary significantly under illumination [29]. In fact, the absorption of light induces the generation of electron-hole pairs by means of both band-to-band transitions and trap-to-band transitions, typically the dominant mechanisms for above and below band gap incident light, respectively [30].

The surface photovoltaic effect consists in an alteration of the band-bending due to the spatial separation of the injected carriers, by means of the electric field of the SCR [39]. The surface photovoltage is thus defined as [31]:

$$SPV = V_s(light) - V_s(dark) \tag{2.3}$$

Indeed, the net charge redistribution of the generated electron-hole pairs is a necessary condition for the formation of a SPV [29]. Sometimes, other minor mechanisms also contribute to the formation of free carriers, e.g. trapping of electrons or holes upon super-bandgap illumination, and Franz-Keldysh absorption, in which sub-bandgap photons induce band-to-band transitions via photon-assisted tunneling [30]. All the described transitions and the resulting evolution of the surface potential are illustrated for a depleted n-type semiconductor surface in Fig. 2.3.

At last, since both super-bandgap and sub-bandgap illumination-induced electronic transitions are generally hindered by a background of thermal transitions, decreasing tem-

peratures are very likely to lead to an enhancement of the SPV effect [30].

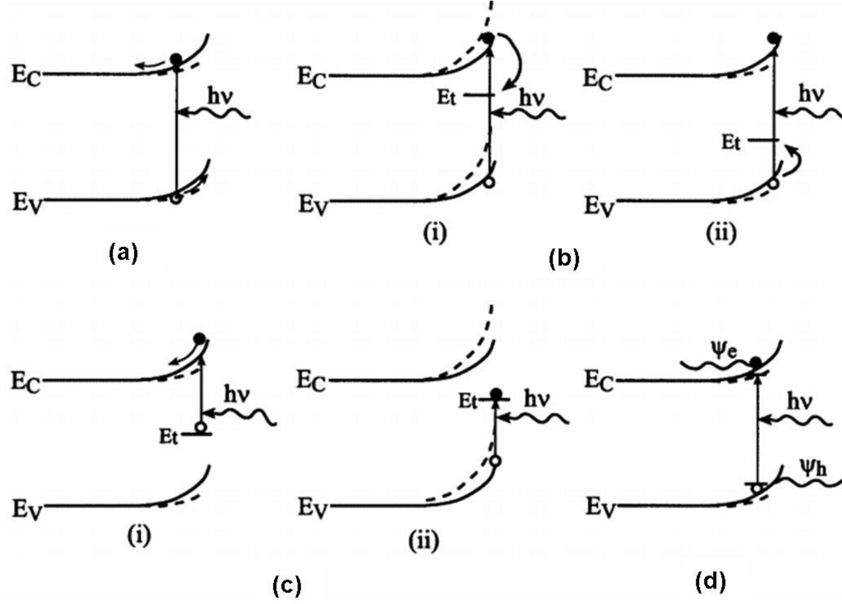

Figure 2.3: Illustration of the SCR at the surface of a depleted n-doped semiconductor under different conditions: (a) super-bandgap illumination with carrier separation due to an electric field; (b) super-bandgap illumination with preferential trapping of (i) electrons and (ii) holes; (c) sub-bandgap illumination with excitation of trapped (i) electrons and (ii) holes; (d) sub-bandgap illumination with Franz-Keldysh absorption, where ψ_n and ψ_p are the electron and hole wave functions, respectively. In all diagrams, solid and dashed lines are used to indicate the position of the bands in the dark and under illumination, respectively. Adapted from [29].

2.2 Experimental methods

The surface voltage cannot simply be measured with a voltmeter, since it is a built-in potential, nor it is possible to apply any sort of electrical contact, otherwise the surface properties would be inevitably altered. Consequently, many elaborate techniques for the determination of SPV have been developed and improved throughout the years [30]. In the following we will describe two methods, the Kelvin probe and the MIS configuration. Both of them present some advantages, yet, since they rely on different physical principles, each method proves to be suitable for the investigation of distinct phenomena.

2.2.1 The Kelvin Probe

As we have seen in Fig.2.2 in Sec. 2.1.1, any light-induced variation of the band-bending at a semiconductor surface is reflected in its work function. Therefore, provided no photo-chemical activity occurs to change the surface dipoles, the evaluation of the work function changes is equivalent to a direct determination of the SPV [30].

One of the oldest methods for measuring the difference between the work function of two materials involves the formation of a parallel plate capacitor [29]. Consider the schematic illustration of a capacitor with two metallic plates depicted in Figure 2.4. At first, the plates are isolated and the metals share the same local vacuum level, see Fig. 2.4(a). If now the metals are short-circuited as in Fig. 2.4(b), in order for their Fermi levels to achieve equilibrium, a charge transfer from the metal with smaller work function to the one with larger work function is established, thereby inducing an electric field within the gap of the capacitor. The corresponding potential drop in the local vacuum level across the gap equals the difference in the work functions of the two metals, i.e. $eV_{CPD} = W_1 - W_2$, and it is commonly known as the Contact Potential Difference (CPD) [29].
Ideally, knowing both the stored charge Q and the overall capacitance C_0, one would be able to calculate the CPD from the expression $Q = C_0 V_{CPD}$; however, the determination of the stored charge is a non-trivial issue [29]. In 1898, Lord Kelvin proposed a method for measuring the CPD directly, even if neither the stored charge nor the capacitance are known [40].
Basically, the Kelvin Probe method consists in the determination of the external bias that has to be applied in order to discharge the capacitor. In fact, under this condition, the Fermi levels of both the metals in our example would differ exactly by V_{CPD}, as in the isolated case, and there would be no need for the charge to be exchanged between the plates (Fig. 2.4(c)) [29]. To perform the measurements, the back surface of the semiconductor sample is ohmically contacted to a metallic reference electrode; since the work function of the metal does not vary upon illumination, the following relation can be assumed to be valid [29]:

$$- e \, \Delta SPV = \Delta W_s = e \, \Delta V_{CPD} \tag{2.4}$$

The Kelvin probe method has been applied to the determination of illumination-induced changes in work function since the 1950s, with the earliest experiments of Bardeen and Brattain [32], and nowadays it has become a wide-spread and well-established technique. In the modern configuration, a periodically vibrated plate is brought in proximity to the sample surface so that an AC capacitor is formed. Since the steady-state AC current can be zero if, and only if, the capacitor is discharged, in order to measure the CPD, it is sufficient to determine the DC bias for which the external AC current is nullified [29].

2.2.2 The Metal-Insulator-Semiconductor structure

The direct measure of the SPV can be achieved with an alternative approach based on a metal-insulator-semiconductor (MIS) configuration. Let us assume that the MIS capacitor is brought in open-circuit mode (disconnected terminals) after reaching equilibrium, and then illuminated [30]. Due to the photovoltaic effect, the surface voltage V_s may

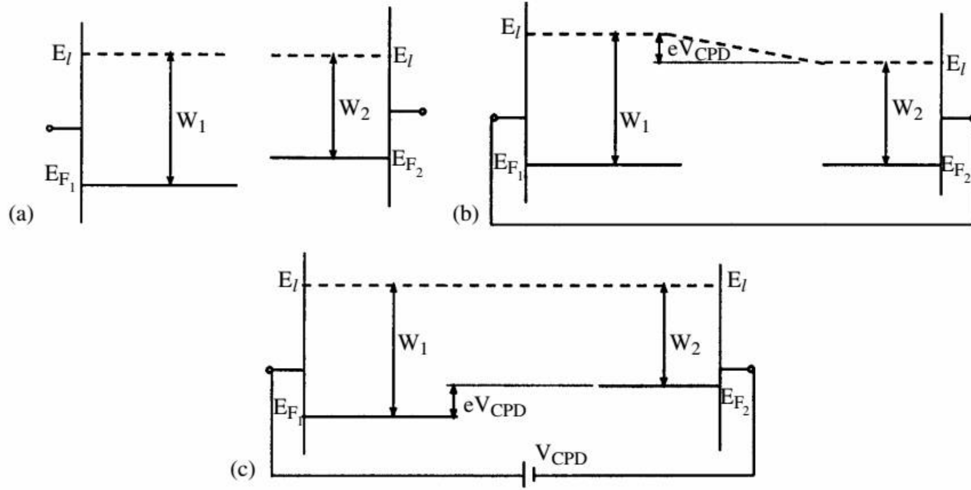

Figure 2.4: Schematic band diagram of a parallel plate capacitor in which the two metallic plates are (a) isolated, (b) short-circuited, or (c) connected through a DC bias equal and opposite to the contact potential difference [29].

vary upon illumination; correspondingly, a change in the external voltage measurable between the capacitor terminals must arise. Therefore, by measuring the photo-induced variation of the potential between the two capacitor plates, it is possible to determine the SPV (Eq. 2.3) at the semiconductor/insulator interface in a MIS structure [30]:

$$V_{meas} = SPV \tag{2.5}$$

It is believed that the first to employ the MIS technique for studying the SPV at a free semiconductor surface was Morrison in 1953. He was able to achieve contactless and non-destructive SPV measurements with a MIS structure in which a static platinum grid was placed in front of the sample, and where the insulator was simply air or vacuum, [29]. As long as it does not alter the surface properties of the semiconductor, the gap between the capacitor plates can be alternatively filled with an insulating spacer, e.g. mylar [29].
In Sec. 3.2.1 we provide a detailed description of the experimental set-up used in the present work, for surface photovoltage spectroscopy measurements in the MIS structure configuration.

2.2.3 Scanning SPV measurements

SPV mapping of semiconductor surfaces may be performed, with both the Kelvin probe method and the MIS approach, by scanning a small probe or a well-focused beam, respectively, across a surface. This technique has been proven useful, for example, for mapping surface and/or bulk contaminants on semiconductors and for carrier diffusion

length measurements [41]. The lateral resolution is typically of the order of ∼1 μm with both approaches [30]. Starting from the 1990s, SPV scanning measurements based on scanning tunneling microscopy (STM) and atomic force microscopy (AFM) have been succesfully implemented, allowing for even finer lateral resolutions [30].

2.3 Applications of SPS

From the previous sections emerges the unquestionable great potential of SPV-based characterization methods. In the following, we present an overview of the applications of SPS for the approximate determination of the bandgap energy and the semiconductor type, as well as the position of defect states within the bandgap, and the characterization of multilayer structures and actual devices.

2.3.1 Determination of semiconductor bandgap and type

As regards the extraction of the bandgap energy, SPS can be considered almost analogous to transmission spectroscopy, although not identical [30].
The absorption spectrum of most semiconductors is characterized by a significant increase of the optical absorption coefficient α near bandgap energy E_g, due to light-induced band-to-band transitions. Because the surface photovoltage is proportional to α, this increment is reflected in the SPS spectra (SPV as a function of the photon energy) as a sharp flank in the SPV curve near the photon energy of the bandgap, which often represents the most significant feature of a given spectrum [29, 38]. However, in order for super-bandgap SPV to be indicative of absorption, the following assumptions must be valid: linear dependence of the SPV on the light intensity, absorption length much larger than the diffusion length, and effective surface recombination velocity only weakly dependent on the light intensity. Provided such conditions are verified, E_g may be extrapolated quantitatively from the data, by means of a fitting procedure, using the simple relations [29]:

$$SPV \sim \alpha \sim (h\nu - E_g)^2 \tag{2.6}$$

$$SPV \sim \alpha \sim \sqrt{h\nu - E_g} \tag{2.7}$$

for indirect and direct bandgap semiconductors, respectively.
On the other hand, it is important to notice that the determination of E_g is usually only approximate. As a matter of fact, in SPV spectra the signal is observed to rise gradually up to a saturation value, rather than increasing sharply, in correspondence to E_g; the latter is thus determined by the energy position of the "knee" in the SPV curve [31]. The broadening of the super-bandgap SPV onset is caused by the absorption of photons with energy below the bandgap, as a consequence of the presence of band tails, i.e. shallow states extending from the band gap, and of the Franz-Keldysh effect [29].

Therefore, the exact position of the bandgap energy within the broad onset is not obvious and is usually affected by an error, which may be as large as 0.2 eV [29]. This observation is true even for clean surfaces of high quality single crystals, as clearly shown in Figure 2.5 [29]. At last, due to a strong decrease of the light penetration depth α^{-1} near the bandgap energy, electron-hole recombination processes might occur at the surface, resulting in the reduction of the SPV signal at photon energies $h\nu > E_g$ [31]. Hence, in some cases, a peak rather than a knee is observed [31].

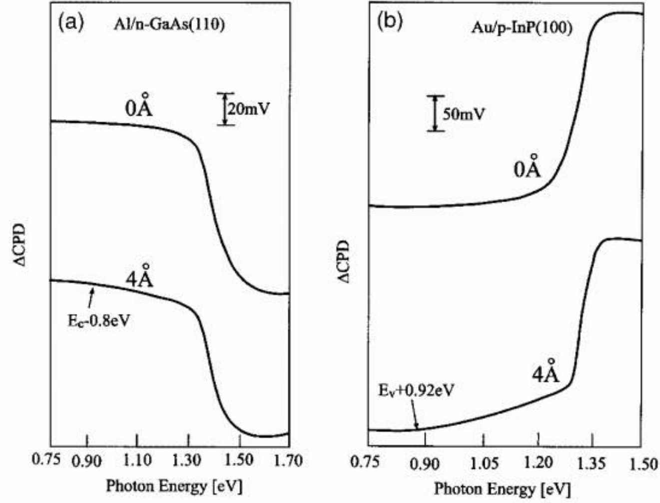

Figure 2.5: SPV spectra of (a) an n-type GaAs surface and (b) a p-type InP surface. In both graphs, the bottom curves refer to the measurements taken on the UHV cleaved surfaces, while the top curves resulted from the surfaces with an Al overlayer. From [30].

To understand how to extract information on the semiconductor type from SPS measurements, let us recall what has been stated in Sec. 2.1.2. Most semiconductor surfaces are usually depleted/inverted, i.e. the bands of a p-type semiconductor are bent downwards towards the surface ($V_s > 0$), while the bands of an n-type semiconductor are bent upwards ($V_s < 0$). Because super-bandgap illumination causes a decrease of the surface band-bending (Fig. 2.3), it leads to a positive SPV sign (negative ΔCPD) in n-type semiconductors and a negative SPV (positive ΔCPD) sign in p-type semiconductors. This behaviour can be distinctly observed in the examples of Fig. 2.5. Hence, the semiconductor type can be identified by observing the sign of the slope change associated with the SPV onset [30]. Note that, if the signal is collected by a lock-in amplifier, the root mean square (rms) value is usually calculated, so that the resulting sign of the SPV onset is positive (V_{meas}=|SPV|).
Therefore, SPS measurements can be be very useful for the determination of the type of unknown semiconductors, as well as to reveal ambient- and/or treatment-induced reversals of the conductivity of known films [29].

2.3.2 Detection of defect states and Urbach tails

Surface photovoltage spectroscopy has demonstrated, from the beginning, to be a valuable tool for the detection of surface and/or bulk defect states that may be present within the semiconductor bandgap, thereby allowing, for example, to obtain information on how a certain treatment affects the electronic properties of the material [30, 38].
Whenever the energy of the incident light is such to promote electronic transitions between a surface state and either the conduction or the valence band, a 'knee' emerges in the SPV curve [30]. More precisely, photo-induced excitations of electrons from occupied surface states to the bulk conduction band cause a positive modification of the surface charge Q_{SS}, i.e. a positive SPV (negative ΔCPD); conversely, if electrons are promoted from the bulk valence band into empty surface states (hole conductivity), Q_{SS} and the SPV become more negative (positive ΔCPD) [30, 38]. In a similar way as for the determination of E_g, thus, the analysis of SPV spectra may provide information on the energy position and type of surface states. In addition, SPS allows for the distinction between surface and bulk states, which is achieved by observing whether the pertinent spectral feature disappears after a surface or a bulk treatment [30].

As mentioned in the previous section, optical absorption for photon energies below the optical gap may occur between localized states extending from the energy gap, the so-called Urbach tails [42, 43]. The broadening of the onset of SPV spectra near the energy gap is an indication of the presence of tail states in the bandgap of the investigated material [29].
In amorphous semiconductors this effect is enhanced, because the distribution of the electronic states of the conduction and valence bands do not terminate abruptly at the band edges, due to the disorder present within the amorphous network [42, 43]. The breadth of the tail states, and consequently the broadening of the measured SPV, reflects the amount of disorder present within the amorphous material [29].

2.3.3 Characterization of multilayered structures

So far the SPV method has been only considered applied to the study of surface and bulk properties of semi-infinite, uniform bulk semiconductors. Nonetheless, in recent years, SPS has started to be employed for the study of heterojuctions, multilayer structures and actual device structures, on account of its sensitivity to buried interfaces [30].
Let us consider a sample consisting of a stack of one ore more semiconducting films, grown on a semiconducting bulk substrate, each of them characterized by different material parameters. The upper layers may have thicknesses of the same order of the diffusion length and/or the absorption length, so that excess carriers might be present near the rear surface as well. Because the energy bands of such structure are connected serially, the presence of any non-neutral region, may significantly influence the measured SPV signal, no matter how deep within the sample [30].

The sensitivity of SPS measurements to a certain region is only limited by the penetration depth of the incident photons; therefore, the measured SPV may result from the band-bending variations of both the SCR at the free surface and the SCR at the buried interfaces [30]. Of course, additional contributions to the SPV may also arise from quantum wells and other low-dimensional heterostructures, thereby revealing their presence within the sample [30].
An example is shown in Figure 2.6, which reports the SPV spectra of $Al_xGa_{1-x}As/GaAs$ laser structures with varied aluminium content in the active region. The contribution of the different layers can be clearly distinguished, in fact, in both curves two main features are present: one at 1.46 eV and 1.66 eV, respectively, corresponding to the two different active regions, and one at ~1.73 eV, which is related to the $Al_{0.30}Ga_{0.70}As$ barriers (located above and below the active region in the LASER structure) [44].

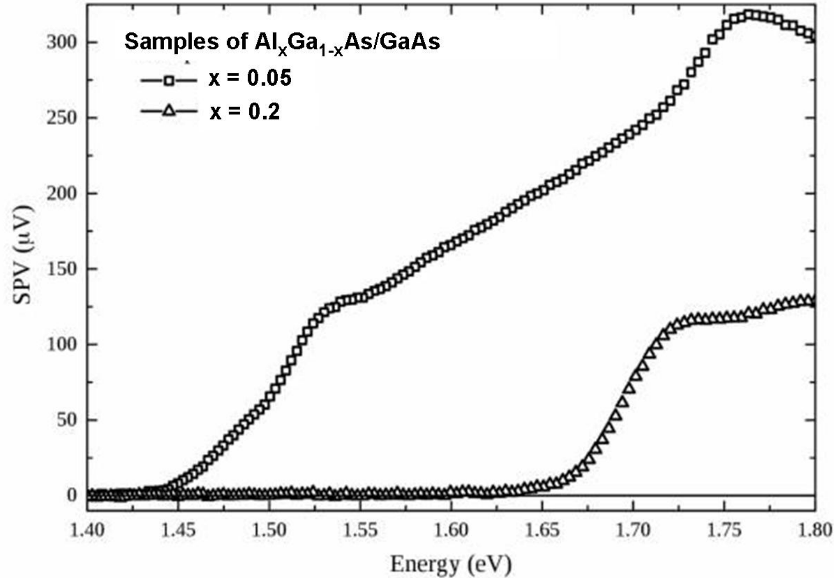

Figure 2.6: SPV spectra for two $Al_xGa_{1-x}As/GaAs$ laser diodes with different aluminium content (x) in the active region; energy peaks of the active region in each structure can be clearly differentiated [44].

In conclusion, by appropriate design of the experiments and interpretation of the results, sometimes in correlation with other methods (e.g. surface photo-conductivity, SPC, photo-luminescence, PL), SPS offers the opportunity to investigate how the surface and/or bulk electronic structure of semiconductors may evolve upon modification of the external conditions (temperature, humidity, etc.), variation of the composition, and other physical/chemical treatments.
Besides, one of the major advantages is represented by the possibility to perform contactless and non-destructive measurements, which makes SPS particularly valuable for the characterization of actual devices. Among the others, it has found many applications

for the prediction of the ultimate performance of solar cells, the identification of energy levels and lasing wavelength of LASER heterostructures, as well as the assessment of bandgap narrowing and ultimate gain of heterojunction bipolar transistors [30].

Chapter 3

Materials and Methods

This thesis aims to report the investigation of nc-SiO_xN_y:H thin layers deposited on c-Si and glass substrates, conducted by means of Surface Photovoltage Spectroscopy and electrical measurements. It specifically concerns on how the oxygen and nitrogen content and the crystalline fraction affect the film and the SiO_xN_y/Si interface properties. In the present chapter, the first section provides a summary of the properties known so far from previous studies on these materials. Then, the experimental methods and instrumental set-ups are described in detail in Section 3.2.

3.1 Materials

Silicon oxynitride is believed to represent a suitable candidate for PV applications, thanks to its excellent electrical and optical properties. It has been demonstrated an improved passivation quality and dark conductivity with respect to a-Si:H, the latest commercially used material in heteroemitter stack in the heterojunction solar cells (effective minority carrier lifetime of 2.5 ms, $\sigma_{n-type} = 4.5 \times 10^{-3}$ S/cm, $\sigma_{p-type} = 3.9 \times 10^{-4}$ S/cm) [4]. In fact, despite the high efficiency potential above 20%, a-Si heteroemitters and passivation layers present heavy parasitic absorption of light, which causes a loss in short circuit current [4]. The incorporation of oxygen and nitrogen into the amorphous matrix results in a wider optical bandgap (in this case, up to 2.2 eV), with a consequent reduction of parasitic absorption within the material, which could enable to achieve higher power conversion efficiencies [4]. Moreover, the combination of intrinsic and doped a-SiO_xN_y films with the c-Si base in SHJ solar cells resulted in a very high open circuit voltage of up to 733 mV [4]. Inasmuch as they exhibit higher conductivity and optical band gap values, as well as lower contact resistance to the TCO layer, further efficiency increase is expected from replacing the amorphous films with nanocrystalline ones [7].

The nc-SiO_xN_y:H thin films for the present study were prepared at the Department of Physics of the University of Konstanz, Photovoltaic Division. They were deposited

by Plasma Enhanced Chemical Vapour Deposition (PECVD) using a commercial system (PlasmaLab 100 from Oxford Instrument), in a parallel plate configuration [7].
Chemical vapour deposition, whose PECVD is one of the many variations, is a technique mostly employed for the deposition of thin layers on surfaces, for the fabrication of high-purity bulk materials and powders, and composite materials as well [45]. The deposition process starts with the flow of the reactants in vapour phase into a chamber containing one or more layers of material to be coated. Then, a chemical reaction between the precursor gases and the surface of the heated substrates is triggered by a different method depending on the CVD technique in use. The result is a solid deposit on the substrate surface. Finally, the unwanted chemical by-products formed during the reaction are neutralized and eliminated from the chamber by an exhaust-conditioning system and vacuum pumps [45, 46]. Alternatively to thermal CVD, that requires high temperatures to activate the reaction, in PECVD the ionization of the reactants is achieved by means of an RF o DC discharge between two electrodes. The resulting faster deposition rates and lower deposition temperatures represent a major advantage of this technique, since they yield improved uniformity of the deposited thin films and permit the coating of low-temperature substrates [46]. A schematic view of the PECVD system is presented in Figure 3.1.

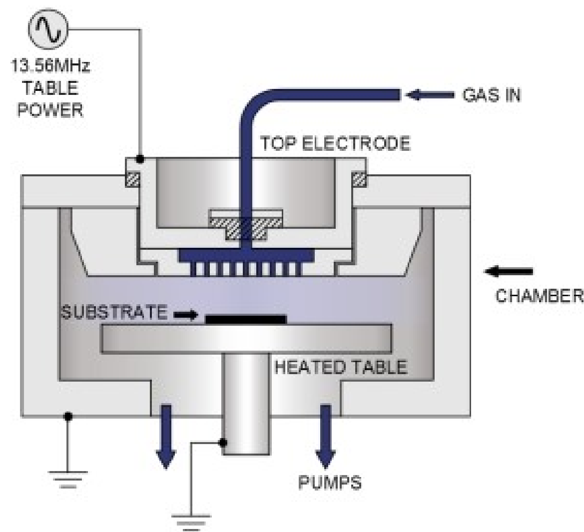

Figure 3.1: Schematic diagram of a PECVD reactor [47].

The investigated samples were deposited on Float Zone silicon (FZ-Si) and glass substrates at 300 °C, with radio frequency set at 13.56 MHz, deposition power equal to 5 W, and at pressure of 650 mTorr. As precursor gases, silane (SiH_4), nitrous oxide (N_2O), and hydrogen (H_2) were used, while diborane (B_2H_6) diluted in hydrogen (0.5%) was added to achieve p-type doping. Referring all the gases flows to their dilution in silane,

we indicate the diborane and nitrous oxide ratios as it follows:

$$R_{B_2H_6} = \frac{[B_2H_6]}{[B_2H_6] + [SiH_4]} \tag{3.1}$$

and

$$R_{N_2O} = \frac{[N_2O]}{[N_2O] + [SiH_4]} \tag{3.2}$$

respectively, where the square brackets indicate the gases concentrations. All the samples have been doped with $R_{B_2H_6} = 2.34\%$ [7]. Then, in order to obtain nanocrystals (NCs) formation, they have been annealed at 800 °C in nitrogen atmosphere [6]. Although the usual method, consists in providing an enhancement of the H_2 dilution during the deposition process, more compatible with PV technology, in this case a thermal treatment has been proven necessary, due to a technical limitation in the used PECVD system [6]. In this work we study the properties of the layers with the lowest N_2O dilution (3 h annealed and as-deposited) and with the highest N_2O concentration (3 h annealed). The deposition parameters and characteristics of the specimens are summarized in Table 3.1, where we have denoted the samples deposited on silicon and glass substrate by "_Si" and "_g", respectively, and the reported thicknesses are derived from ellipsometry measurements [6].

Table 3.1: Deposition parameters and characteristics of the SiO_xN_y thin films [7, 6, 8].

Sample (label)	Annealing (h)	R_{N_2O} (%)	Thickness (nm)	Crystalline fraction (%)	E_{Tauc} (eV)	σ_{dark} (S/cm)
C0h_Si	0	9	209 ± 5	67	1.80 ± 0.04	
C3h_Si	3	9	417 ± 5	88	2.5 ± 0.1	
C3h_g	3	9	209 ± 5	88	2.5 ± 0.1	44 ± 4
E3h_Si	3	47	283 ± 5	70	2.34 ± 0.08	
E3h_g	3	47	283 ± 5	70	2.34 ± 0.08	∼ 4

Structural Properties

In Figure 3.2a, a Scanning Electron Microscope (SEM) image shows the cross section of a similar sample ($R_{N_2O} = 16.7\%$, 3 h annealed, 224 nm thick): two different areas can be clearly distinguished, due to the presence of NCs in the SiON layer [7]. From High Resolution Transmission Electron Microscopy (HR-TEM) measurements on a different film ($R_{N_2O} = 28.6\%$, 6 h annealed), in Figure 3.2b, the absence of a preferred crystalline orientation after the annealing is evident, as the crystals form randomly throughout the layer. This is confirmed by the diffraction pattern in the inset, which also reveals the presence of an amorphous phase [6].
The values of the crystalline fraction χ listed in Table 3.1 were extracted from the Raman

spectra of the samples deposited on glass, and calculated from the following formula:

$$\chi = \frac{I_C}{I_C + I_A} \tag{3.3}$$

where I_C is the integrated area under the peak at 520 cm^{-1} and I_A is the integrated area of the peak at 480 cm^{-1}, corresponding to the crystalline and the amorphous components, respectively [6]. The comparison between the crystalline fraction of nc-SiO_xN_y samples with varying deposition parameters and annealing times has pointed out that the thermal treatment promotes the formation of the crystals. In particular, as depicted in the graphs of Figure 3.3, χ reaches the highest value of 88% for the C3h sample, then it saturates after the first annealing step. For the 3h annealed films, a decreasing trend with rising N_2O dilution has been observed. This behaviour can be attributed to an enhancement of the structural disorder of the layers, due to higher nitrogen and mainly oxygen incorporation within the amorphous phase [6]. In this regard, from Secondary-Ion Mass Spectroscopy (SIMS) it has been found that increasing R_{N_2O} leads to a linear increase of the oxygen concentration in the matrix, whereas the nitrogen content remains fairly constant [4].

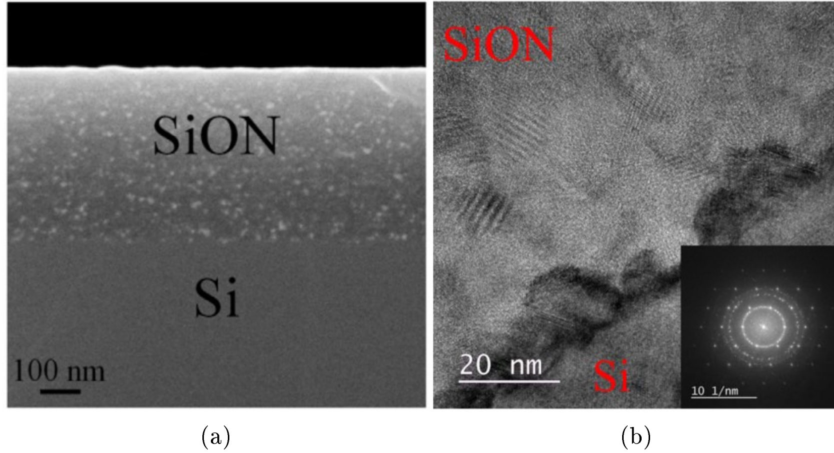

(a) (b)

Figure 3.2: (a) SEM image of a SiO_xN_y layer deposited with $R_{N_2O} = 16\%$, 3 h annealed [7] and (b) HR-TEM picture of a SiO_xN_y film deposited with $R_{N_2O} = 28.6\%$, 6 h annealed [6]. In the inset of (b) the diffraction pattern of the layer is shown.

Further analysis of Si-O-Si and Si-Si bonds from Fourier Transform Infrared (FTIR) spectra has confirmed these findings: for the as-deposited layers, in fact, the Si-O-Si peak intensity (i.e. integrated absorbance) rises with increasing R_{N_2O}, suggesting enhanced oxygen incorporation [6]. Also, the linear shift towards higher wavenumbers reveals a homogeneous distribution of the Si-O-Si and Si-Si bonds [6]. On the other hand, the peak position is observed to increase towards higher wavenumbers for all dilutions after the thermal treatment, yet its shift with R_{N_2O} is no longer linear. In addition, Perani

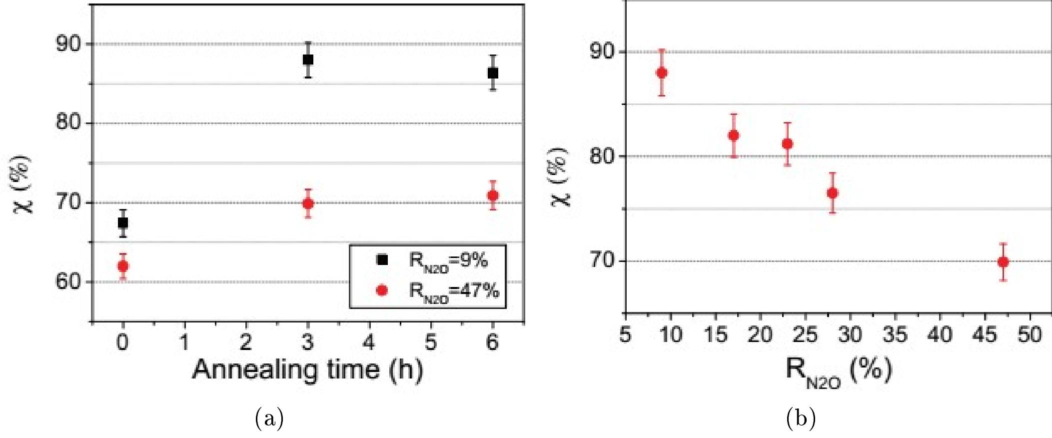

Figure 3.3: (a) Crystalline fraction depending on the annealing time, where the error bar corresponds to the error evaluated from the fitting procedure, and (b) crystalline fraction as a function of the N_2O dilution after 3 h annealing [48].

et al. [6] reported the appearance of a new peak in the 3h annealed state attributed to interstitial oxygen. Therefore, the annealing treatment is believed to promote the relocation of oxygen within the layers, leading to a phase separation of Si-rich and O-rich areas, as it was also evidenced by EDX measurements [48].

Optical and Electrical Properties

The optical properties of the nc-SiO_xN_y:H thin films deposited on glass were investigated by transmission $T(h\nu)$ and reflection $R(h\nu)$ spectra measurements in the range 300-1500 nm [6]. In particular, the absorption coefficient α was determined from the expression:

$$\alpha(h\nu) = \frac{1}{t}\, ln\left(\frac{1 - R(h\nu)}{T(h\nu)}\right) \tag{3.4}$$

where t is the thickness of the sample. The values of Tauc gap E_{Tauc} (reported as a function of N_2O dilution in Figure 3.4b) were extracted from the linear fit of the Tauc plots, obtained following:

$$(\alpha(h\nu) \cdot h\nu)^{1/2} \propto (h\nu - E_{Tauc}) \tag{3.5}$$

under the assumption of indirect band gap and disordered material [7].
A reduction of the absorption coefficient (calculated from ellipsometry data) with increasing N_2O dilution had already been observed in a-SiO_xN_y:H films [4]. The same decreasing behaviour seems to occur after the annealing [7], as can be seen in Figure 3.4a for a sample with $R_{N_2O} = 17\%$. In the as-deposited state, E_{Tauc} increases linearly with R_{N_2O}, due to higher oxygen content within the layers. No similar trend can be observed after the 3h annealing, yet E_{Tauc} becomes larger for all dilutions [6]. This finding could

be explained considering two different effects: the shift of the band gap of the material towards that of SiO_2 (9.3 eV [49]), following from the annealing-induced phase separation, and the formation of Si nanocrystals which can lead to quantum confinement (QC) effects [7, 6]. Increased dimensions of the NCs, and consequent reduced QC, could be the reason of the drop of the Tauc gaps after the additional annealing step [7].

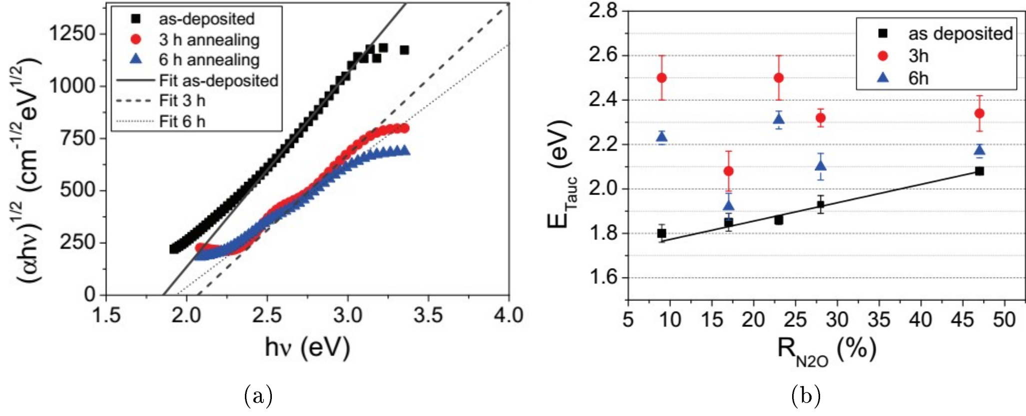

(a) (b)

Figure 3.4: (a) Tauc plot with linear fits of the data (solid, dashed and dotted lines) for the sample with $R_{N_2O} = 17\%$ at different annealing times [7]. (b) E_{Tauc} as a function of the N_2O dilution for different annealing times. The solid line is a linear fit of the data points relative to the as-deposited SiO_xN_y layers [6].

The graphs in Figure 3.5 report the lateral conductivity in the dark σ_{dark} as a function of the crystalline fraction χ, and σ_{dark} together with the prefactor σ_0 and the activation energy E_a, as a function of the nitrous oxide dilution R_{N_2O}. They were determined from room temperature IV characteristics and temperature-dependent conductivity measurements, performed on the samples grown on glass with titanium/palladium/aluminum contacts deposited by electron beam epitaxy [6]. σ_0 and E_a, the latter representing the amount of energy required for the conduction to occur, were extracted from the equation:

$$\sigma = \sigma_0 \; exp\left(-\frac{E_a}{kT}\right). \tag{3.6}$$

Similarly to χ, both σ_{dark} and σ_0 decrease as R_{N_2O} is increased, while E_a follows the opposite trend. According to these results, it can be concluded that increasing oxygen content improves the formation of the amorphous phase, thus preventing the conductivity of the films [6]. The highest values of both dark conductivity and band gap, up to 44 S/cm and 2.5 eV, respectively, have been measured for the nc-SiO_xN_y:H layer deposited with low nitrous oxide dilution and 3 h annealed (sample C3h in Table 3.1) [6].

Morphology and Conductivity at the nano-scale

The analysis of the surface of the nc-SiO_xN_y thin films on Si substrate conducted by Atomic Force Microscopy (AFM) has provided information on the morphological and electrical properties at the nano-scale.
First of all, the topography maps have clearly revealed the presence of grain-like structures on the surface of the samples [7, 8]. The evolution of the monitored parameters - including surface roughness (R_{HHCF}), lateral correlation length (ξ), and equivalent disk radius (EDR) distribution - indicate that larger grains are formed after the thermal treatment [7, 8]; moreover, changes in the AFM phase contrast maps could suggest that variations of the local composition occur on the surfaces of the samples [8]. In particular, a tendency of Si NCs to agglomerate forming clusters has been observed [7, 8], confirming that a phase separation does take place with annealing, as already evidenced by the evolution of the structural properties of the specimens discussed above. Furthermore, increasing R_{N_2O} causes the development of larger crystal aggregates; however, since the crystalline fraction of the layers decreases, it results in higher structural disorder [6].
Secondly, conductive-AFM measurements have pointed out that different surface morphology corresponds to peculiar electrical properties of the films, with differences in the measured local currents up to three orders of magnitude between the most and the least conductive samples [8]. As can be seen in the current maps in Figure 3.6, Si-rich nanocrystals with enhanced conductivity are embedded in an amorphous and less conductive matrix, mainly composed by oxygen [6, 8]. With respect to the C3h, in the samples C0h and E3h the grain distribution appears more uniform throughout the surface and leads to lower values of local conductance. On the other hand, the annealing-induced formation and clustering of the crystals result in improved conduction at the nano-scale for the sample C3h, being probably responsible for the enhanced macroscopic conductivity as well [8]. Current-voltage characteristics measured in several points of the surface support these findings; in addition, they have also allowed to verify the agreement with the model of back-to-back Schottky barriers, assumed for the tip/nc-SiO_xN_y/contact to the ground structure [8].
At last, from the conductance distributions as a function of negative and positive applied biases (Figure 3.6g) it can be deduced that the oxygen content prevents the activation of the dopants. The holes contribution to conduction prevails, in fact, only after annealing and for low R_{N_2O} (sample C3h) [9].

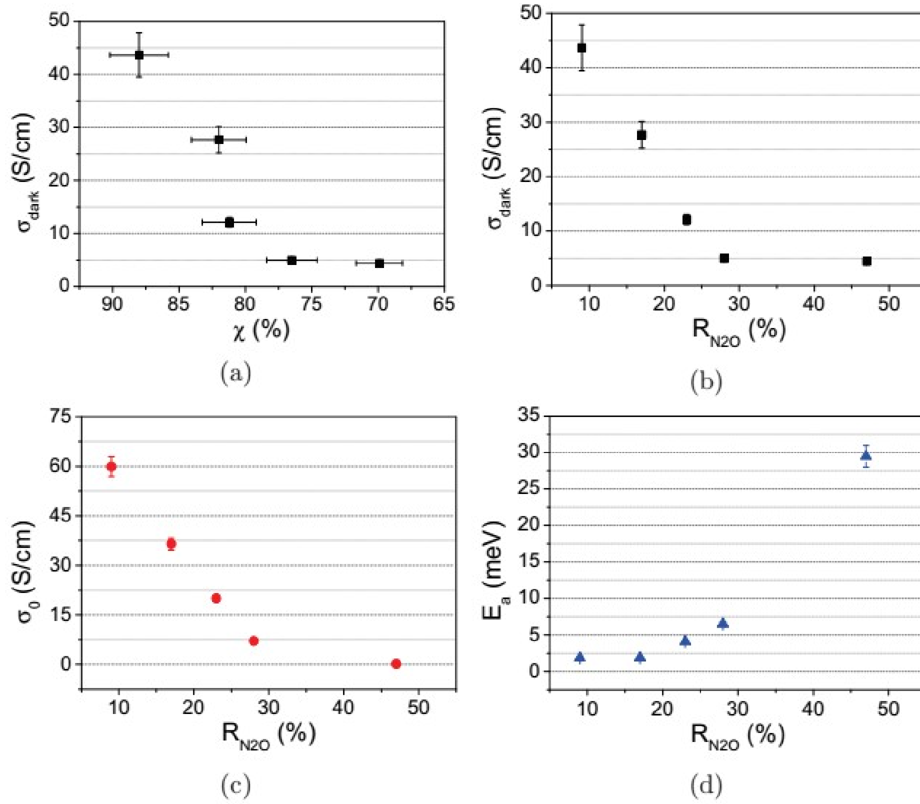

Figure 3.5: (a) Room temperature dark conductivity σ_{dark} of the samples 3 h annealed as a function of the crystalline fraction; (b) Room temperature dark conductivity σ_{dark}, (c) prefactor σ_0, and (d) activation energy E_a as a function of N_2O dilution after 3 h annealing [48].

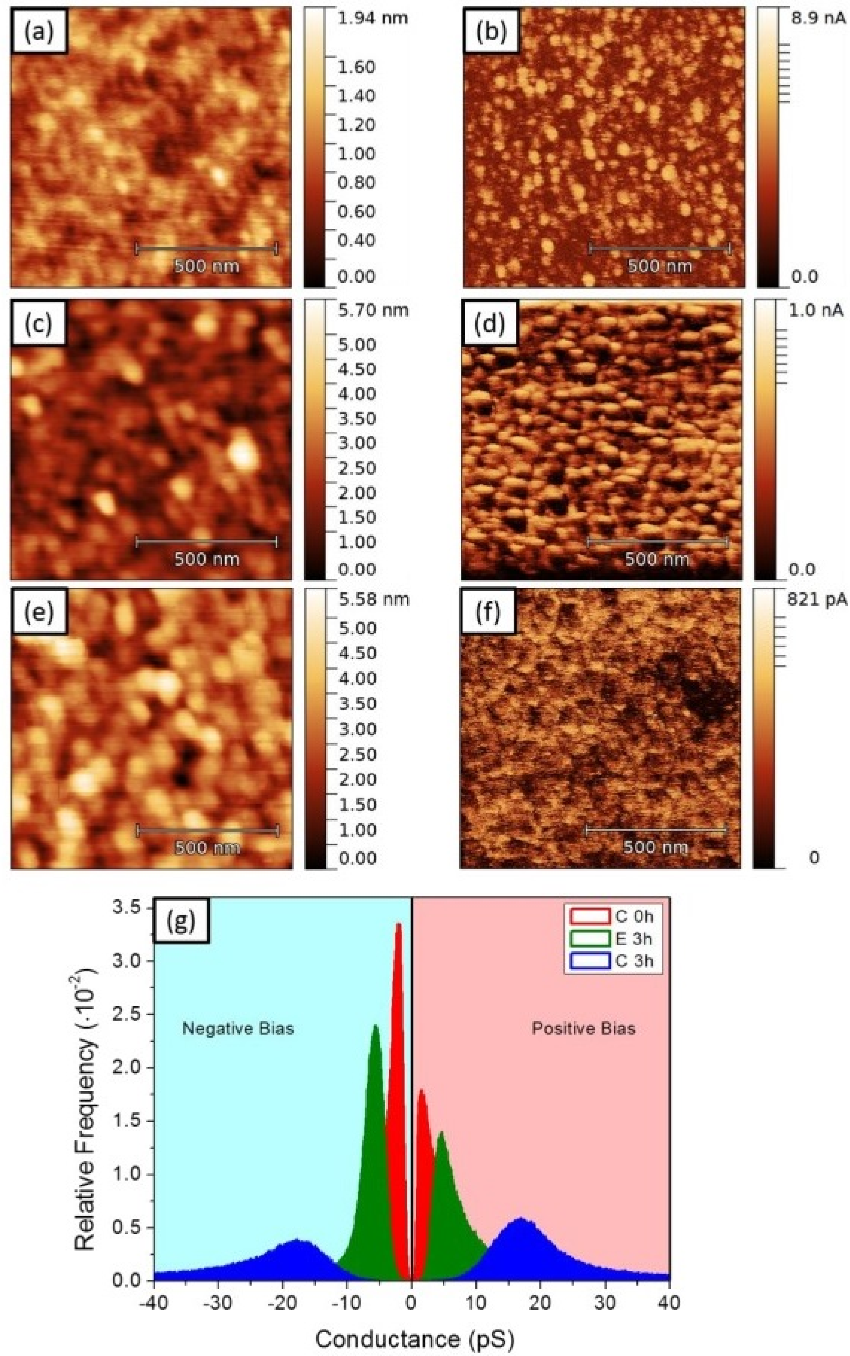

Figure 3.6: Morphology and current maps, respectively, of nc-SiO_xN_y thin films: (a)-(b) C3h at 0.1 V, (c)-(d) C0h at 1.5 V, and (e)-(f) E3h at 0.4 V. (g) Conductance distributions for C0h (red), E3h (green), and C3h (blue) samples for negative (light blue) and positive (light red) applied biases. Negative conductance values refer to negative applied voltages [9].

3.2 Experimental Methods

3.2.1 Surface Photovoltage Spectroscopy Apparatus

A schematic view of the experimental set-up used to perform Surface Photovoltage (SPV) measurements is depicted in Figure 3.7. In order to obtain spectroscopic measurements, a white light source has been employed in combination with a monochromator. A chopper placed just before the input entrance of the latter was used to provide the reference signal for the lock-in amplifier, which reads the signals from either the pyroelectric sensor or the SPV probe. Surface Photovoltage spectra have been measured in the MIS structure configuration, where the air plays the role of the insulator and either an ITO-coated glass or a metallic grid has been placed in front of the sample to act as transparent electrode. Both the set-ups have been used, the results have been compared and are presented in Section 4.2.
Silver conductive paste contacts both the sample and the probes to the system. In this case, the voltage signal reaches the lock-in amplifier after passing through a high output impedance FET pre-amplifier.
All the data has been acquired by means of the real-time software SPS_Data_Acquisition.vi, a LabVIEW Virtual Instrument previously developed to interface the SPS instrumental set-up [50].

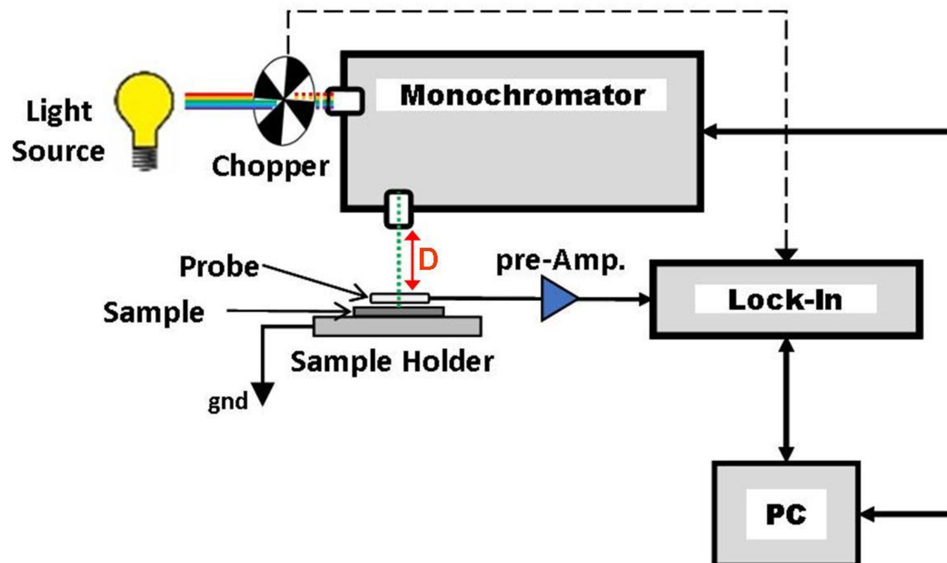

Figure 3.7: Block diagram of the Surface Photovoltage Spectroscopy experimental apparatus.

Light Sources

As continuum white light sources, a QTH (Quartz Tungsten Halogen) lamp and a short arc Xe (Xenon) lamp have been employed. The former consists of a quartz bulb which contains, together with a rare gas and small amounts of halogen, a tungsten filament able to emit light when heated at high temperatures. The spectral irradiance of a QTH lamp varies with the filament temperature, which in turn depends on the applied voltage (in our case, equal to 23 V) [51]. The Xe lamp is a gas discharge lamp, and produces light by passing electricity through ionized Xe gas at high pressure [52]. As can be seen in Figures 3.8a and 3.8b, both sources have a black body emission spectra, yet they show maximum emission at different energy values: around 1 eV for the QTH, and between 2 and 3 eV for the Xe lamp. Thus, the use of both types of lamps allowed spectroscopic measurements to be performed in a wide range of wavelengths.

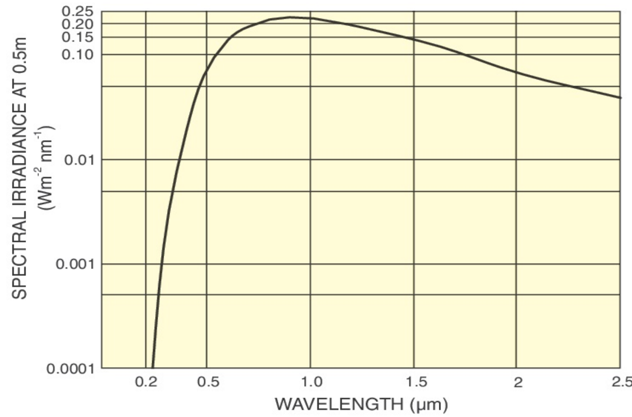

(a)

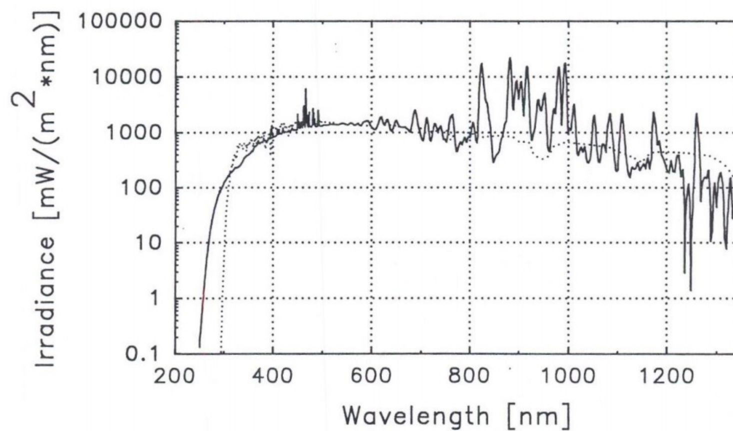

(b)

Figure 3.8: Spectral irradiance of (a) a 1000 W Quartz Tungsten Halogen lamp [51], and (b) a long arc Xenon lamp [52].

Chopper

The optical chopper used is a 300CD model by Scitec Instruments. It consists of a compact chopper head mounting a photochemically blacked non-magnetic disc, and a control unit which allows to set the frequency in the range between 5 Hz - 3 kHz [53]. Photon flux measurements have been conducted at low chopping frequencies ($\sim$ 13 Hz), whereas frequencies around 77 Hz have been shown to be the most suited to assure the stability of the signal during the acquisition of SPV spectra [50].

Monochromator

As monochromator we have used a SPEX 500M Czerny-Turner spectrometer by SPEX Industries, Inc. Here, the white light from the source enters the system through an input slit on the front and is collimated by a first mirror, while the actual separation into monochromatic components is accomplished by means of a plane diffraction grating. Then, after focusing on a second mirror, each wavelength is selected through a narrow exit slit, on the front or on the side of the monochromator. Illustrations of the spectrometer and of the Czerny-Turner configuration are reported in Figure 3.9.

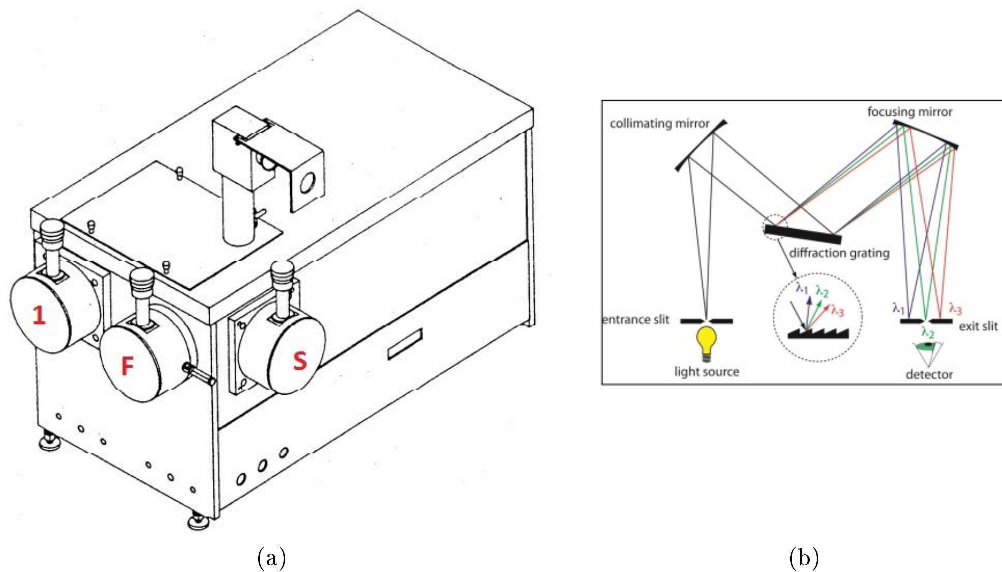

(a) (b)

Figure 3.9: Left, schematic view of the SPEX 500M monochromator [54]. Entrance slit, front and side exit slits are labelled as 1, $2F$, and $2S$, respectively; right, the Czerny-Turner configuration [55].

A diffraction grating is a dispersive element consisting of a reflective surface carved into parallel and equally spaced grooves, each of which emits light at all angles, acting as a secondary light source. Let's consider the geometry in Figure 3.10a, the condition for constructive interference of two parallel rays incident at an angle α on two adjacent

grooves, and diffracted at β, is satisfied when the geometrical path difference equals an integral multiple of the diffracted wavelength λ. This is expressed through the equation of the grating:

$$d(\sin\alpha - \sin\beta) = n\lambda \qquad n \in \mathbb{Z} \tag{3.7}$$

where the angles are measured from the grating normal, d is the groove spacing, also called the grating parameter, and n is the diffraction or spectral order. Since the condition $|\sin\alpha - \sin\beta| > 2$ has no physical meaning, equation (3.7) and $|n\lambda/d| < 2$ restrict the possible diffraction orders (or angles) to a finite number [56].
Figure 3.10b refers to a particular condition called the *blaze condition*, which is fulfilled when the diffracted ray is reflected at the same incident angle from the facet normal. Under this circumstance, the following equation stands:

$$n\lambda = 2d\sin\theta_B \tag{3.8}$$

where θ_B is called the blazing angle and represents the angle at which the grating diffraction efficiency is maximal, provided the grating is used in Littrow configuration ($\alpha = \beta = \theta_B$) [56]. Since to a given blazing angle corresponds a blazing wavelength λ_B, the spectral efficiency of a diffraction grating varies with the wavelength. In the

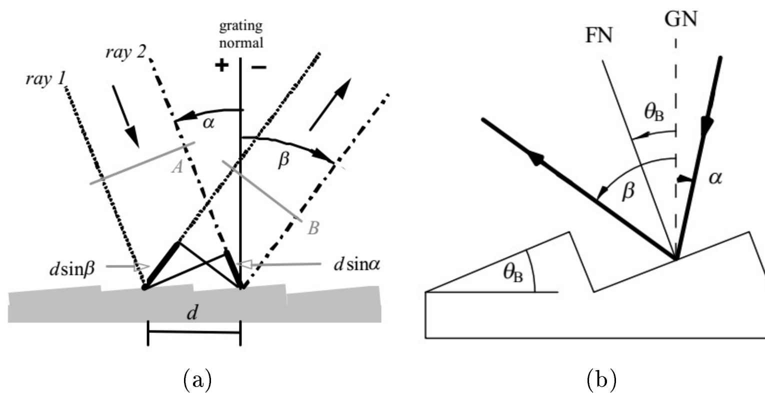

Figure 3.10: Geometric illustrations of (a) a reflective diffraction grating and (b) the blaze condition, from [56].

present case, two diffraction gratings with groove density of 600 gr/mm and different blazing wavelengths of $\lambda_B = 300$ nm and $\lambda_B = 1500$ nm have been employed, allowing us to choose between the two, depending on the photon energy range of interest for the measurement.
A ministep driver provides the rotation of the stepping motor on which the gratings are mounted, so that the wavelength of the beam hitting the detector can be varied by changing the grating plane in respect of the incident and diffraction directions. On the side of the SPEX, values to 0.1 Å indicated by a needle-point at right and white marks

can be read on a 5-digit mechanical counter (total range of $0 - 30000$ Å). Since the counter is set to read true only for 1200 gr/mm gratings, in this case all values must be multiplied by a factor of 2 [54].
Even though the light source at the entrance is purely monochromatic, a spectral broadening (effective bandwidth) of the wavelength will always exist at the output of a real spectrometer. The finite width of the line profile, that is the FWHM of the recorded trace, is called instrumental line profile or bandpass (BP), and represents a measure of the instrument's ability to isolate adjacent spectral lines. Assuming the monochromator is not used at the limit of its resolution (0.02 nm [54]), which is usually the case, the width of the slits can be considered the dominant factor of the bandpass. Therefore, the latter results from the convolution of the two functions $\Delta\lambda_1$ and $\Delta\lambda_2$ (as illustrated in Figure 3.11), defined as the product of the linear dispersion (D)[1] and the width of the entrance and exit slits (w_{in}, w_{out}) respectively [57]. If the slits are perfectly matched, then $\Delta\lambda_1 = \Delta\lambda_2 = \Delta\lambda$, $|\Delta\lambda_1 - \Delta\lambda_2| = 0$, and $\Delta\lambda_1 + \Delta\lambda_2 = 2\Delta\lambda$. So the FWHM is half the base of the peak and can be approximated as:

$$BP = FHWM \sim D \cdot w \tag{3.9}$$

where w corresponds to whichever is greater between w_{in} and w_{out}, in the present case $w = w_{in} = w_{out}$ [57]. Note that a trade-off is always necessary to obtain the maximum throughput without loss of bandpass, because widening or narrowing the aperture of the slits affects not only the FWHM of the line profile, but also the magnitude of the photon flux at the exit of the instrument.

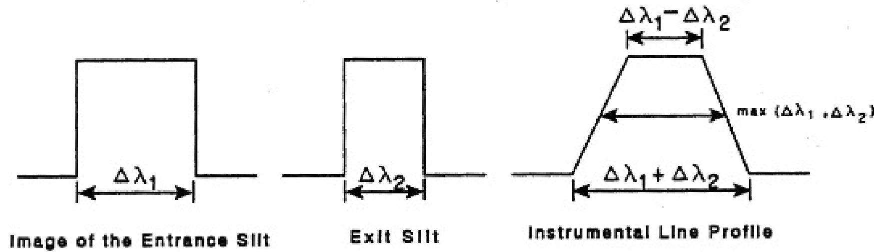

Figure 3.11: Instrumental line profile as the convolution of the entrance and exit slits functions $\Delta\lambda_1$ and $\Delta\lambda_2$ [57].

The linear dispersion of the SPEX mounting a 600 gr/mm grating is equal to 3.2 nm/mm [54], therefore, the uncertainty associated to the wavelength of the radiation at the exit slit is given by:

$$\Delta\lambda = 1.6 \cdot w \ (nm) \tag{3.10}$$

The width of the entrance and exit slits may be varied from 3 μm to 3 mm, calibrated in 2 μm by means of a micrometer-type knob above each of them. Moreover, it is also

[1] "The extent to which a spectral interval is spread out across the focal field of a spectrometer" [57].

possible to set the height of the two apertures to three different values (0.2 mm, 1 mm, or 2 mm) [54].

Pyroelectric Sensor

Since the QTH and Xenon lamps have a non-constant photon flux, their light intensity spectra were acquired in advance, in order to be able to normalize the SPV spectra accordingly. These measurements have been performed by means of a pyroelectric sensor, which has a response proportional to light intensity, but independent of the wavelength. Such detector is fabricated as a small capacitor in which the dielectric is a pyroelectric material, that is an asymmetric crystal in which the atoms have an internal electric dipole moment. When a temperature change occurs, it is followed by a variation in the position of the atoms within the crystal, as well as a change of the polarization of the material, leading to the generation of a voltage between the capacitor plates [58].
As already mentioned above, the reference frequency for the light spectra measurements is chosen around the value of 13 Hz, since the detectivity of a pyroelectric sensor is higher at low frequencies.

Lock-in Amplifier

The signals from either the pyroelectric sensor and the SPV probe have been collected by the Stanford Research System SR830 DSP Lock-In Amplifier of Figure 3.12.
Lock-in amplifiers detect very small AC signals even when a larger surrounding noise signal is present. Based on the Phase Sensitive Detection (PSD) method, such instruments are able to measure only the component of the signal at a specific reference frequency and phase, while rejecting all the noise components at frequencies different from that of the reference.
Let us assume that the voltage signal at the lock-in input is given by the sine wave $V_{sig} \sin(\omega_r t + \theta_{sig})$ and that $V_L \sin(\omega_L t + \theta_L)$ is the lock-in reference, here provided by the chopper. In the Digital Signal Processor (DSP), the phase sensitive detector multiplies these two waves and a low pass filter computes the average of the result over a time longer than the period of the two functions. As a consequence, a non-zero DC signal is obtained if $\omega_r = \omega_L$, whereas all the other components are removed. In a dual-phase lock-in, the signal amplitude V_{sig} is measured by computing the quantity $R = \sqrt{X^2 + Y^2}$, where $X = V_{sig} \cos(\theta)$ and $Y = V_{sig} \sin(\theta)$ are the 'in-phase' and the 'quadrature' components respectively, the latter being the product of the signal by the reference oscillator shifted by 90°, while θ is the phase between the signal and lock-in reference [59].
The low pass filter bandwidth and roll-off determine the attenuation of the noise. The SR830 Lock-In Amplifier allows to select the number of filtering stages after the DSP up to four, from 6 dB/oct to 24 dB/oct of roll off, as well as to adjust the bandwidth by setting the time constant (from 10 μs to 3 ks, detect. freq. < 200 Hz). The ratio of

Figure 3.12: Stanford Research System SR830 DSP Lock-In Amplifier, from [60]

the largest tolerable noise signal to the full scale signal defines the dynamic reserve of the instrument, which can be also adjusted by setting the dynamic reserve mode (Low, Normal, High) and the sensitivity of the measurement (2 nV - 1 V) [59].

Data Acquisition Software

The LabVIEW software SPS_Data_Acquisition.vi [50] controls the data acquisition of the Surface Photovoltage Spectroscopy measurements.
In the program Front Panel the user is able to select the wavelength range and increment of the spectrum, and to set the lock-in parameters, including sensitivity, time constant, dynamic reserve mode, low pass filter slope, and filtering mode. There is also the possibility to add some notes, such as the lamp used, the width of the entrance and exit slits of the monochromator, and the blazing wavelength of the grating. The point-by-point acquisition is shown in a Voltage vs Wavelength graph, updated and rescaled in real time after the program performs the stability check of the signal. In fact, each collected value results from the average of 5 consecutive acquisitions, provided they do not vary greater than 8%; otherwise, if the signal does not reach stability after 25 seconds, the *mean mode* is activated and the average is calculated on the last 10 values. At the end of the process, the data is stored in a file containing the wavelength (nm), the signal's 'in-phase' and 'quadrature' components X(V) and Y(V), module R(V), and phase theta(deg), the reference frequency(Hz) of the chopper, and the waitForStable(unit=time constant) value. The latter parameter indicates the number of time constants the program waits for the signal to be stable enough to be acquired [50].

Data Analysis

The light intensity of both lamps used to perform the measurements is not constant with the energy of the incident photons (reported in Chapter 4); moreover, the lamp flux and the SPV signals are collected using two different devices.
Therefore, the following expression has been used to normalize the raw data, in order to

obtain reliable information about the SPV spectral response of the samples:

$$SPV_{Norm} = \frac{SPV_{Raw}}{\Phi/h\nu} \tag{3.11}$$

where SPV_{Raw} is the signal as it is measured by the lock-in amplifier (i.e. V_{meas}), Φ is the photon flux measured by the pyroelectric sensor, and $h\nu$ is the energy of the incident photons.

Furthermore, since the main features of the SPV spectra are represented by slope changes, these points can be better distinguished in the numerical derivative of the normalized SPV. Indeed, the maxima and minima in the derivative spectra allow to easily indentify the energies corresponding to the electronic transitions [44, 29]. Assuming that the SPV signal is proportional to the open-circuit voltage, it follows that SPV $\propto V_{oc} \propto \alpha/h\nu$, then [44]:

$$\frac{d\left[SPV_{norm}(E)\right]}{dE} = \frac{d\alpha}{dE}. \tag{3.12}$$

3.2.2 Electrical Characterization

The macroscopic electrical properties of the nc-SiO_xN_y:H thin films have been investigated by means of the analysis of their dark current-voltage characteristics, acquired at room temperature.
As long as Ohm's law $V = IR$ is valid, the resistance R of a samples may be calculated from the linear fit of the I-V curves as:

$$R = \left(\frac{dI}{dV}\right)^{-1} \ (\Omega) \tag{3.13}$$

where I is the current that flows through the device under test (DUT) when a potential difference V is applied, provided a two-point probe (2PP) set-up is adopted. On the other hand, in a four-point probe (4PP) configuration the measured quantity is usually the potential difference generated between the inner contacts of the sample, when a current source is connected to the outer pair of probes. Both configurations are schematically reproduced in Figures 3.13a and 3.13b. Since the resistance depends on the structure of the DUT, it may be used to calculate the resistivity ρ (or, alternatively, the conductivity σ), in order to evaluate the intrinsic behaviour of the material. For 2PP measurements, ρ can be expressed by the following equation:

$$\rho_{2PP} = R_{2PP}\frac{D\ t}{L} \ (\Omega\ cm) \tag{3.14}$$

with D representing the length of the contacts, L the distance between the two, and t the thickness of the specimen (ref. Fig 3.13a) [61]. In the case of the 4PP configuration, the resistivity yields from the approximation of an infinite sheet with thickness t much

smaller than the distance between the contacts s [62]:

$$\rho_{4PP} = R_{4PP} \frac{\pi t}{ln(2)} \ (\Omega \ cm) \tag{3.15}$$

The conductivity is defined as the reciprocal of the resistivity $\sigma = 1/\rho$, and it is measured in S/cm.

Two-point probe and four-point probe measurements were performed with a 2614B System SourceMeter and a 2400 Keithley SourceMeter, respectively, by Keithley Instruments Inc. [63, 64]. In the first case, the instrument was interfaced with an acquisition software, by means of which the user can set various parameters, including the input voltage range and the voltage increment. A current-voltage graph is shown and updated automatically during the point-by-point acquisition, and at the end the data is stored in a file for further analysis.

For two-point probe measurements the samples were deposited on borosilicate glass, with titanium/palladium/silver contacts deposited by electron beam evaporation, then sintered in nitrogen atmosphere for 90 minutes at 150 °C [4]. High conductive silver paste was used to make the contacts for 2PP and 4PP measurements on the samples deposited on silicon.

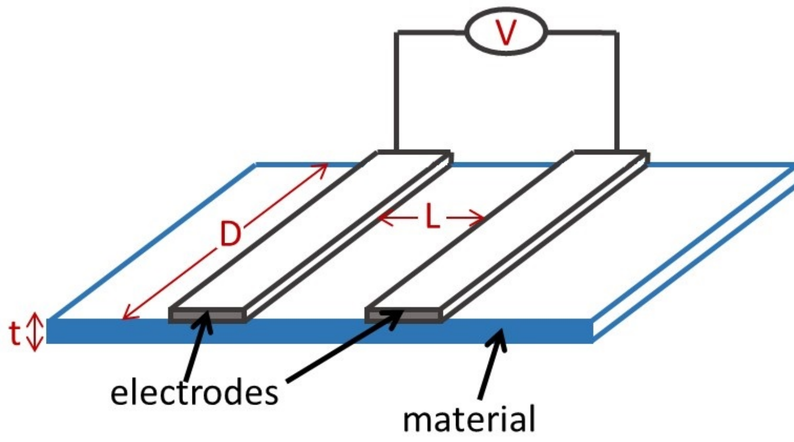

(a)

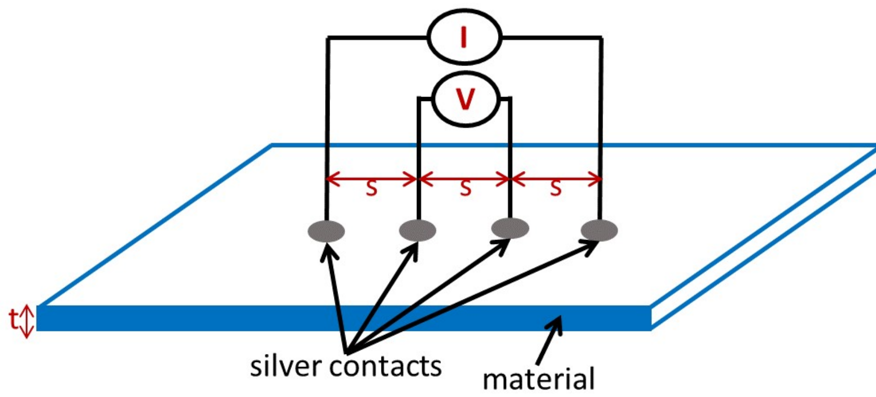

(b)

Figure 3.13: Basic set-up for (a) two-point probe and (b) four-point probe measurements.

Chapter 4

Results

In the present chapter we report the experimental results obtained during this study. Section 4.1 is dedicated to a series of tests conducted in order to attain the calibration of the SPS experimental apparatus described in Sec. 3.2.1. Thereafter, the results of the SPV characterization of the nc-SiO_xN_y:H layers deposited on silicon, and the current-voltage measurements on those deposited on both Si and glass substrates, are presented in Sections 4.2 and 4.3, respectively.

4.1 Optimization of the SPS set-up

Prior to the actual SPS measurements on the samples, several monochromator-sensor configurations have been tested, as well as the effect of different lock-in settings on the acquisitions. The results are reported in the following.

Monochromator-sensor configuration

As seen in Section 3.2.1, in the Czerny-Turner configuration the monochromatic light beam is focused by a focusing mirror before reaching the exit of the monochromator (cfr. Fig. 3.9b). The spectrometer SPEX500M (Fig. 3.9a) allows to direct the light beam, entering the monochromator from the front input slit (1), either to the front exit (F) or to the side one (S), by means of a semi-reflective mirror in the optical system. In the set-up in use, a focusing quartz lens (f = 20 mm) was added to the side exit. Its effect on the output light intensity has been investigated by comparing the signals collected at the two exits of the monochromator.
Let us refer to Figure 4.1, where the distance between the pyroelectric sensor and the exit slits is indicated by D_F and D_S, at the front and at the side of the instrument, respectively. In order to find the distance at which the output light beam is focused at each exit, several acquisitions of the QTH lamp have been performed, each with the sensor at a different distance form the considered opening. The results are reported in Figure 4.2.

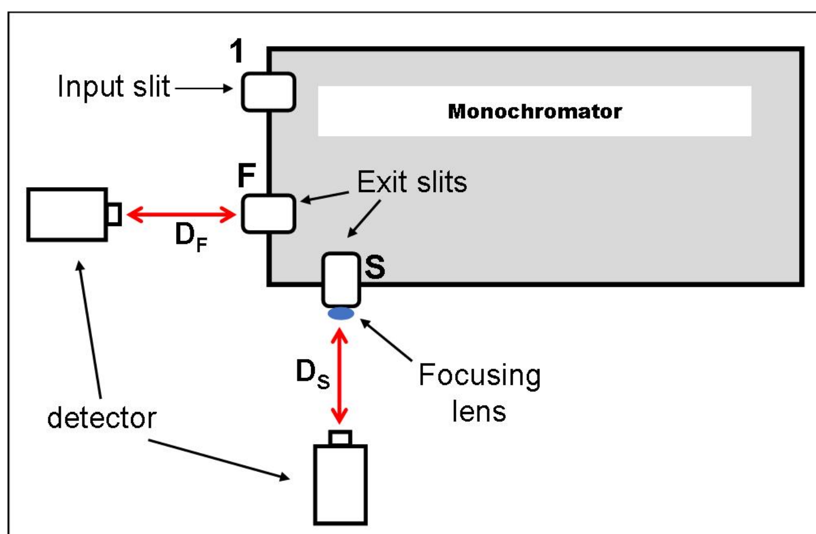

Figure 4.1: Schematic illustration of the monochromator-sensor configurations available in the SPS set-up used (see also Fig. 3.9 for a sketch of the spectrometer and the Czerny-Turner configuration). The front and the side exit slits are indicated by an F and an S, respectively.

At the front exit, where no lens is present, the maximum intensity has been registered with the sensor at $D_F = 18$ mm, using both gratings. On the other hand, when the lens is added, i.e. at the side exit, the distance at which the light beam is focused is different depending on which grating is used: the maximum intensity has been measured at $D_S = 5.0 \pm 0.5$ mm using the grating A and at $D_S = 10.0 \pm 0.5$ mm while using the grating B. Figure 4.3 compares the spectra of the QTH lamp flux collected, using grating B, with the pyroelectric sensor placed at the optimal distance from the two exits: $D_F^{opt} = 18$ mm at the front, and $D_S^{opt} = 10$ mm at the side. As can be seen, there is a difference of one order of magnitude (in mV) between the two signals, which indicates that the further focusing stage, provided by the lens at the side exit, yields a significant enhancement of the output light intensity.
Similar results have been obtained for the photon flux of the Xenon lamp. In this case, however, the output light beam is seen to be focused at a greater distance from the lens, with respect to that recorded using the QTH lamp with the same grating: as an example, the maximum intensity using the grating A has been registered with the pyroelectric sensor at a distance $D_S^{opt} = 10.0 \pm 0.5$ mm from the lens, while $D_S^{opt} = 5.0 \pm 0.5$ mm for the QTH.

It can be concluded that a benefit arises by the use of the focusing lens, which yields a significant enhancement of the output light intensity at the side exit with respect to that collected at the front, where no lens is present. Therefore, in order for the normalization of the SPV signal (equation 3.11) to be consistent, both the light intensity and the SPV spectra must be acquired from the same exit of the monochromator in use.
In addition, it has been possible to evaluate the distance at which the light beam is

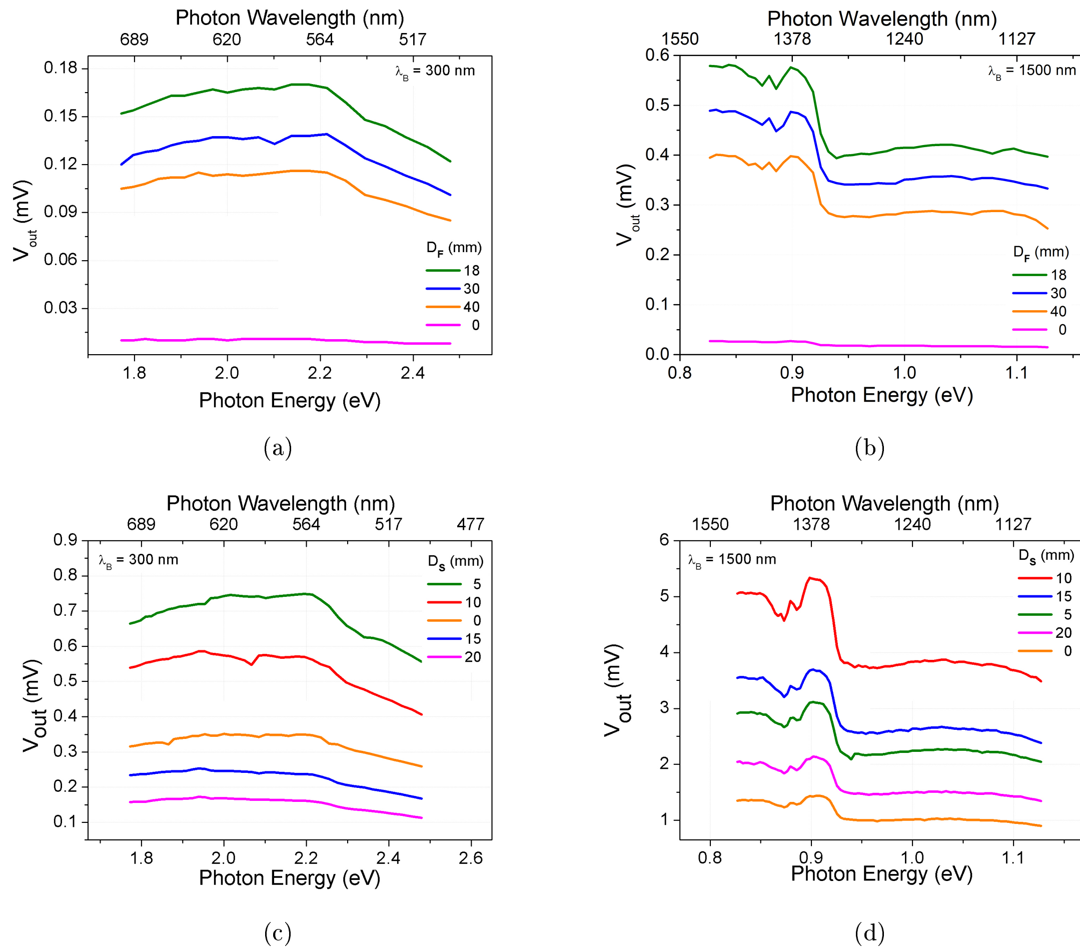

Figure 4.2: QTH lamp photon flux collected by the pyroelectric sensor at different distances d (mm), from the (top) front-no lens and (bottom) side-with lens exit slits of the monochromator, measured in the energy range (a)-(c) [1.8 - 2.4] eV with the grating A (λ_B = 300 nm), and (b)-(d) [0.83 - 1.13] eV with the grating B (λ_B = 1500 nm).

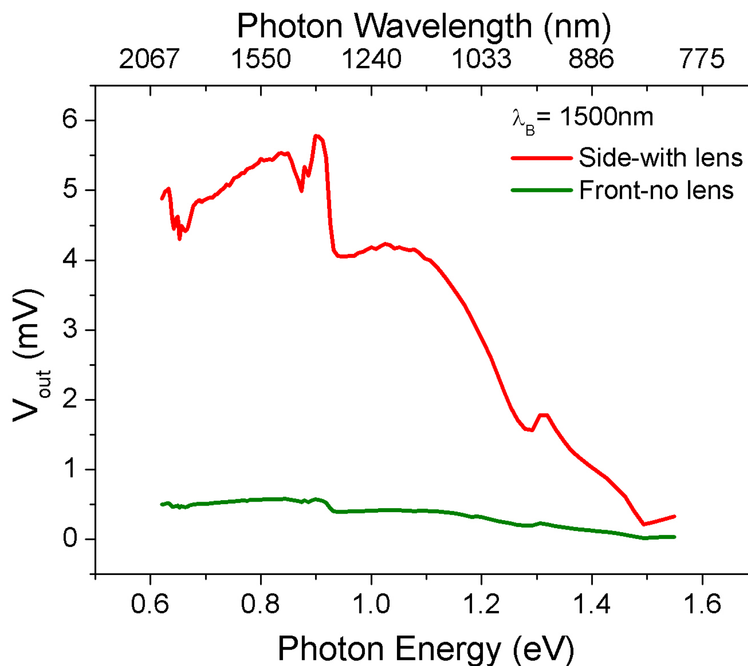

Figure 4.3: Comparison of the photon flux from the QTH lamp, measured using the grating B (λ_B = 1500 nm) with the pyroelectric sensor placed at the optimized distance from the front-no lens (green curve) and the side-with lens (red curve) exit of the monochromator, respectively equal to D_F^{opt} = 18 mm and D_S^{opt} = 10 mm.

focused by the lens, using each grating, corresponding to the optimal distance for the acquisition.

At last, it has been also verified that the output light intensity is greater when the opening is set at its maximum aperture, corresponding to an height of 2 mm and to the entrance/exit slits width equal to 3 mm [59].

Lock-in parameters

As explained in Section 3.2.1, one of the parameters of the lock-in amplifier important for the attenuation of the surrounding noise is the dynamic reserve, defined as the largest tolerable noise at the lock-in input with respect to the full scale signal [59]. The actual value depends on the sensitivity of the measurement, which, in fact, sets the maximum available value if in High Reserve mode, the minimum available value if in Low Noise mode, or an intermediate value if the Normal mode is set on [59]. Figure 4.4 shows three curves corresponding to the pyroelectric signal of the QTH flux, each recorded in a different reserve mode. The signal appears to be equally stable in all three cases, and no marked difference is observed between the curves obtained while in the Normal and High reserve modes, yet a slight attenuation of the output resulted from the Low Noise mode. Therefore, the Normal mode seems to represent a reasonable choice for the measurement of the photon flux with the pyroelectric sensor.

Indeed, the time constant (TC) of the low pass filter is another critical parameter: because an RC filter requires ∼5 TCs to settle its final value, a TC too low may prevent the signal to reach stability, thereby resulting in a noisy output [59]. This effect can be clearly observed in the spectra of Fig. 4.5, where the pyroelectric response measured with TC equal to 1 s and 100 ms is reported in blue and orange, respectively: a lower time constant led to higher noise. On the other hand, the value of the filter roll-off has shown not to be of significant influence (compare Fig. 4.5a and Fig. 4.5b), and thus it has been kept at an intermediate value of 12 dB/oct during all acquisitions.

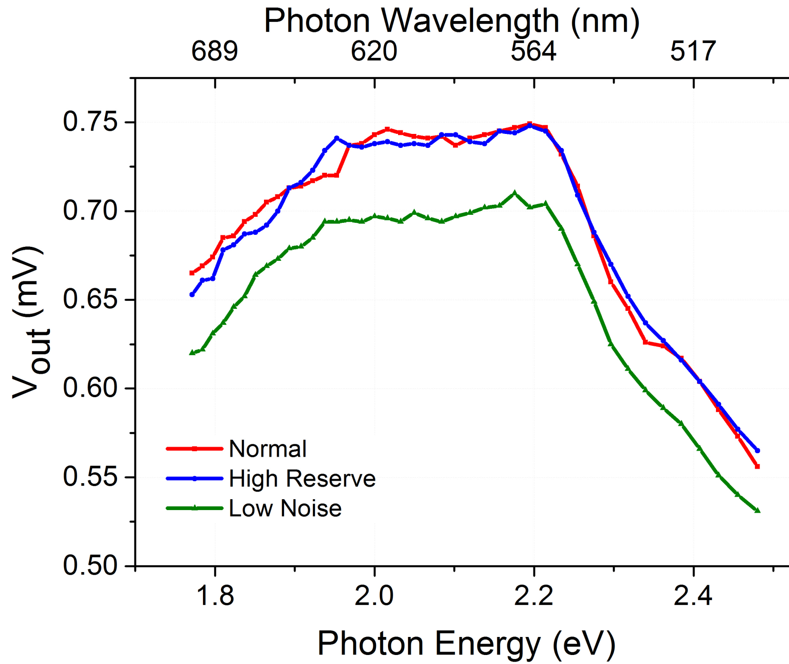

Figure 4.4: Comparison of the QTH lamp photon flux collected by the pyroelectric sensor at the side exit of the monochromator, using the grating A (λ_B = 300 nm), recorded in Low Noise mode (green curve), High Reserve mode (blue curve), and Normal mode (red curve).

Figure 4.6 shows the QTH lamp intensity spectra acquired from the side exit of the monochromator in the optimal configuration: D_S^{opt} = 5 mm when using grating A, D_S^{opt} = 10 mm when using grating B, in Normal reserve mode, TC = 1 s. When using the grating A, the maximum intensity is observed for energies around 2 eV, while with the grating B the signal appears higher in the range 0.8 eV to 1.5 eV.

It must be noted that, since the QTH lamp has maximum emission around 1 eV, there is a significant difference between the magnitude of the measured signals in the two cases: the one acquired using the grating B is almost one order of magnitude greater than that resulting from the use of the grating A. In fact, the spectrum acquired from a certain lamp results from the convolution of the emission spectrum of that particular source

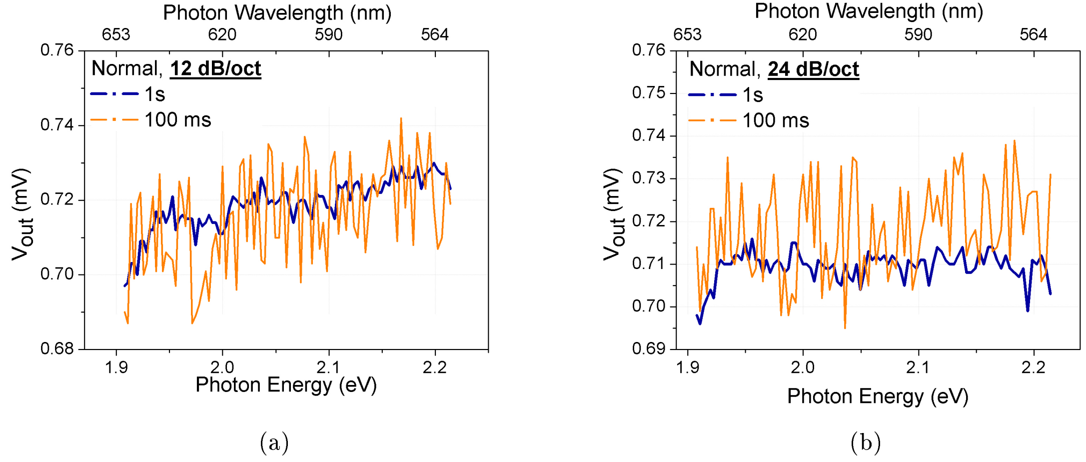

Figure 4.5: Pyroelectric signals of the QTH flux at the side exit (using the grating A) taken in the Normal reserve mode with a time constant of 1 s (blue curve) and 100 ms (orange curve). The slope of the lock-in low pass filter was set at 12 dB/oct and 24 dB/oct.

and the efficiency spectrum of the grating employed. Consequently, in our case we have chosen to use the grating B (λ_B = 1500 nm) when using the QTH lamp, and the grating A (λ_B = 300 nm) when using the Xenon lamp, since the latter has maximum emission around 2 eV (cfr. Sec. 3.2.1).

Due to the results obtained in the preliminary investigation of the set-up, the following parameters have been used for the SPV measurements:

- the grating B (λ_B = 1500 nm) when using the QTH lamp, D_S^{opt} = 10 mm;
- the grating A (λ_B = 300 nm) when using the Xenon lamp, D_S^{opt} = 10 mm;
- fixed height of the exit slit at its maximum of 2 mm;
- Normal reserve mode, intermediate roll-off (12 dB/oct), and time constant TC $\geq$ 1 s.

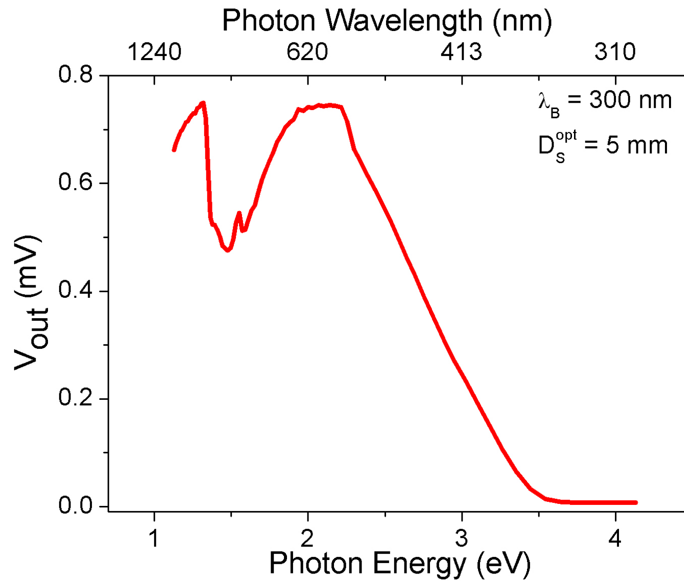

(a)

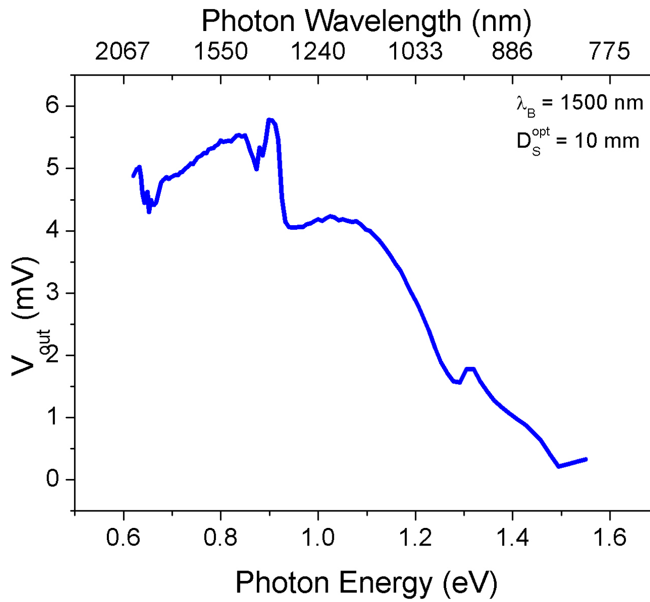

(b)

Figure 4.6: QTH lamp photon flux spectra measured in the optimized configuration of the SPS set-up (D_S^{opt} = 5 mm when using grating A, D_S^{opt} = 10 mm when using grating B, Normal reserve mode on, TC = 1 s), as resulted using (a) the grating A (λ_B = 300 nm), and (b) the grating B (λ_B = 1500 nm).

4.2 SPV Measurements

Surface Photovoltage Spectroscopy was performed on the nc-SiO_xN_y:H samples deposited on silicon listed in Table 3.1. In order to remove the native oxyde layer that typically might form on the top of the surface, all three samples have been dipped in diluted HF just before performing the measurements.

Shimakawa *et al.* [42] have suggested that the optical absorption of nc-Si:H can be dominated by a mean field constructed by a mixture of amorphous and crystalline states, as confirmed by the agreement of the numerical simulations with the experimental data for the absorption coefficient [42, 65]. Moreover, from the results of absorption coefficient measurements on c-Si, a-Si:H and nc-Si:H samples, emerges that the nano-crystalline film shows an intermediate behaviour between that of c-Si and a-Si:H [42, 65]. In particular, the comparison of the absorption coefficient spectra of the samples highlightes that nc-Si:H has higher absorption than crystalline silicon for energies above 1.7 eV [42, 65].
As regards the nc-SiO_xN_y:H samples under study, previous results from absorption measurements have pointed out that the absorption coefficient (α) of these films decreases for wavelength values $\lambda > 600$ nm, and consequently that they appear transparent to photon energies around 1 eV [4, 6].

Therefore, SPV studies in the spectral range around 1 eV were conducted with the purpose to investigate the properties of the interface between the layers and the silicon substrate. Whereas, light radiation at energies around 2 eV (Xe lamp) was employed for the investigation of the electronic structure of the actual SiO_xN_y layer.

4.2.1 SiO_xN_y/Si interface properties

In Figure 4.7, the as-measured spectrum SPV_{Raw} (blue curve) of the sample C0h_Si is compared to the QTH lamp intensity (black curve) measured with the pyroelectric sensor, in the spectral range 0.90 eV to 1.20 eV.
Since the photon flux spectrum shows no significant variations in this energy range, the marked increment of SPV_{Raw} around 1 eV can be attributed to the material response to irradiation. The normalized spectrum SPV_{Norm} (red curve), obtained according to Eq. 3.11, also confirms this hypotesis.
Moreover, it can be observed that the results obtained using the two probes, the ITO-coated glass (Fig. 4.7a) and the copper grid (Fig. 4.7b), are in good agreement.

We report the normalized SPV spectra of all three samples, for energies between 0.90 eV and 1.20 eV, in Figure 4.8: the sample C0h_Si (R_{N_2O}=9%, as-deposited) is indicated in red, the C3h_Si (R_{N_2O}=9%, 3 h annealed) is reported in blue, and the sample E3h_Si (R_{N_2O}=47%, 3 h annealed) is indicated by the green curve.
As explained in Chapter 2 and at the beginning of this section, for photon energies around 1 eV the SPV signal is expected to show an increase up to a saturation value, due to photo-induced band-to-band transitions in the c-Si substrate, followed by a decrease due

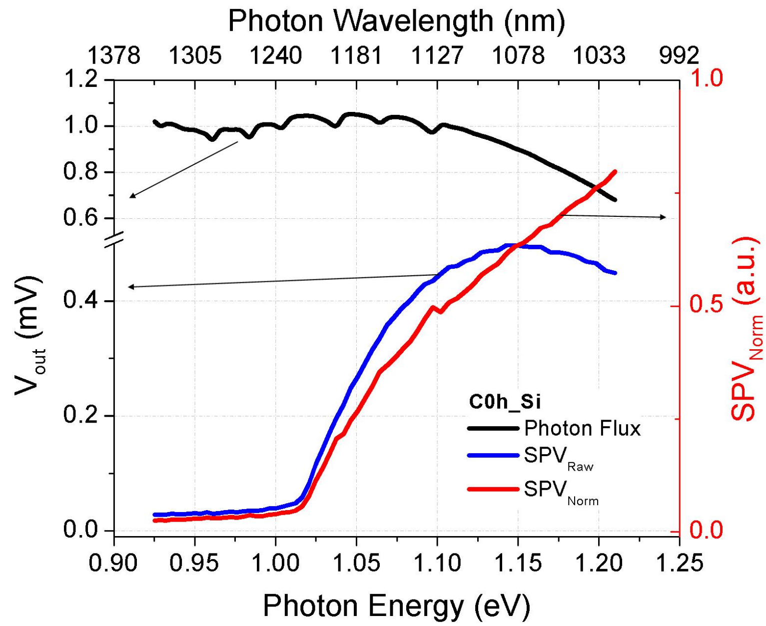

(a)

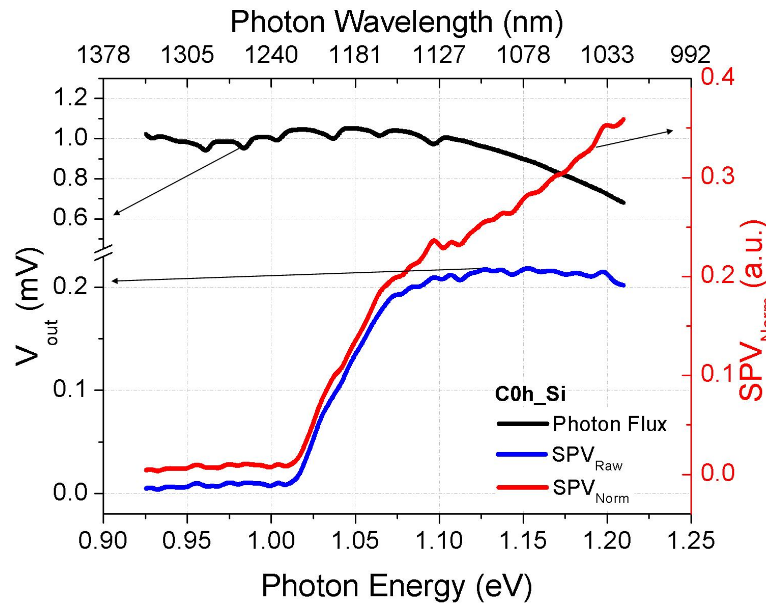

(b)

Figure 4.7: (Blue) as-measured and (red) normalized SPV spectra of the sample C0h_Si (R_{N_2O}=9%, as-deposited) for energies around 1 eV, taken with (a) an ITO-coated glass and (b) a copper grid, as the metallic electrode of the MIS structure. The black curve corresponds to the QHT lamp photon flux measured with the pyroelectric sensor in the same energy range. In the left axis, V_{out} indicates the magnitude (in mV) of both the pyroelectric signal and the SPV_{Raw}.

to electron-hole recombination at the interface.

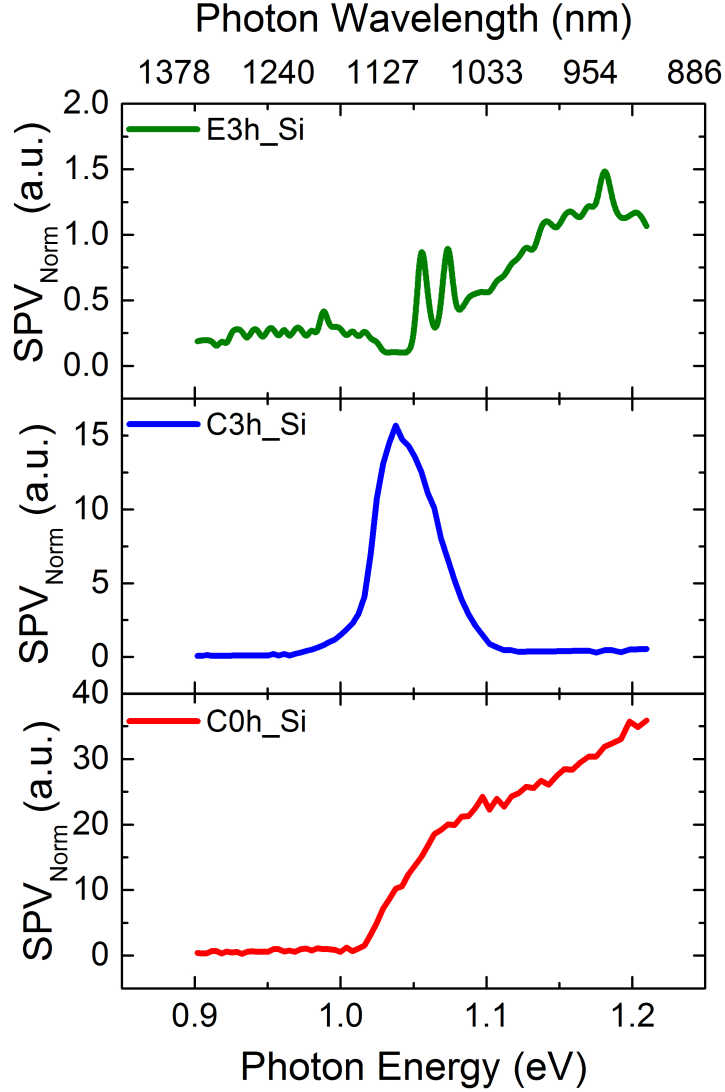

Figure 4.8: SPV normalized spectra in the range 0.90 eV to 1.20 eV for: from top to bottom, the E3h_Si sample (R_{N_2O}=47%, 3 h annealed), the C3h_Si sample (R_{N_2O}=9%, 3 h annealed), and the C0h_Si sample (R_{N_2O}=9%, as-deposited), indicated in green, blue, and red, respectively.

For all three samples, the signal is observed to rise significantly for photon energies near the band gap of c-Si (E_g = 1.12 eV [66]). Nonetheless, we do not observe the decrease due to e-h recombination at the interface in the as-deposited layer (C0h_Si in Tab. 3.1), while this effect can be seen in the spectra of the annealed ones (C3h_Si, E3h_Si). Therefore, as it appears from its spectrum, the as-deposited sample with low oxygen content shows good interface passivation quality.
On the other hand, the loss of the passivating properties for the annealed layers might be explained by taking into account that the thermal treatment induces the relocation

of oxygen within the amorphous network, as evidenced by previous studies [6]. This effect could lead to the formation of oxygen precipitates at the interface, which can act as recombination centres [6].

Furthermore, it should be noticed that the peak position for the sample E3h_Si (R_{N_2O}=47%, 3 h annealed) is slightly shifted towards higher energies and that the whole spectrum appears more noisy. These macroscopic effects, not visible for the C3h and C0h samples, could be attributed to the higher oxygen content of this layer with respect to the other two [6].
In the sample with higher oxygen content the annealing treatment leads to oxygen precipitation [6]. The presence of oxygen precipitates has been observed in FTIR spectra reported by Perani *et al.* [6], where the peak position of the Si-O-Si bond is seen to reach the position corresponding to stoichiometric SiO_2 (1081 cm^{-1}) for R_{N_2O} = 47%.
Hence, the enhancement of the incorporation of oxygen within the SiO_xN_y layer (E3h) might be the reason of the observed shift of the energy gap of the material towards higher values, since SiO_2 has a wider bandgap then c-Si (9.3 eV and 1.12 eV, respectively [49, 66]).

At last, an attempt has been made to measure the SPV signal around 2 eV using the QTH. However, the photon flux of the lamp in this spectral range turned out to be too low to observe SPV effects on these samples.

4.2.2 SiO_xN_y surface properties

Figure 4.9 illustrates the SPV spectra of the C0h_Si sample, both as-measured (blue curve) and normalized (red curve), for energies from 1.7 eV to 2.5 eV. The Xenon lamp photon flux measured with the pyroelectric sensor is indicated in black. As in the case of the QTH lamp, no marked variations can be highlighted in the Xe flux spectrum, and the normalized curve follows the trend of the raw signal. Therefore, it can be assumed that the features in the spectrum are not related to spectral variation of the photon flux, but to photo-induced electronic transitions in the sample.

The normalized SPV spectra collected from the three samples are reported in Figure 4.10, together with the corresponding derivative spectra, calculated according to Eq. 3.12; both the normalized and derivative curves are indicated in red for the C0h, in blue for the C3h, and in green for the E3h sample.

First of all, a general decrease of the SPV signal with increasing energy can be observed for all the samples, which could be explained considering that, as the light penetration depth decreases with increasing E[1], the e-h pairs are generated more and

[1] The characteristic penetration depth l is the inverse of the optical absorption coefficient $\alpha(\lambda)$ (cm^{-1}), which is defined by the expression: $-(d^2\left[\Phi(\lambda,z)\right]/dz^2) = \alpha(\lambda)\ \Phi(\lambda,z)$, where the z-axis points in the direction of the photon flux Φ and λ is the photon wavelength. The solution is given by the Lambert-Beer absorption law:

$$\Phi(\lambda,z) = \Phi_0\ e^{-\alpha(\lambda)z} \tag{4.1}$$

and it describes the attenuation of the incident light intensity (Φ_0 is the initial photon flux density) after

more near the surface, where they subsequently recombine. Hence, since no charge redistribution takes place, the band-bending of the SCR, and so the surface voltage, are left unaltered (SPV = 0) (cfr. Sec. 2.1.2).

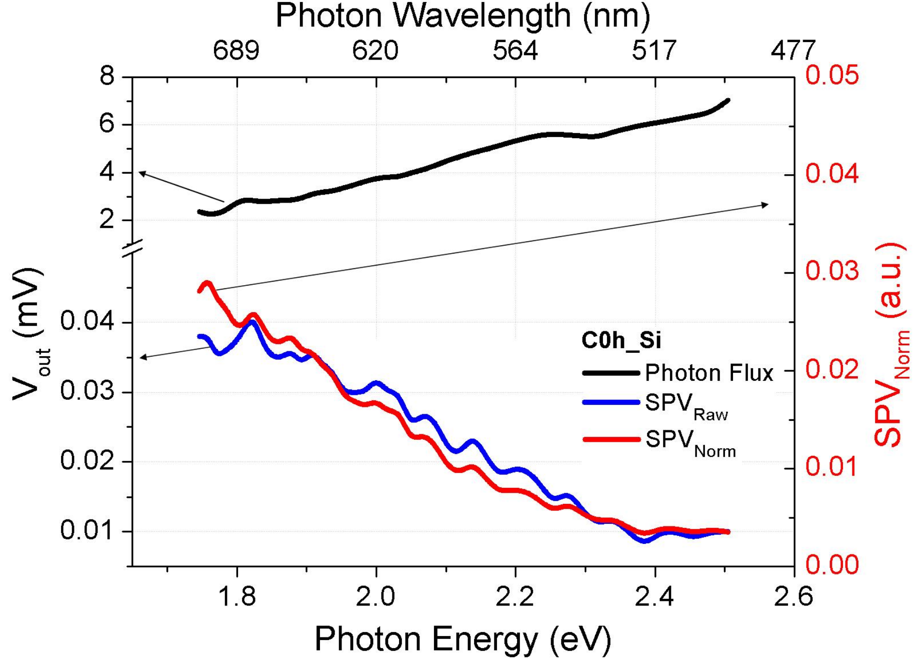

Figure 4.9: (Blue) as-measured and (red) normalized SPV spectra of the sample C0h_Si (R_{N_2O}=9%, as-deposited) in the energy range [1.7 - 2.5] eV. The black curve corresponds to the Xenon lamp photon flux at the same energies, measured with the pyroelectric sensor. In the left axis, V_{out} indicates the magnitude (in mV) of both the pyroelectric signal and the SPV_{Raw}.

In particular, this effect is more pronounced for E3h sample, whose spectrum is characterized by a significant broadening of the decreasing curve. This might be explained by considering that SPV spectroscopy is sensitive to electronic transitions between localized tail states, or Urbach tails, that might be present at the edges of the conduction and valence bands of an amorphous material [29]. Moreover, it should be reminded that the breadth of the tail states is an indication of the amount of disorder present within the material [42, 29].

Therefore, the effect observed for E3h sample might be due to a wider Urbach tail, which denotes an enhanced degree of disorder of this layer with respect to the other two. This seems in agreement with what has been reported previously as regards the evolution of the structure of the studied nc-SiO_xN_y films: the results of Perani *et al.* [6] show that the incorporation of more oxygen within the amorphous network, followed by the annealing, leads to higher disorder and lower crystalline fraction in the layer

travelling a distance z in the material. Thus, the penetration depth l corresponds to the distance into the solid at which the light intensity is attenuated by a factor 1/e [43, 67, 68].

E3h_Si (R_{N_2O}=47%, 3 h annealed) with respect to the samples deposited with lower N_2O dilution, both as-deposited (C0h) and annealed for 3 hours (C3h).

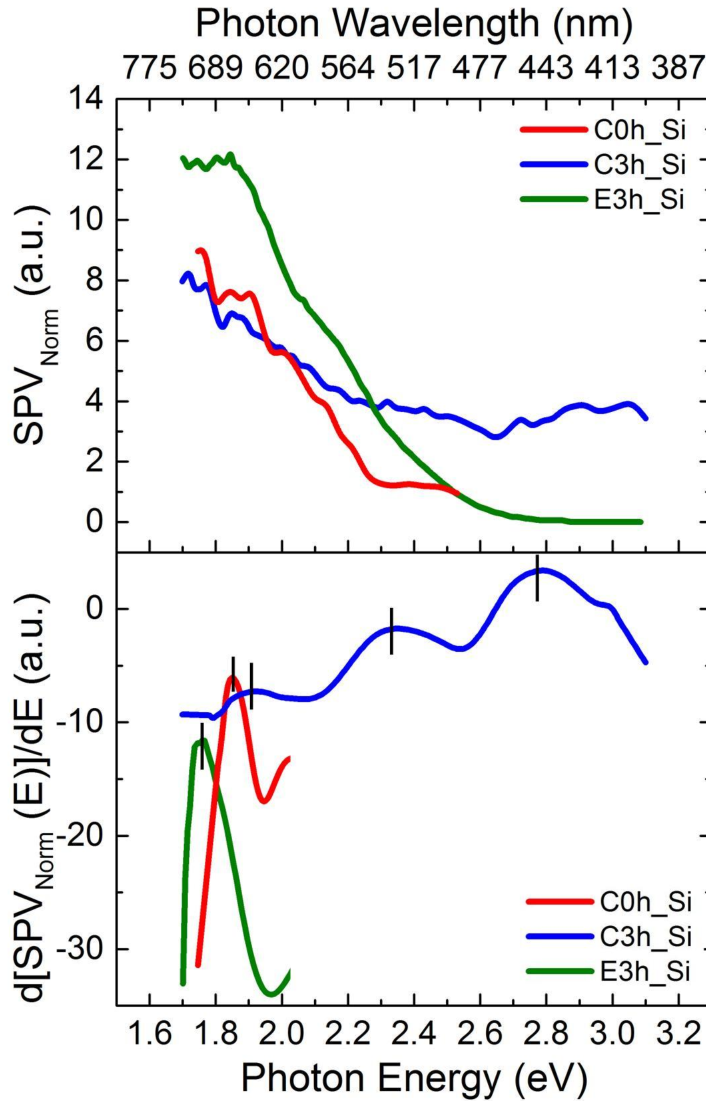

Figure 4.10: (Top) normalized SPV and (bottom) corresponding derivative spectra, obtained using the Xenon lamp, for the three samples: C0h_Si (R_{N_2O}=9%, as-deposited) depicted in red, (blue) C2h_Si (R_{N_2O}=9%, 3 h annealed) indicated in blue, and E3h_Si (R_{N_2O}=47%, 3 h annealed) reported in green.

As the main features of the SPV spectra are the slope changes, these can be better shown in a plot of the derivative of the SPV spectrum as a function of energy (cfr. Section 3.2.1). This derivative is reported for the three samples in Figure 4.10.
A maximum can be clearly distinguished in the derivative spectra of the three samples, which might indicate the energy position of the bandgaps of the material. The values of the band-to-band transitions are reported in Table 4.1. The error associated to the energy values has been estimated by taking into account the width of the observed peaks

and the error of the wavelength of the light beam at the exit of the monochromator, calculated from Eq. 3.10.

Table 4.1: Band gap energy values extracted from the derivative spectra of the SPV (Figure 4.10) obtained for the investigated nc-SiO_xN_y:H layers.

Sample	E_g (eV)
C0h_Si	1.85 ± 0.05
C3h_Si	1.90 ± 0.05
E3h_Si	1.75 ± 0.05

As it appears, the samples C3h and C0h show a similar value (higher for the C3h), while, for the E3h, E_g corresponds to a lower energy. As stated above, the different behaviour of the E3h with respect to the other two, could be related to the higher oxygen content of this sample, which results in higher structural disorder within the layer [6, 8].
Moreover, it is worth to note that the resulting bandgaps seem to confirm the trend of the Tauc gaps extracted from absorption measurements (see Table 3.1), although it is not possible to compare the exact values, since they have been extrapolated from different methods [6].

Further examination of the derivative spectrum of C3h layer (blue curve in Fig. 4.10) shows for this sample a higher signal with respect to the other two, and reveals the presence of additional features at energies higher than the bandgap. The energy values corresponding to the local maxima at $E > 1.9$ eV in the derivative spectrum of C3h are reported in Table 4.2.

Table 4.2: Transition energies extracted from the derivative spectrum of sample C3h_Si reported in Figure 4.10.

Level	Transition Energy (eV)
E_1	2.33 ± 0.05
E_2	2.78 ± 0.05

This finding might be an indication of quantum confinement effects occurring at the Si nanocrystals (NCs), which are formed within the amorphous matrix due to the annealing treatment, as reported in reference [6]. It might also indicate a higher limit for the dimensions of the NCs at 5 nm, since the latter is the critical dimension above which QC effects are no more observed [69].
Previous studies have shown that oxygen incorporation within the layer prevails on nitrogen incorporation during the deposition by PECVD [4, 6]. Therefore, for C3h (R_{N_2O}=9%, 3 h annealed) it can be assumed that the Si NCs are embedded in an amorphous matrix mainly composed by SiO_x-like compounds.
Evidences of quantum confinement effects might also establish a higher limit for the dimensions of the Si crystals in the C3h layer, provided by the Bohr radius of silicon

excitons, which is $\sim$ 5 nm [69, 70].
As a consequence of quantum confinement of the carriers, discrete energy levels arise at the edges of the valence and conduction bands of the semiconductor; therefore, the band gap of the nanocrystal, or quantum dot (QD), results from the sum of the fundamental bulk band gap E_g^0 (here $E_g^0 = E_g(Si)$) and the confinement energy of both electrons and holes [69]. QDs absorption spectra typically consist of a series of discrete peaks at energies higher than the bandgap, corresponding to optical transitions between different electron and hole levels (indicated by $S_{e/h}$ for orbital angular momentum l=0, $P_{e/h}$ for l=1, $D_{e/h}$ for l=2, and so forth) [69].
In Fig. 4.11 is reported a schematic depiction of the band structure of Si QDs in a SiO_x matrix, as deduced for the behaviour of C3h sample from the derivative of the SPV spectrum (4.10). Blue arrows indicate the electronic transitions between discrete electron and hole levels corresponding to the energy values listed in Table 4.2.

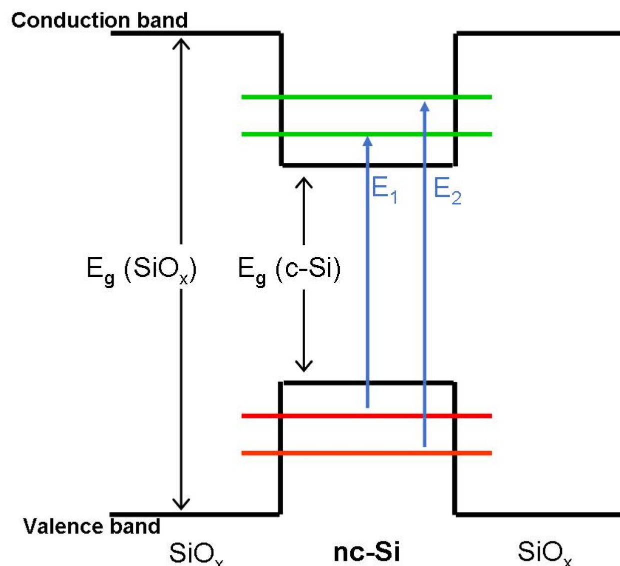

Figure 4.11: Schematic illustration of the electronic structure of a nc-Si QD embedded in a SiO_x matrix. The descrete electron and hole levels in the Si QD are indicated in green and red, respectively. The blue arrows indicate the electronic transitions corresponding to the energy values, E_1 and E_2, reported in Tab. 4.2.

The transition energies extracted from the derivative spectrum of C3h sample (Tab. 4.2) appear to be in agreement with the results from single-dot spectroscopy studies on silicon quantum dots in an amorphous oxyde matrix, reported by Sychugov *et al.* [71]. They observed four broad peaks at energies of 2.29 eV, 2.67 eV, 2.94 eV, and 3.33 eV, in the absorption curve of the Si QDs. The first peak at $\sim$2.3 eV has been identified as a combination of $S_h \rightarrow D_e$ and $P_h \rightarrow P_e$, while, the next peak at $\sim$2.65 eV has been attributed to arise from the $P_h \rightarrow D_e$ family of transitions [71]. The higher-energy peaks have been attributed to several transitions from numerous, densely spaced electron and

hole levels [71].

At last, several SPV spectra were acquired for each sample: as a general rule, the position of the peaks is seen to remain constant. As an example, four different acquisitions, normalized SPV and corresponding derivative, in the energy range around 2 eV, are reported in Fig. 4.12 for the E3h_Si sample.

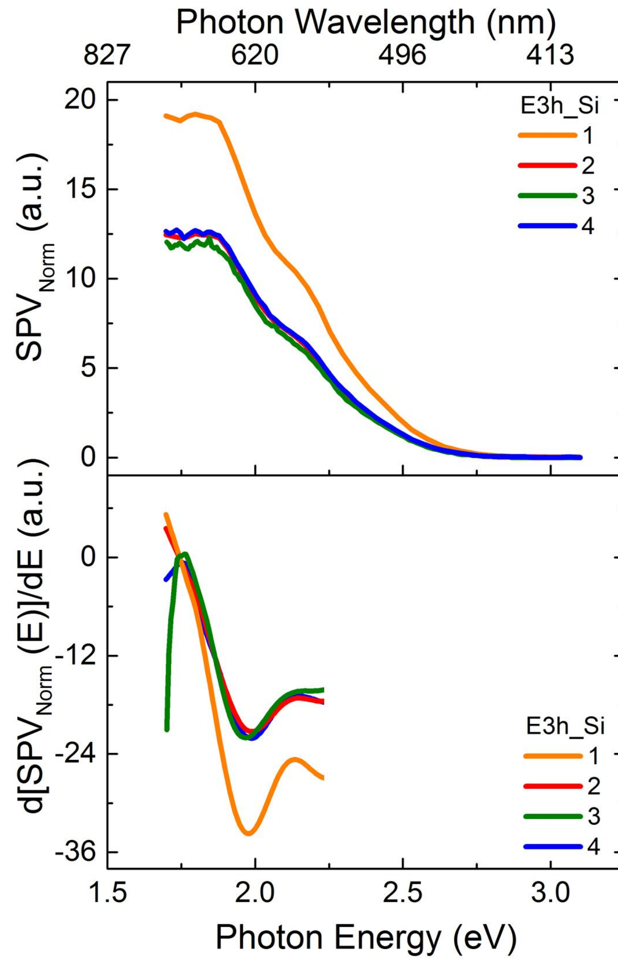

Figure 4.12: (Top) normalized SPV and (bottom) corresponding derivative spectra, from four different acquisitions in the range [1.7 eV - 2.5 eV], on the E3h_Si sample (R_{N_2O}=47%, 3 h annealed).

4.3 Electrical Measurements

The two-point probe I-V characteristics of the annealed samples deposited on glass, C3h_glass and E3h_glass in Table 3.1, are reported in Figure 4.13.
First of all, from the linear relationship between the output current and the input voltage, we can conclude that the contacts are of ohmic type. In addition, the response of both samples at positive and negative biases appears almost symmetric.
The sample with lower oxygen content, $R_{N_2O} = 9$ %, shows higher conductivity than the sample with $R_{N_2O} = 47$ %. In fact, for the C3h_glass, higher output currents correspond to lower input voltage values, whereas the E3h_glass shows almost zero conductance in a wider range of input voltages, [-1.5, 1.5] V. Moreover, there is a difference of 3-4 orders of magnitude between the measured output current values, mA and μA for C3h and E3h, respectively.

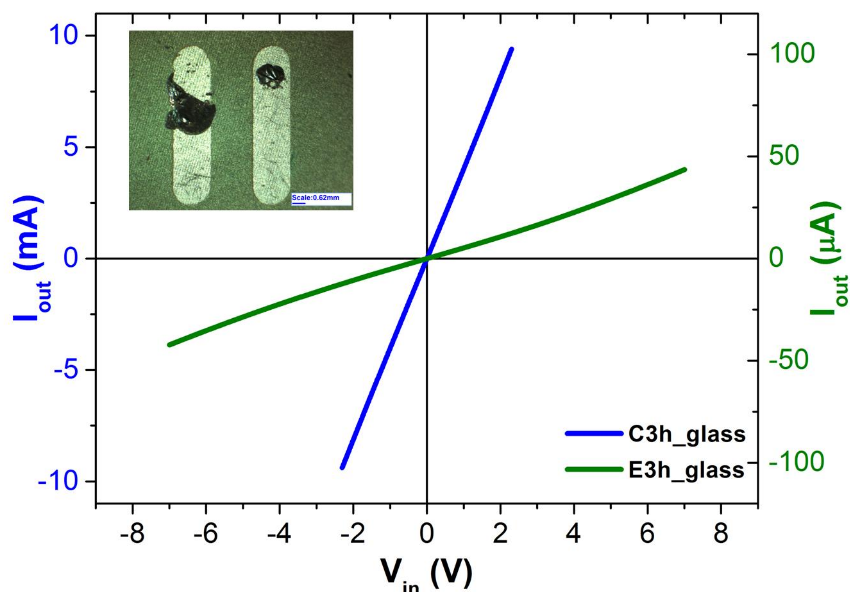

Figure 4.13: Current voltage characteristics of the samples C3h_glass (blue) and E3h_glass (green). The I_{out} axis has been scaled differently for the two samples for sake of clarity. The inset shows a picture (0.8x of magnification) of the metallic contacts on the C3h_glass sample.

The observed electric behaviour might be attributed to the different crystalline content of the two investigated layers.
The crystalline fraction (χ) obtained from Raman spectroscopy resulted in an higher value ($\chi = 88\%$) for the sample with low oxygen content (C3h_glass) with respect to the value ($\chi = 70\%$) of the sample deposited with higher N_2O dilution (E3h_glass) [6].

From c-AFM morphology and current maps emerges that the crystalline phase has a strong role in conductivity enhancement, thanks to the presence of highly conductive clusters of Si nanocrystals, which are formed during the annealing [6]. On the other hand, an increase of N_2O dilution causes an enhancement of the disorder, which corresponds to larger crystal clusters, but also to lower crystalline fraction [6].
The resulting values of the dark conductivity (cfr. Sec. 3.2.2) are:

$$\sigma_{dark} = 49 \pm 1 \quad (S/cm) \tag{4.2}$$

$$\sigma_{dark} = (5.4 \pm 0.1)\ 10^{-2} \quad (S/cm) \tag{4.3}$$

for the C3h_glass and the E3h_glass, respectively, and appear to be consistent to the previous results on these samples reported by Perani *et al.* [6] (see also Table 3.1). We report a comparison of all measurements in Figure 4.14.
On the other hand, values of resistivity very close to that of the silicon substrate employed (2 Ω cm [4]) suggest that in the four-point probe configuration the electrical conduction took place mostly in the substrate, which is less resistive.

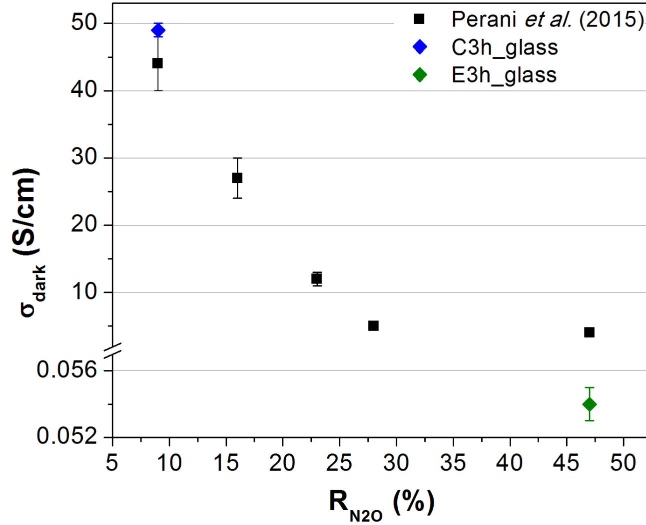

Figure 4.14: Room temperature dark conductivity as a function of N_2O dilution after 3 h annealing, from [6] (black symbols) and from the presented measurements (blue for C3h_glass, green for E3h_glass).

For 2PP measurements on the samples deposited on silicon the contacts were made with high conductive silver paste. The resulting curves in Figure 4.15 show that these contacts act as double Schottky barriers.
Nonetheless, the differences between the three curves suggest that an effect related to the properties of the nc-SiO_xN_y layers may be present. In particular, the as-deposited layer,

C0h_Si, appears to be the less conductive, while the same sample annealed for three hours shows a higher slope. The annealed sample with higher N_2O dilution, E3h_Si, shows an intermediate behaviour with respect to the other two.
In conclusion, the conductance is seen to increase after the thermal treatment and with decreasing oxygen content, in agreement with the previous results on the conductance at the nanoscale obtained by Fazio et al. [9] (cfr. Figure 3.6 in Section 3.1).

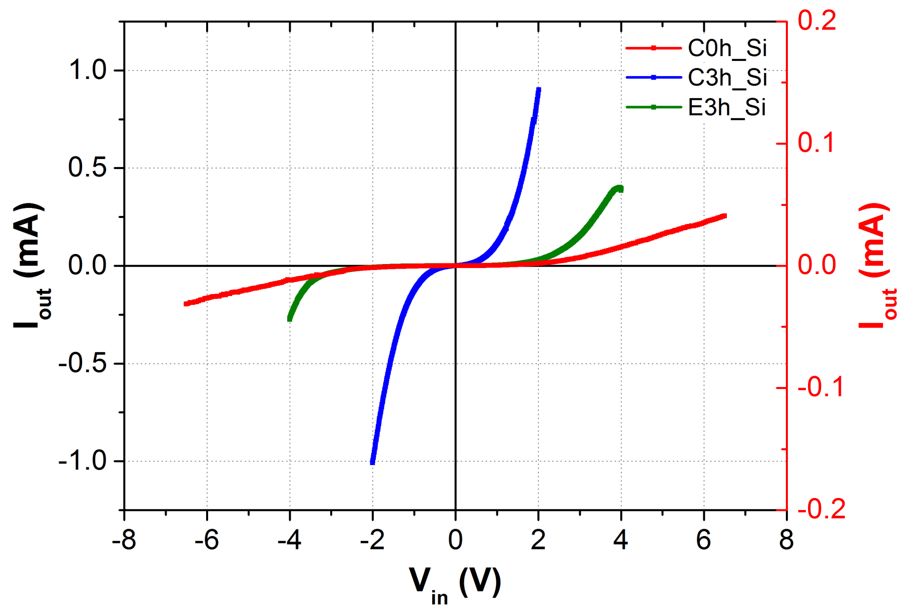

Figure 4.15: Comparison between 2PP-measured IV characteristics for C0h_Si (red), C3h_Si (blue), and E3h_Si (green). The I_{out} axis on the left has been scaled differently for the C0h_Si sample.

Conclusions

In the last years, silicon heterojunction (SHJ) solar cells have demonstrated the most promising results among the field of thin film photovoltaics, reaching record efficiencies for silicon-based devices of about 25% [1]. The key to these high performance devices relies on the concept of passivated heteroemitters: an intrinsic layer and a doped layer of hydrogenated amorphous silicon are subsequently deposited on both the front and the rear side of the crystalline silicon thin film absorber. Such heteroemitter stack serves the role of a semi-permeable membrane for carrier extraction, enabling the device to reach values of V_{oc} up to 743 mV [2, 3].
Notwithstanding the excellent passivating properties of a-Si:H, currently employed to form the heteroemitter stack in SHJ devices, this material also shows strong parasitic absorption of light, which causes a loss in short circuit current, consequently limiting the achievement of higher power conversion efficiencies.
This effect can be prevented by the use of a wider bandgap material. In these regards, silicon oxynitride is believed to represent a good candidate for the substitution of a-Si in SHJ solar cells: its amorphous form have already demonstrated implied open circuit voltages as high as 733 mV [4].
Previous studies on hydrogenated nanocrystalline silicon oxynitride (nc-SiO_xN_y:H) thin layers deposited on crystalline silicon substrate by Plasma-Enhanced Chemical Vapour Deposition (PECVD) suggest that the use of nanocrystalline films, instead of amorphous ones, could lead to significant efficiency improvements. These films have shown optical bandgap values as high as 2.5 eV and very high dark conductivities, up to 44 S/cm [6].

The present work focuses on the investigation on how the oxygen content and the annealing treatment affect the optoelectronic properties and the macroscopic electric behaviour of hydrogenated nc-SiO_xN_y thin layers. Three different samples deposited by PECVD on c-Si and glass substrate have been studied: a sample deposited with low N_2O dilution in the deposition chamber, resulting in low oxygen content within the layer, not annealed (C0h); a sample with low oxygen concentration, annealed for 3 hours (C3h); a sample with deposited with higher N_2O dilution, 3 hour annealed (E3h).
The investigation was conducted by means of Surface Photovoltage Spectroscopy (SPS) and current-voltage methods. SPV measurements on the samples deposited on c-Si have allowed for the extraction of the bandgap energy of the studied materials, as well as for

the investigation of the surface properties. The results are summarized in the following.

The SPS set-up in use consisted in a white light source (QTH or Xenon lamp) in combination with a spectrometer with two exit slits; a focusing lens was added to one of them. A lock-in amplifier was used to acquire the voltage signal from both a pyroelectric sensor, used for the measurements of the light intensity spectra, and the SPV probe (ITO-coated glass or metallic grid) of the Metal-Insulator-Semiconductor structure (the insulator being the air). The reference signal for the lock-in was provided by a chopper, placed just before the input slit of the monochromator.
Prior to the actual SPV measurements, the calibration of the SPS experimental set-up has been conducted, in order to establish the optimal conditions for the acquisition of the light source intensity spectra, performed with a pyroelectric sensor.
The results have shown that:

- the use of a focusing lens at the exit of the monochromator yields an enhancement of the intensity of the light beam collected by the pyroelectric sensor;
- a maximum of the intensity of the output photon flux can be achieved by adjusting the distance between the detector and the monochromator;
- as regards the parameters of the lock-in amplifier, a minimum time constant of 1 s should be used in order for the pyroelectric signal to be stable, whereas intermediate values of reserve (Normal mode) and roll-off of the low pass filter (12dB/oct) appeared to be sufficient for the acquisition of the lamps flux.

The most significant features in SPV spectra are due to band-to-band transitions, induced by excitation of the charge carriers due to absorption of photons with energy equal or higher than the bandgap of the investigated material [29]. When the interface between two semiconductors is investigated, the SPV is expected to rise in correspondance of the bandgap energy of the substrate. A good quality interface is denoted by a SPV signal that remains constant at high values for energies above the bandgap energy. On the contrary, the decrease of the SPV is due to recombination of carries at the interface, due to the presence of recombination-active interface defect states.
Hence, Surface Photovoltage Spectroscopy has demostrated to represent a valuable tool for the investigation of the passivation quality of the interface between the nc-SiO_xN_y layer and the substrate. The results can be summarized as it follows.

- The SPV spectra of the sample with low oxygen content (as-deposited (C0h)) has shown excellent passivation quality of the SiO_xN_y/Si interface, since the signal does not decrease at higher energies due to carriers recombination. On the other hand, the spectra of the annealed samples, C3h and E3h, show lower passivation quality, recombination mechanisms might occur at the interface between the layer and

the substrate. This behaviour could be attributed to annealing-induced formation of oxygen precipitates, as evidenced by previous results from FTIR spectroscopy measurements [6], which causes an enhancement of the interface defects acting as recombination centres. The formation of O precipitates could be also the reason for the slight blue shift of the bandgap observed for the sample with higher oxygen concentration, towards SiO_2 bandgap values (9 eV [49]).

- The bandgap energy (reported in Table 4.1 for the three samples) appears to lie around (1.8 $\pm$ 0.05) eV for the amorphous layers (C0h, E3h), whereas the sample with higher crystalline fraction (C3h) shows the highest value of E_g, equal to (1.9 eV $\pm$ 0.05) eV; in agreement with the trend observed for the E_{Tauc} values extracted from trasmission spectroscopy in precedent studies on the same samples [7]. This increase can be related to electronic transitions at quantum confined states linked to Si nanocrystals embedded in the SiON matrix [7].

- From the derivative spectra of C3h sample, it has been possible to distinguish additional features at energies above the bandgap (cfr. Tab. 4.2), which are not observed in the spectra of the other samples. These features are associated to some additional transitions (apart from the band to band ones) available for the carriers. The presence of these characteristics might suggest possible effects of quantum confinement (QC) at the silicon nanocrystals. In fact, previous studies had revealed that a phase separation is enhanced during the annealing process, leading to the formation of a multi-phase material, where Si-rich clusters are embedded within an O-rich amorphous matrix [6, 8].

- The energy gap of the sample E3h (annealed and with high O content) results to be lower than C3h (which has a lower O content), as shown in Table 4.1. The reason for this can be due to the high O-related crystal disorder already observed in this sample [6], that induced the formation of high Urbach tails thereby reducing the observed gap value.

At last, current-voltage measurements have shown that the thermal treatment and the oxygen content deeply affect the electrical properties of nc-SiO_xN_y thin films. The results have shown that the annealing treatment promotes an enhancement of the conductivity of the material, whereas the incorporation of high amounts of oxygen within the network results in poorer electrical properties. In fact:

- the sample with low oxygen content, as-deposited, appears the most resistive among the three layers;

- on the other hand, very high values of dark conductivity up to 49 S/cm have been calculated for the sample with low oxygen content, 3 h annealed;

- the sample with higher oxygen content, annealed for 3 hours, shows an intermediate behaviour between the other two samples.

This trend appears to be in good agreement with previous results obtained from both macroscopic conductivity measurements and analysis of the conductance at the nano-scale [6, 8].

In conclusion, SPV measurements have revealed the excellent passivation quality of the as-deposited sample with low oxygen content. In addition, it allowed for the identification of possible quantum confinement effects at the silicon nanocrystals in the sample with low oxygen, 3 h annealed. Furthermore, the thermal treatment have demonstrated to yield a significant improvement of the electrical properties of nc-SiO_xN_y thin films. The results here presented show that the optimization of this layer for its application in SHJ solar cells still requires further study. In order to achieve the required high conductivity, annealing treatments are required; however, such treatments strongly degrades the passivating quality of the layer. Similar high conductivities can be achieved using higher H_2 dilution during the deposition stage, that boosts the layer crystallinity [10].

Ringraziamenti

Desidero ringraziare la Professoressa Daniela Cavalcoli, per avermi seguita in questo percorso sempre con pazienza ed estrema gentilezza. Ringrazio, inoltre, la Photovoltaic Division del Department of Physics dell'University of Konstanz, per la deposizione dei campioni oggetto di questo studio.
Un sentito grazie alla Dottoressa Maria Antonietta Fazio, per la sua disponibilità e gentilezza, e per avermi dato supporto fino alla fine.
Mi sento di ringraziare tutti quanti del settore di Fisica della Materia mi hanno aiutato con gli apparati di misura e mi hanno dato assistenza sempre con cortesia.
Ringrazio i miei famigliari che sono sempre stati presenti in tutti questi anni e a tutti gli amici e le amiche che, nonostante me, mi hanno sempre sostenuta e capita.
Grazie a Fabio, che mi fa sentire come una sorella.
Infine, a mia madre, mia sorella e mio fratello: GRAZIE.

Bibliography

[1] https://www.nrel.gov/workingwithus/re-photovoltaics.html.

[2] S. De Wolf, A. Descoeudres, Z.C. Holman, and C. Ballif. High-efficicency Silicon Heterojunction Solar Cells: A Review. *Green*, 2:7–24, (2012).

[3] T. Mishima *et al.* Development status of high-efficiency HIT solar cells. *Sol. Energy mater Sol. Cells*, (2010). doi:10.1016/j.solmat.2010.04.030.

[4] N. Brinkmann, D. Sommer, G. Micard, G. Hahn, and B. Terheiden. Electrical, optical and structural investigation of plasma-enhanced chemical-vapor-deposited amorphous silicon oxynitride films for solar cell applications. *Sol. Energy Mater. Solar Cells*, 108:180–188, 2013.

[5] Jenny Nelson. *The Physics of Solar Cells*. Imperial College Press, 2009.

[6] M. Perani, N. Brinkmann, A. Hammund, D. Cavalcoli, and B. Terheiden. Nanocrystal formation in silicon oxy-nitride films for photovoltaic applications: optical and electrical properties. *J. Phys. Chem. C*, 119:13907–13914, 2015.

[7] M. Perani *et al.* Annealing effects on SiO_xN_y thin films: Optical and morphological properties. *Thin Solid Films*, 2016. http://dx.doi.org/10.1016/j.tsf.2016.03.067.

[8] Maria Antonietta Fazio. *Nano-scale morphological and electrical characterization of nc-SiO_xN_y thin layers for photovoltaic applications*. Master's degree thesis, Universitá di Bologna - Scuola di Scienze, Corso di Laurea Magistrale in Fisica, 2014/2015.

[9] M. A. Fazio, M. Perani, N. Brinkmann, B. Terheiden, and D. Cavalcoli. Transport properties of Si based nanocrystalline films investigated by c-AFM. *Journal of Alloys and Compounds*, 2017, Submitted.

[10] A.M. Funde *et al.* Influence of hydrogen dilution on structural, electrical and optical properties of hydrogenated nanocrystalline silicon (nc-Si:H) thin films prepared by plasma enhanced chemical vapour deposition (PE-CVD). *Solar Energy Materials & Solar Cells*, 92:1217–1223, (2008).

[11] IPCC, 2014: Climate Change 2014: Synthesis Report. Contribution of Working Groups I, II and III to the Fifth Assessment Report of the Intergovernmental Panel on Climate Change [Core Writing Team, R.K. Pachauri and L.A. Meyer (eds.)]. IPCC, Geneva, Switzerland, 151 pp.

[12] W. Steffen, P. J. Crutzen, and J. R. McNeill. The Anthropocene: Are Humans Now Overwhelming the Great Forces of Nature? *Ambio*, 36(8), December 2017. Royal Swedish Academy of Sciences 2007, `http://www.ambio.kva.se`.

[13] Antonio Luque and Steven Hegedus. *Handbook of Photovoltaic Science and Engineering*. John Wiley and Sons, Ltd., 2nd edition, 2011.

[14] Nathan S. Lewis. Powering the Planet. *MRS Bulletin*, 32, October 2007.

[15] `http://www.solarimpulse.com/`.

[16] ©Fraunhofer ISE: Photovoltaics Report, updated: 17 November 2016.

[17] Wilfried G.J.H.M. van Sark, Lars Korte, and Francesco Roca (Eds.). *Physics and Technology of Amorphous-Crystalline Heterostructure Silicon Solar Cells*. Springer-Verlag Berlin Heidelberg, 2012.

[18] A. Lin, K. Chen, P. Zhang, J. Xu, H. Yang, and X. Huang. Improved efficiency in phosphorous doped n-a-SiNxOy/p-Si heterojunction light emitting diode. *Appl. Phys. Lett.*, 110:081109, (2017).

[19] F. J. Aparicio *et al.* Silicon oxynitride waveguides as evanescent-field-based fluorescent biosensors. *J. Phys. D: Appl. Phys.*, 47:405401, (2014).

[20] J. Schmitz, B. Rangarajan, and A.Y. Kovalgin. Fabrication and properties of GeSi and SiON layers for above-IC integrated optics. *Solid-State Electronics*, 108:8–12, (2015).

[21] H. Yang, E. Wang, H. Wang, and W. Guo. Industrial technology of passivated emitter and rear cells with silicon oxynitride and silicon nitride as rear passivation for high efficiency BIPV modules. *Energy Procedia*, 88:389–393, (2016).

[22] `http://www.nationalgeographic.com/environment/global-warming/global-warming-overview/`.

[23] `https://blogs.scientificamerican.com/plugged-in/why-we-know-about-the-greenhouse-gas-effect/`.

[24] United Nations, Department of Economic and Social Affairs, Population Division (2015). World Population Prospects: The 2015 Revision, World Population 2015 Wallchart. ST/ESA/SER.A/378.

[25] http://unfccc.int/paris_agreement/items/9485.php.

[26] http://re.jrc.ec.europa.eu/pvgis/.

[27] Gavin Conibeer and Arthur Willoughby. *Solar Cell Materials. Developing Technologies.* John Wiley and Sons, Ltd., 2014.

[28] Martin A. Green. *Third Generation Photovoltaics. Advanced Solar Energy Conversion.* Springer, 2003.

[29] L. Kronik and Y. Shapira. Surface photovoltage phenomena: theory, experiment, and application. *Surf. Sci. Rep.*, 37:1–206, 1999.

[30] L. Kronik and Y. Shapira. Surface photovoltage spectroscopy of semiconductor structures: at the crossroads of physics, chemistry and electrical engineering. *Surf. Interface Anal.*, 31:954–965, 2001.

[31] D. Cavalcoli and A. Cavallini. Surface photovoltage spectroscopy: methods and applications. *Phys. Status Solidi C*, 7(5):1293–1300, 2010.

[32] W.H. Brattain and J. Bardeen. Surface properties of Germanium. *Bell System Tech. J.*, 32:1–41, 1953.

[33] E.O. Johnson. Measurement of minority carrier lifetimes with the surface photovoltage. *J. Appl. Phys.*, 28(11):1349–1353, 1957.

[34] A.M. Goodman. A method for the measurement of short minority carrier diffusion lengths in semiconductors. *J. Appl. Phys.*, 32(12):2550–2552, 1961.

[35] H.C. Gatos and J. Lagowsky. Surface photovoltage spectroscopy - a new approach to the study of high-gap semiconductor surfaces. *J. Vac. Sci. Technol.*, 10(1):130–135, 1993.

[36] H.C. Gatos and J. Lagowsky. The structure and properties of metal-semiconductor interfaces. *Surf. Sci. Rep.*, 2:123, 1982.

[37] W. Mönch. in: R. Vanselow, R. Howe (Eds), Chemistry and Physics of Solid Surfaces, V, vol. 35 of the Springer Series in Chemical Physics, Springer, Berlin, 1984.

[38] H. Lüth and G. Heiland. Surface photovoltage spectroscopy on semiconductor surfaces. *Il Nuovo Cimento*, 39 B(2):748–758, 1977.

[39] W. Mönch. *Semiconductor Surfaces and Interfaces.* Springer-Verlag: Berlin, 1993.

[40] W. Thomson (Lord Kelvin). Contact electricity of metals. *Phil. Mag.*, 46(278):82–120, 1898.

[41] J. Lagowsky, P. Edelman, M. Dexter, and W. Henley. Non-contact mapping of heavy metal contamination for silicon IC fabrication. *Semicond. Sci. Technol.*, 7:A185–A192, 1992.

[42] K. Shimakawa, J. Singh, and S. K. O'Leary. *Optical Properties of Disordered Condensed Matter.* Optical Properties of Condensed Matter and Applications, edited by J. Singh, John Wiley and Sons (2006).

[43] M. Grundmann. *The Physics of Semiconductors. An Introduction Including Nanophysics and Applications.* Springer, 2nd edition, 2010.

[44] Y. González, A. Abelenda, and M. Sánchez. Surface photovoltage spectroscopy characterization of AlGaAs/GaAs laser structures. *IOP Conf. Series: Journal of Physics: Conf. Series*, 792, 2017. doi:10.1088/1742-6596/792/1/012021.

[45] J.-H. Park and T. S. Sudarshan. *Surface Engineering Series Volume 2: Chemical Vapor Deposition.* ASM International, 2001.

[46] H. O. Pierson. *Handbook of Chemical Vapor Deposition: Principles, Technology and Applications.* Noyes Publication, 2nd edition, 1999.

[47] `https://www.oxford-instruments.com/products/etching-deposition-and-growth/plasma-etch-deposition/pecvd`.

[48] Martina Perani. Nanocrystalline Silicon Based Films For Renewable Energy Applications. PhD thesis, Universitá di Bologna - Scuola di Scienze, Dottorato di Ricerca in Fisica, 2013/2014.

[49] Z. A. Weinberg, G. W. Rubloff, and E. Bassous. Transmission, photoconductivity, and the experimental band gap of thermally grown SiO_2 films. *Phys. Rev. B*, 19(16):3107–3117, 1979.

[50] Margherita Sola. *Optoelectronic properties of $LaVO_3$ perovskite for photovoltaic applications investigated by surface potential measurements.* Master's degree thesis, Universitá di Bologna - Scuola di Scienze, Corso di Laurea Magistrale in Fisica, 2015/2016.

[51] `http://www.forter.com.tw/products_detail.asp?seq=550`.

[52] `http://www.controlledenvironments.org/Light1994Conf/5_9_Kofferlein/Kofferleintext.htm`.

[53] `http://www.scitec.uk.com/optical_chopper/pdf/model%20300%20optical%20chopper%20issue%201.0.pdf`.

[54] `http://www.horiba.com/fileadmin/uploads/Scientific/Documents/OSD/MSeries.pdf`.

[55] http://chem.libretexts.org/Textbook_Maps/Analytical_Chemistry_Textbook_Maps/Map%3A_Analytical_Chemistry_2.0_(Harvey)/10_Spectroscopic_Methods/10.1%3A_Overview_of_Spectroscopy.

[56] C. Palmer and E. Loewen. *Diffraction Grating Handbook.* Newport Corporation, 2005.

[57] http://www.horiba.com/us/en/scientific/products/optics-tutorial/monochromators-spectrographs.

[58] John H. Moore, Christopher C. Davis, Michael A. Coplan, and Sandra C. Greer. *Building Scientific Apparatus. A practical Guide to Design and Construction.* Cambridge University Press, 4th edition, 2009.

[59] http://www.thinksrs.com/downloads/PDFs/Manuals/SR830m.pdf.

[60] http://www.thinksrs.com/products/SR810830.htm.

[61] Michael B. Heaney. *The Measurement, Insturmentation and Sensors Handbook.* CRC Press, 1999. chapter Electrical Conductivity and Resistivity.

[62] F. M. Smits. Measurement of Sheet Resistivities with the Four-Point Probe. *Bell Sys. Tech. J.*, 37:711–718, May 1958.

[63] Keithley Instruments, Inc. *Series 2600B System SourceMeter Instrument: Reference Manual*, August 2016. 2600BS-901-01 Rev. C.

[64] Keithley Instruments, Inc. *2400 Series SourceMeter: User's Manual*, May 2002. 2400S-900-01 Rev. G.

[65] M. Vaněček, A. Poruba, A. Remeš, N. Beck, and M. Nesládek. Optical properties of microcrystalline materials. *Journal of Non-Crystalline Solids*, 227–230:967–972, (1998).

[66] S. M. Sze. *Physics of Semiconductor Devices.* Wiley-Interscience, John Wiley & Sons, Inc., 1969.

[67] Peter Y. Yu and Manuel Cardona. *Fundamentals of Semiconductors. Physics and Materials Properties.* Springer, 4th edition, 2010.

[68] C. Schinke *et al.* Uncertainty analysis for the coefficient of band-to-band absorption of crystalline silicon. *AIP Advances*, 5, 067168, (2015). doi: 10.1063/1.4923379.

[69] R. Koole, E. Groeneveld, D. Vanmaekelbergh, A. Meijerink, and C. de Mello Donegá. *Size Effects on Semiconductor Nanoparticles.* Nanoparticles. Workhorses of Nanoscience, edited by C. de Mello Donegá, Springer-Verlag Berlin Heidelberg (2014).

[70] D. W. Palmer, 2014. www.semiconductors.co.uk.

[71] I. Sychugov, F. Pevere, J.-W. Luo, A. Zunger, and J. Linnros. Single-dot absorption spectroscopy and theory of silicon nanocrystals. *Physical Review B*, 93:161413(R), (2016).